THE HETEROGENEOUS UPPER MANTLE: INSIGHTS FROM SEISMOLOGY

by
Oliver S. Boyd

B.A. Geology, University of Colorado at Boulder, 1995
M.S. Geology, University of Colorado at Boulder, 1997

A dissertation submitted to the
Faculty of the Graduate School of the
University of Colorado in partial fulfillment
of the requirement for the degree of
Doctor of Philosophy of
Geophysics Graduate Program
Department of Geological Sciences
2004

The dissertation entitled:
The Heterogeneous Upper Mantle: Insights from Seismology
written by Oliver S. Boyd
has been approved for the Department of Geological Sciences

_____
Anne Sheehan

_____
Craig Jones

_____
Date

A final copy of this thesis has been examined by the signatories, and we find that both the content and the form meet acceptable presentation standards of scholarly work in the above mentioned discipline.

Boyd, Oliver S. (PhD Geophysics)
The Heterogeneous Upper Mantle: Insights from Seismology
Dissertation directed by Professor Anne Sheehan

Insights into the composition and thermal structure of the upper mantle beneath multiple regions are made possible by various seismological techniques and additional constraints provided by gravity and mineral physics. I investigate the upper mantle beneath the Colorado Rockies, Sierra Nevada and New Zealand. In each region I find complicated compositional and thermal structure. The southwest Colorado Rockies are marked by a region of reduced shear wave speeds which many have believed are due to increased temperatures. I add the complementary measurement of shear wave attenuation and conclude, with the help of gravity, that southwest Colorado is underlain, not by increased temperatures, but by anomalous composition, specifically a small fraction of phlogopite. When investigating the Sierra Nevada, I again find multiple regimes of temperature and composition. Without the complementary measurement of attenuation, low velocities would have been misinterpreted as upwelling asthenosphere. I found however, that these low velocities actually reflect an unusual eclogite, a rock that is typically seismically fast. In New Zealand, through the use of receiver functions, I image the subducting Pacific Plate and its influence on the transition zone discontinuities. This influence depends strongly on temperature, composition, and the kinetics of mineral phase reactions. Whereas the deflection of the 660 km discontinuity appears consistent solely with the expected changes in temperature due to the subducting slab, the topography on the 410 km discontinuity is more complicated and requires multiple operating mechanisms to explain its behavior.

Acknowledgements

Without the guidance and support of Anne Sheehan, this dissertation would not have been possible. I am very appreciative of the fact that her door was always open and I always felt welcomed. The same applies for nearly all of the professors that helped answer most of my questions. The social support of my office mates is also appreciated. My friends and family kept me together and on track as well and special thanks go to my wife, Vicki Rystrom, mom, Kathy Grant, and dad, Jeff Boyd.

CONTENTS

LIST OF TABLES

2. ATTENUATION TOMOGRAPHY BENEATH THE ROCKY MOUNTAIN FRONT: IMPLICATIONS FOR THE PHYSICAL STATE OF THE UPPER MANTLE

3. FOUNDERING LITHOSPHERE IMAGED BENEATH THE SOUTHERN SIERRA NEVADA, CALIFORNIA, USA

APPENDIX 3. SUPPORTING ONLINE MATERIAL FOR: FOUNDERING LITHOSPHERE IMAGED BENEATH THE SOUTHERN SIERRA NEVADA, CALIFORNIA, USA

LIST OF FIGURES

2. ATTENUATION TOMOGRAPHY BENEATH THE ROCKY MOUNTAIN FRONT: IMPLICATIONS FOR THE PHYSICAL STATE OF THE UPPER MANTLE

3. FOUNDERING LITHOSPHERE IMAGED BENEATH THE SOUTHERN SIERRA NEVADA, CALIFORNIA, USA

4. ILLUMINATING UPPER MANTLE STRUCTURE BENEATH COOK STRAIT, NEW ZEALAND, WITH RECEIVER FUNCTIONS

APPENDIX 1. SOURCES OF ERROR

APPENDIX 2. MODEL RESOLUTION

APPENDIX 3. SUPPORTING ONLINE MATERIAL FOR: FOUNDERING LITHOSPHERE IMAGED BENEATH THE SOUTHERN SIERRA NEVADA, CALIFORNIA, USA

APPENDIX 4. *t** UNCERTAINTY FROM THE INTERFERENCE OF AN ADDITIONAL WAVELET

1. INTRODUCTION: THE IMPORTANCE OF REGIONAL SEISMIC INVESTIGATION AND ANELASTIC TOMOGRAPHY

1.1 WHY ARE WE INTERESTED IN THE EARTH'S INTERIOR?

Having knowledge and understanding of the interior of the Earth allows human populations to live more efficiently and adapt more quickly to the imminent changes in the natural systems of the planet and solar system. Some interior processes control long term trends in our environment. These include but are not limited to changes in heat flow that lead to changes in ice budgets and albedo, evolving plate positions that lead to changes in oceanic and continental topography and thereby affect oceanic and atmospheric circulation, and changes in volcanic output and subduction rates that lead to changes in atmospheric chemistry. Other interior processes of human interest produce catastrophic changes such as earthquakes, tsunamis and volcanic eruptions. In addition to natural processes that affect the human population's ability to live on the planet are the actions of other humans. Certain actions, such as the testing of high yield explosive weapons, can be monitored remotely using seismic instrumentation given knowledge of the material properties along the path through which the seismic wave has passed. Beyond the practical points rests a simple curiosity about the Earth. How was it formed? What is its composition? What are the processes controlling its evolution? Countless additional questions can be asked. Suffice it to say that there is strong interest in obtaining knowledge and understanding of the Earth's interior.

1.2 HOW DO WE LEARN ABOUT THE EARTH'S INTERIOR?

The stimulus for knowledge and understanding of the Earth's interior has lead to many strategies for obtaining the information necessary to answer these questions. These strategies are separated into direct and indirect methods. Direct methods involve collecting samples of the Earth's interior that are present at or near the Earth's surface [*Fei et al.*, 1999]. Several sorts of samples are available. Xenoliths are fragments of rock that once resided within the Earth and have become entrained in volcanic eruptions and brought to the surface. Samples of the Earth's interior can also be obtained from deep oceanic or continental crust that has been brought to the surface by tectonic forces. These samples can then be analyzed to gain knowledge and understanding of the Earth's interior. For example, what is its composition? What is its melting point? What is its viscosity as a function of temperature and pressure? When and under what temperatures and pressures did the minerals form?

Indirect methods become necessary because natural samples are available only from limited lateral extents of the crust and uppermost mantle. Indirect methods make use of remote and direct observations and theoretical assumptions to infer some property about the object being studied. Remote observations include gravity, magnetism, conductivity and seismic attributes. These indirect observations are integrated measures of relevant material properties and require assumptions about how the observations relate to the material properties. This leads to other questions that can be answered using direct methods. What is the sample's density? What is its seismic velocity and attenuation? What is its conductivity and magnetic susceptibility? How do these material properties change with temperature and

pressure? Minerals expected to exist in the lower mantle and core are synthesized so the previous questions can be addressed to these samples. This knowledge can be applied to indirect observations to infer the composition and temperature within the Earth.

Though direct and indirect methods will be referred to in subsequent chapters of this dissertation, I will now concentrate on a discussion of the indirect method of seismology. As opposed to other indirect methods, seismology not only has the advantage of generally being capable of higher resolution but it can be used to distinguish compositional as well as thermal variability. I begin by presenting various seismic observations and the interpretations that have been garnered from them. I then become more focused and turn the discussion to the anelastic behavior of materials during the passage of seismic waves. This topic is exceptionally important when trying to interpret seismic variability within the earth.

1.3 WHAT SEISMIC OBSERVATIONS HAVE BEEN MADE? WHAT HAS BEEN LEARNED?

In the 1970's there was a concerted effort by the International Association of Seismology and Physics of the Earth's Interior (IASPEI) to unify seismic observations by producing a consistent reference earth model that could explain them. Adam Dziewonski and Don Anderson were charged with this task. They compiled a dataset of normal mode periods with quality factors (Q values) and P and S-wave travel times and inverted for the radial distribution of anelastic parameters, densities and velocities within the Earth [*Dziewonski and Anderson*, 1981]. The attenuative properties of the

Earth were required to reconcile the relative dispersion between waves traveling with different periods. The additional complexity of transverse anisotropy in the upper 220 km was invoked to generate better fits between observed and predicted travel times. The results of this work have since been sited nearly 2000 times, a testament to its relevance.

More regional one-dimensional models of mantle velocities produced by Walck [1984; 1985] and Grand and Helmberger [1984] were utilized by Duffy and Anderson [1989] to compare with elasticity data of mantle minerals to estimate the likely composition of the mantle. These authors were interested in determining whether the mantle is primarily pyrolite [*Ringwood*, 1975], olivine and orthopyroxene accounting for 75% of the mineral assemblage, or piclogite [*Bass and Anderson*, 1984] where olivine is less than 50% of the mineral assemblage. Duffy and Anderson's preferred mantle composition is 40% olivine, 37% clinopyroxene, 13% garnet and 10% orthopyroxene, a piclogite composition. A direct method dataset compiled by Griffen et al. [1999] revealed that sub-continental lithospheric mantle (SCLM) does not have the same composition as what was found by Duffy and Anderson [1989]. The composition of SCLM is found to have evolved over time from the Archean (69% olivine, 2% clinopyroxene, 4% garnet and 25% orthopyroxene) to the Proterozoic (70% olivine, 6% clinopyroxene, 7% garnet and 17% orthopyroxene) to the present (66% olivine, 9% clinopyroxene, 8% garnet and 17% orthopyroxene). These compositions are approaching the composition predicted by Duffy and Anderson, decreasing olivine and orthopyroxene and increasing garnet and clinopyroxene.

Duffy and Anderson's compositional model is strongly controlled by the phase transitions of anhydrous olivine. Recent experimental evidence shows that a reasonable amount of hydration in the transition zone could substantially reduce seismic velocities, an effect that would allow for much greater amounts of olivine in the upper mantle [*Jacobsen et al.*, 2003; *Smyth et al.*, 2003]. In Chapter 4 of this dissertation, *"Illuminating upper mantle structure beneath Cook Strait, New Zealand, with receiver functions"*, I address this issue by investigating the topography on the 410 and 660 km seismic discontinuities in the vicinity of the subducting Pacific Plate. In addition to hydration, it is also very probable that chemical gradients exist at the boundaries between lithosphere, asthenosphere, mantle transition zone and lower mantle.

Knowing the composition of the mantle is critical to evaluating the primary questions posed in section 1.1. Poorly known mantle composition could severely bias estimates of mantle density, temperature and viscosity. These poorly known parameters would then result in possible misinterpretations of the expected style of mantle convection, errors in the estimates of heat flow at the base of the crust, etc.

1.4 WHY IS THE ADDITIONAL MEASUREMENT OF ATTENUATION IMPORTANT?

A necessary piece of information to complement seismic velocities is seismic attenuation, the loss of seismic energy. Attenuation is defined as the inverse of the quality factor, Q,

$$Q^{-1} = \frac{\Delta E}{4\pi \bar{E}}, \tag{1}$$

where ΔE is the energy lost during a cycle of strain and $\bar{E}$ is the average strain energy during one cycle. The relationship between attenuation and velocity is dependent on composition and temperature such that this relationship can simultaneously identify regions of both compositional and thermal variability. Many regional and global studies have relied on measured seismic velocities and relied upon either a constant attenuation or an assumed relationship of wavespeed to attenuation to estimate compositional and thermal variability. A poor knowledge of attenuation can result in serious error in interpreting measured velocities. As an example, Karato [1993] points out that the temperature derivative of velocity decreases by 50% when Q decreases from 100 to 50. Chapter 2 of this thesis, "*Attenuation tomography beneath the Rocky Mountain Front: Implications for the physical state of the mantle*", addresses this issue by directly measuring attenuation to properly differentiate and quantify the thermal and compositional variability beneath the southern Rocky Mountains. This knowledge is then used to better understand upper mantle dynamics in the region. Additional work, presented in Chapter 3 of this thesis, *"Foundering lithosphere imaged beneath the southern Sierra Nevada, California, USA"*, further addresses these issues but with the added complication of anisotropy.

1.5 WHAT CONTROLS THE ANELASTIC BEHAVIOR OF ROCKS? WHAT ARE SOME CHARACTERISTIC VALUES OF ATTENUATION, THE INVERSE OF THE QUALITY FACTOR?

Seismic attenuation in rocks can be caused by any mechanism that removes strain energy from the seismic wave. Mechanisms of seismic attenuation such as melt squirt or local fluid flow [*O'Connell and Budiansky*, 1977; *Mavko*, 1980], global fluid flow [*Biot*, 1956], three-phase flow [*Schutt et al.*, 2000; *Brunner and Spetzler*, 2001], grain-boundary sliding [*Ghahremani*, 1980], and bowing dislocations [*Minster and Anderson*, 1981], depend on the seismic frequency, pressure, temperature, composition of the melt phase(s), and in some cases, composition of the solid phase. For frequencies around 1 Hz, the crust is typically most sensitive to various types of fluid flow, primarily because of the low temperatures and high porosity. Deeper in the Earth, as temperatures and pressures increase, bowing dislocations within mineral grains become a more likely mechanism for seismic attenuation.

At seismic frequencies, average values for the quality factor range from 50 to 100 in the upper crust to several hundred in the lower crust [*Patton and Taylor*, 1984; *Chen et al.*, 1994]. Dziewonski and Anderson [1981], during their work on PREM, found that to reconcile seismic velocities at different periods, they had to require that shear Q be 600 in the crust, 80 in the mid upper mantle and increase to just over 300 near the base of the mantle. Shear Q drops again to about 85 in the inner core. They estimated that the compressional quality factor outside of the inner core is 57822 and decreases to 1328 in the inner core. Durek and Ekstrom [1996] found similar values of radially averaged Q though compressional Q decreases to 950 in the asthenosphere. These are one-dimensional estimates and do not address lateral

variability nor frequency dependence. Low resolution global models begin to address the problem of spatial variability [*Romanowicz*, 1995; *Bhattacharyya et al.*, 1996; *Reid et al.*, 2001]. Unfortunately for relatively high resolution velocity tomography [*Lee and Grand*, 1996], temperature derivatives of velocity using attenuation estimates from global models could be severely inaccurate if the attenuation model does not correspond in spatial resolution to the velocity model or is not constant across the periods for which velocity and attenuation were measured [*Roth et al.*, 2000].

Many studies have shown that attenuation is at least weakly dependent on frequency, w,

$$Q^{-1} \propto w^{-\alpha} \tag{2}$$

where α is approximately 0.2 [*Karato and Spetzler*, 1990; *Sobolev et al.*, 1996; *Warren and Shearer*, 2000]. Laboratory experiments suggest that this relationship holds for a broad frequency range [*Jackson*, 1993]. There is recent evidence however, that within the earth (2) may hold only for a limited frequency range [*Wahr and Benjamin*, personal communication] thereby producing a limited frequency band over which anelastic mechanisms are active. The Chapter 2 of this dissertation addresses this issue.

The possibility of an absorption band or at least frequency dependence minimally complicates the simple conversion of velocity variations to thermal variations using the relation given by Karato [1993] (equation 2.2 in this dissertation).

For reasons stated above, a single value of Q can not be used for an entire region. Moreover, because of compositional variations, band limited absorption, and the possibility of multiple mechanisms of seismic absorption, simple relationships between velocity and attenuation can not be used either. We are left then to measure attenuation independently and apply the appropriate equations for frequency dependent attenuation.

2. ATTENUATION TOMOGRAPHY BENEATH THE ROCKY MOUNTAIN FRONT: IMPLICATIONS FOR THE PHYSICAL STATE OF THE UPPER MANTLE

2.1 ABSTRACT

Utilizing the Rocky Mountain Front (RMF) broadband seismic dataset acquired in 1992, this study has derived the seismic attenuation structure underlying part of the Southern Rocky Mountains and surrounding areas through measurements of differential t^* of S-phase waveforms. Previous studies of the area include P, S and surface wave travel time tomography, and all indicate low upper mantle velocities below the Rocky Mountain region. Calculations of intrinsic attenuation coupled with current velocity models aid in the determination of temperature, partial melt distributions, and compositional variation. A N-S zone of high shear wave attenuation ($Q_s \approx 30$) is found in the mantle beneath the Rocky Mountains and lies east of the region of lowest shear wave velocity. Relationships between shear wave attenuation and shear wave velocity are consistent with both thermal and compositional variability. Along the eastern Colorado Rockies and due north of the Rio Grande Rift, the relationships are consistent with an interpretation of elevated temperatures by up to 50 K at 125 km depth. West of this region low velocities and low attenuation suggest either unusual composition or very high temperatures. The low density mantle material beneath the Colorado Rocky Mountains in addition to increased crustal thickness and low density crustal intrusions provides a density contrast sufficient to support its overburden.

2.2 INTRODUCTION

For decades, geologists have questioned the mechanisms responsible for the high topography of the Rocky Mountains. Are the mountains supported by crustal thickening due to shortening (Airy root) or are there lateral density contrasts in the crust (Pratt compensation)? Is the lithosphere sufficiently rigid to support the topography? Does support come from the mantle rather than the crust? Measurements of crustal thickness by Sheehan et al. [1995] and Li et al. [2002] indicate an increase in crustal thickness that is not entirely able to support the overlying Rocky Mountains. Models of flexural support indicate that little of the observed topography is supported by bending of the elastic plate [*Sheehan et al.*, 1995]. These observations imply that regions of the crust and/or mantle have a reduced relative density.

Previous measurements that have explored the role of reduced crust/mantle density centered on measuring the change in seismic velocity across the region. Lee and Grand [1996], using the Rocky Mountain Front seismic dataset, measured shear wave travel times from teleseismic S-phase arrivals beneath the Colorado Rocky Mountains. The resulting shear wave velocity structures indicate reduced upper mantle velocity directly beneath the Colorado Rocky Mountains (Figure 1). The reduced upper mantle velocities trend north-south beneath the Colorado Rocky Mountains where the minimum shear wave velocity, -9% relative to western Kansas, occurs along this trend northwest of the Rio Grande Rift. Hessler [1997] produced a similar map from P wave travel time tomography but with smaller variations in P wave velocity, -4% (also summarized by Lerner-Lam et al. [1998]). Li et al. [2002] measured surface wave dispersion and inverted for crustal and upper mantle shear

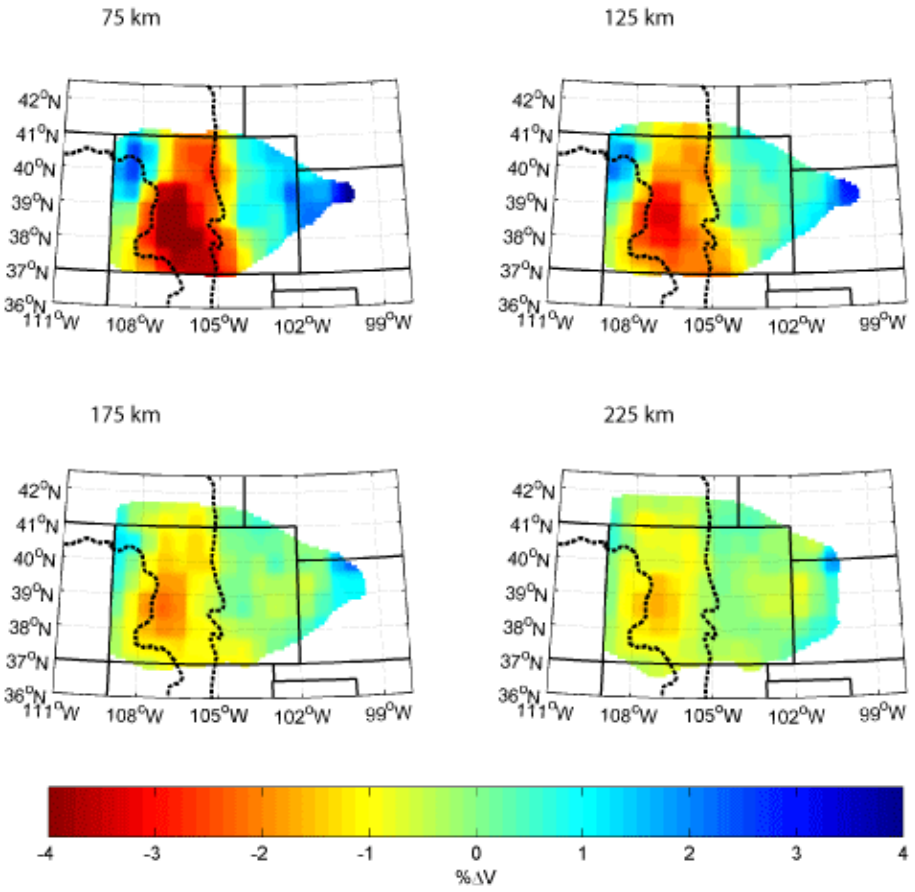

Figure 1. Horizontal slices of shear velocity variation [Lee and Grand, 1996] at four depths.Solid black lines denote state boundaries. Thick dashed solid lines delineate the Rocky Mountain region. Negative values (red) indicate slower velocities. Shear velocities beneath the Colorado Rocky Mountains are reduced by up to 9% relative to western Kansas. The transition to higher velocities in the east is believed to signify the transition to the stable craton.

wave velocity. The greatest difference between the models of Lee and Grand and Li et al. is from 50 to 100 km depth beneath southwest Colorado where Lee and Grand's greatest decrease in shear velocity, -9%, corresponds to a decrease of only -6% from the model of Li et al. In addition, this position correlates with Li et al.'s thickest crust. Li et al. also find slow crustal shear velocities beneath the Sawatch Range in central Colorado which is correlated with high heat flow [*Decker et al.*, 1988]. Decker et al.

used heat flow measurements and Bouguer gravity anomalies to infer the presence of granitic intrusions that were emplaced in the Miocene through the Quaternary. Li et al. point out that this compositional variation could explain the reduced shear velocities.

Changes to seismic velocity can result from changes to several material properties including temperature, composition and partial melt. If Lee and Grand's measured 9% lateral decrease in shear velocity in the upper mantle were due solely to increased temperature, using the scaling relations of Nataf and Ricard [1996] for changes in velocity with respect to temperature,

$$\frac{\partial \ln V_S}{\partial T} = -1.1 \times 10^{-4} K^{-1}, \qquad (1)$$

changes in temperature would be over 800 K. Lateral changes of this magnitude are unlikely. Such changes would produce density contrasts far exceeding those required to support the Rocky Mountains as well as produce wide spread melting.

Karato [1993] shows that velocity-temperature scaling relationships are dependent on attenuation (Q^{-1}), a fact that Nataf and Ricard briefly considered but did not fully exploit. Using Karato's relations with a Q of 50, a 9% S-wave velocity contrast will predict a change in temperature of almost 400 K. If only half of the measured velocity contrast is attributable to changes in temperature, a Q of 50 coupled with ΔV_S of 4.5% implies a change in temperature of only 200 K.

Attenuation models coupled with velocity models can also lead to models of the unrelaxed velocity [*Minster and Anderson*, 1981] which is sensitive to composition including the effects of partial melt [*Duffy and Anderson*, 1989; *Hammond and*

Humphreys, 2000b]. If half of the measured velocity contrast were due to partial melt, Hammond and Humphreys [2000b] predicts that a 5% decrease in shear velocity would accompany a 0.6% increase in partial melt.

Previous studies of the attenuation structure beneath western North America indicate broad regional variations. Lay and Wallace [1988] examined multiple ScS wave attenuation west of the Rocky Mountains and found the highest attenuation values, $Q_{ScS} = 95 \pm 4$, beneath the Basin and Range. The lowest attenuation values, $Q_{ScS} = 344 \pm 88$, were measured beneath the Pacific Northwest. Al-Khatib and Mitchell [1991] measured Rayleigh wave attenuation coefficients across several regions of western North America. One measurement traversed the eastern Colorado Rocky Mountains on its way from southern New Mexico to Edmonton, Alberta. Average Q_β along this path reaches a minimum of 35 at 150 km depth. A higher resolution study [*Slack et al.*, 1996] measured P and S wave travel time delays and path integrated attenuation, differential t^*, across the Rio Grande Rift. Differential t^* spans a range of 3 seconds for S-waves and 2 seconds for P-waves, but there is significant scatter in their data with respect to the relationship between delay time and differential t^*. Possibly because of this scatter, they do not attempt to solve for Q. Global models [*Romanowicz*, 1995; *Bhattacharyya et al.*, 1996; *Reid et al.*, 2001] are consistent with the above studies and also lack the resolution to quantify changes in temperature, partial melt and composition in the upper mantle beneath the Rocky Mountains.

In this paper, we measure the integrated differential attenuation of teleseismic S-phases, δt^* [*Sheehan and Solomon*, 1992], and correct for sedimentary basin

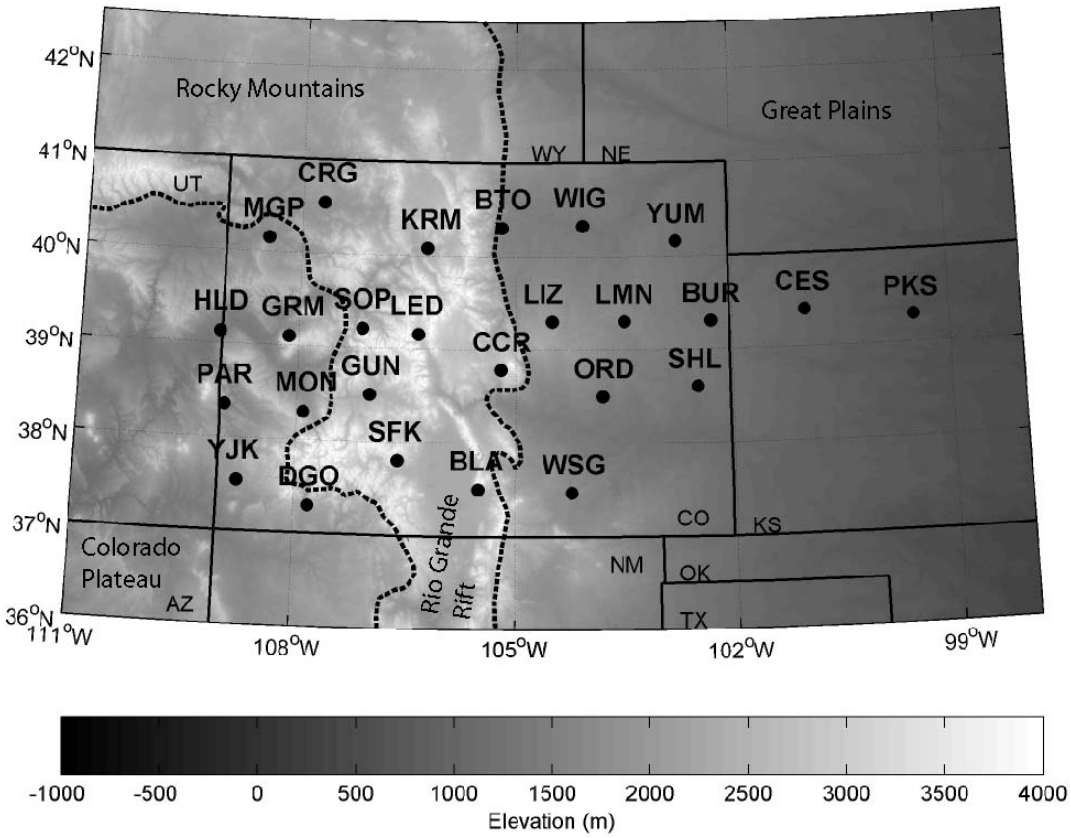

Figure 2. Seismic stations of the Rocky Mountain Front seismic experiment (RMF) used in this study on gray-scale topographic relief map. Stations are denoted by filled circles and a three letter station code. Geologic provinces are separated by thick dashed lines.

reverberations. This measurement along with an a priori velocity model and ray path modeling is used to derive the shear wave attenuation structure in the upper mantle. This information is coupled with the Lee and Grand shear wave velocity model [1996] to identify regions of compositional and thermal variability. Karato's shear velocity - temperature derivative relationship [1993] is applied to estimate the mantle thermal component of isostatic compensation while an analysis is performed using the residual topography to estimate the best relationship between density and unrelaxed shear velocity, $\partial \ln \rho / \partial \ln V_S$, and better constrain the likely compositions.

The mantle component of isostatic compensation is combined with estimates of compensation due to changes in crustal thickness using the model of Li et al. [2002] to evaluate overall isostatic compensation.

2.3 δt^* MEASUREMENT

The RMF seismic dataset was acquired by a two dimensional array of 37 broadband, multicomponent seismometers , 26 of which were used for this study (Figure 2, Table 1), deployed for a period of nearly seven months during 1992 [*Sheehan et al.*, 1995; *Lerner-Lam et al.*, 1998]. Twenty-seven stations were Guralp CMG3-ESP seismometers with a 30 second corner period, two were Guralp CMG3 seismometers with a 10 second corner period, and eight were Streckeisen STS-2 seismometers with a 120 second corner period. The instrument response of the seismometers is flat below the corner period. Events are initially extracted based on the following criteria:

$$65° < \Delta < 85° \;\&\; m_b > 5.6$$

$$45° < \Delta < 65° \;\&\; m_b > 5.4$$

$$30° < \Delta < 45° \;\&\; m_b > 5.3$$

where Δ is the epicentral distance in degrees and m_b is the body wave magnitude. All waveforms are visually inspected before picking windows for signal and noise (Figure 3a). Waveforms with no recognizable S phase are removed. The resulting dataset consists of 380 S-wave traces from 37 events (Figure 4, Table 2).

Table 1. Station Information

Station Name	Latitude	Longitude	Elevation (km)	Sediment Thickness (km)	Sediment Shear Vel. (km/s)	Basin Reflection Coefficient
BLA	37.54	-105.58	2.72	0.0		
BTO	40.38	-105.20	1.73	1.4	2.15	-0.29
BUR	39.38	-102.35	1.26	1.9	2.15	-0.29
CCR	38.77	-105.22	2.68	0.0		
CES	39.38	-101.05	0.94	0.0		
CRG	40.54	-107.70	2.07	5.1	1.98	-0.32
DGO	37.30	-107.81	2.43	2.4	2.28	-0.22
GRM	39.10	-108.13	2.37	2.4	1.98	-0.31
GUN	38.50	-107.00	2.66	0.0		
HLD	39.23	-109.08	1.50	0.0		
KRM	40.08	-106.24	2.53	1.8	2.15	-0.29
LED	39.15	-106.35	3.37	0.0		
LIZ	39.35	-104.54	1.99	4.1	2.15	-0.29
LMN	39.41	-103.62	1.63	2.9	2.15	-0.29
MGP	40.15	-108.46	1.93	2.2	1.98	-0.32
MON	38.41	-107.99	2.39	0.6	2.28	-0.22
ORD	38.50	-103.80	1.47	2.0	2.15	-0.29
PAR	38.33	-108.98	2.05	4.0	2.28	-0.22
PKS	39.25	-99.53	0.63	0.0		
SFK	37.80	-106.60	3.07	0.0		
SHL	38.60	-102.50	1.26	1.8	2.15	-0.29
SOP	39.21	-107.12	2.66	0.0		
WIG	40.32	-104.07	1.39	2.8	2.15	-0.29
WSG	37.47	-104.23	1.71	0.7	2.15	-0.29
YJK	37.54	-108.77	2.08	2.7	2.28	-0.22
YUM	40.16	-102.78	1.27	2.1	2.15	-0.29

Table 1. Station information. Station designation, latitude, longitude, elevation, sediment thickness [*Sheehan et al.*, 1995; *Burchfiel*, 1992], velocity, and reflection coefficient. Please see Appendix 1.1 for information about velocity and reflection coefficient.

Each waveform undergoes conditioning before the calculation of δt^*. The channels are rotated to obtain the transverse component so as to isolate SH motion and minimize S to P conversions. The waveforms are band pass filtered to between 0.005 and 0.4 Hz and cropped to a 200 second window surrounding the hand picked S arrival. The waveform's trend and mean are removed, after which a 10% cosine taper

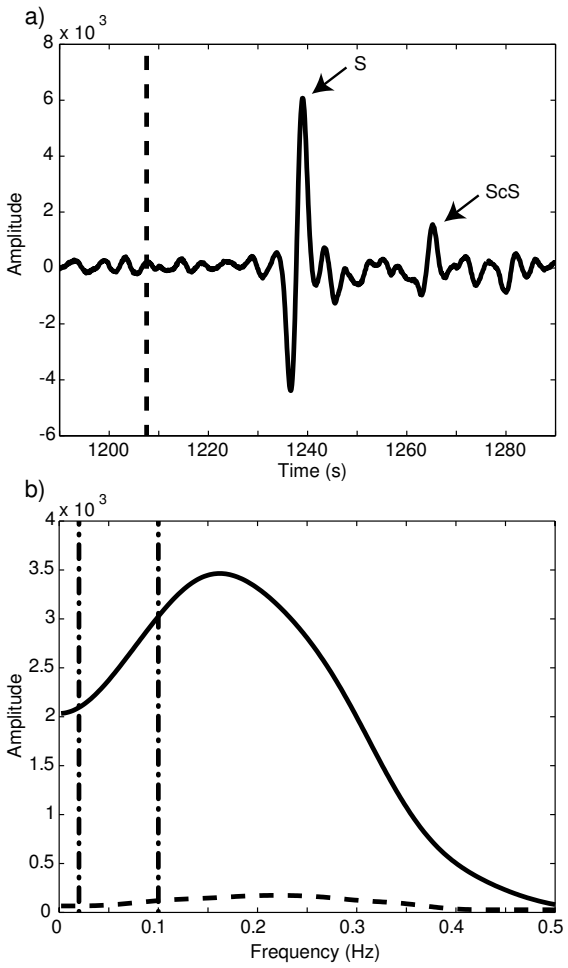

Figure 3. Example time series (a) and associated spectra for signal and noise (b). (a) Seismic phases S and ScS are denoted for reference. The dashed vertical line is the location of the center of the 30 second time window for the noise. This time series was recorded at station DGO and is from a magnitude 5.7 earthquake in northern Japan (backazimuth of 318 degrees, distance of 76 degrees, and depth of 317 km). (b) Signal spectra (solid line) and pre-event noise spectra (dashed line). Signal to noise ratio is 28.5. The vertical dashed dot lines span the frequency range over which the δt^* measurement is made.

is applied. The station's instrument response is removed and then the waveform is reconvolved with a common instrument response, that of the CMG-3 ESP broadband seismometer. The waveform is further reduced to a 30 second window centered on the S-pulse and multiplied by a gaussian taper. Larger windows and less severe tapers result in lower signal to noise ratios which degrades the measurement of δt^*. A multi-

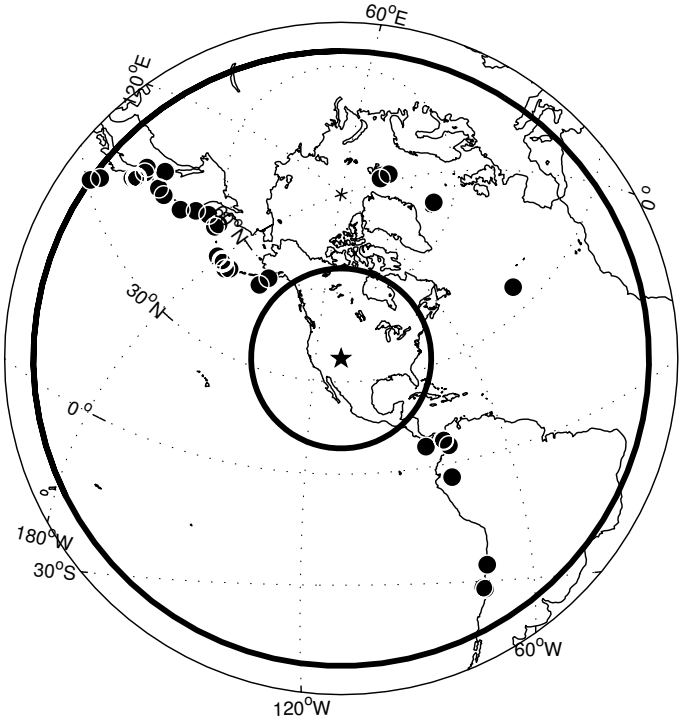

Figure 4. Locations of earthquakes used in this study (filled circles). Most of the events originate from either the northwest or southeast. Thick solid black circles are 30 and 80 degrees distant from the center of the RMF seismic array.

taper spectral analysis [*Percival and Walden*, 1993] with a time-bandwidth product of 3 is performed on the prepared time series to obtain the station spectra (Figure 3b).

For our measurements, t^* for a given signal is measured relative to a reference spectrum. The reference spectrum is derived from a pseudo-source which is the alignment and stack of all signals for a given event. The spectra for the station trace and the reference trace (Figure 5a) are given by:

$$A_S(f) = G_S S(f) I_S(f) R_S(f) e^{-\pi f t_S^*} \tag{2}$$

$$A_R(f) = G_R S(f) I_R(f) R_R(f) e^{-\pi f t_R^*} \tag{3}$$

Table 2. Event Information

Event #	Origin time	Latitude	Longitude	Depth (km)	Magnitude	σ(δt*) / NS
21	5/30/1992 (151) 12:42:03.500	30.69	141.59	20	5.9	3.7
39	6/03/1992 (155) 6:10:54.300	51.13	178.74	22	5.9	3.2
64	6/16/1992 (168) 5:51:03.700	45.70	142.26	317	5.7	3.6
68	6/21/1992 (173) 10:52:42.400	-26.50	289.34	39	5.7	4.8
77	6/24/1992 (176) 12:11:26.000	51.50	186.55	33	5.7	3.8
82	6/26/1992 (178) 11:32:27.100	6.13	277.65	10	5.8	5.1
138	7/10/1992 (192) 9:31:27.500	44.70	149.48	20	6.2	2.8
142	7/12/1992 (194) 11:08:55.300	41.46	142.03	64	6.0	3.2
146	7/13/1992 (195) 15:34:04.500	51.17	157.63	45	5.7	5.3
147	7/13/1992 (195) 18:11:33.700	-3.92	283.40	97	6.1	3.4
161	7/18/1992 (200) 8:36:58.700	39.42	143.33	29	6.2	2.8
165	7/18/1992 (200) 10:20:11.900	39.44	143.03	27	6.1	2.9
171	7/18/1992 (200) 13:56:54.400	39.48	142.96	27	5.8	3.3
180	7/20/1992 (202) 7:46:46.700	78.56	5.52	10	5.7	3.0
189	7/25/1992 (207) 2:53:28.300	38.73	143.01	17	5.9	2.6
202	7/29/1992 (211) 4:30:47.700	39.50	143.50	16	5.9	3.6
229	8/11/1992 (224) 15:14:55.100	32.54	141.64	16	5.8	3.7
233	8/15/1992 (228) 19:02:09.100	5.11	284.39	119	5.7	3.8
239	8/19/1992 (232) 0:57:40.200	50.50	185.08	10	6.2	3.4
251	8/24/1992 (237) 6:59:39.900	41.98	140.66	121	6.2	3.6
293	9/09/1992 (253) 13:08:54.800	76.21	7.29	24	5.7	4.2
306	9/14/1992 (258) 20:33:30.500	54.32	166.67	38	5.5	5.5
323	9/26/1992 (270) 5:45:50.600	64.78	342.41	10	5.5	3.5
326	9/27/1992 (271) 17:48:13.000	53.93	202.70	33	5.8	3.6
330	9/30/1992 (274) 3:27:59.100	51.41	181.37	26	5.9	4.1
331	9/30/1992 (274) 5:34:00.300	51.28	181.96	33	6.1	3.2
333	9/30/1992 (274) 9:42:50.900	51.15	181.83	14	5.8	3.1
335	10/01/1992 (275) 5:02:34.100	51.12	182.00	15	5.9	4.2
342	10/08/1992 (282) 16:34:53.200	51.15	182.13	21	5.6	4.0
355	10/17/1992 (291) 8:32:40.500	6.85	283.19	14	6.2	2.9
359	10/18/1992 (292) 15:11:59.100	7.08	283.14	10	6.6	3.2
371	10/20/1992 (294) 4:40:01.700	55.52	166.30	27	5.7	5.4
405	11/04/1992 (309) 21:32:33.900	-31.57	288.44	19	5.8	2.4
412	11/10/1992 (315) 9:58:10.800	51.49	182.39	33	5.8	5.7
436	11/28/1992 (333) 3:13:33.300	-31.33	288.01	12	5.8	3.3
437	11/30/1992 (335) 9:32:37.500	35.69	325.42	20	6.1	4.7
442	12/07/1992 (342) 2:11:42.300	43.95	147.15	45	5.8	4.4

Table 2. Event information from NEIC. Event #, origin time: date, Julian day and time, latitude, longitude, depth, magnitude (m_b), and the slope of the relationship between the standard deviation of δt^* and the synthetic noise to signal ratio, σ(δt*) / NS, determined for each event (Appendix 1.2).

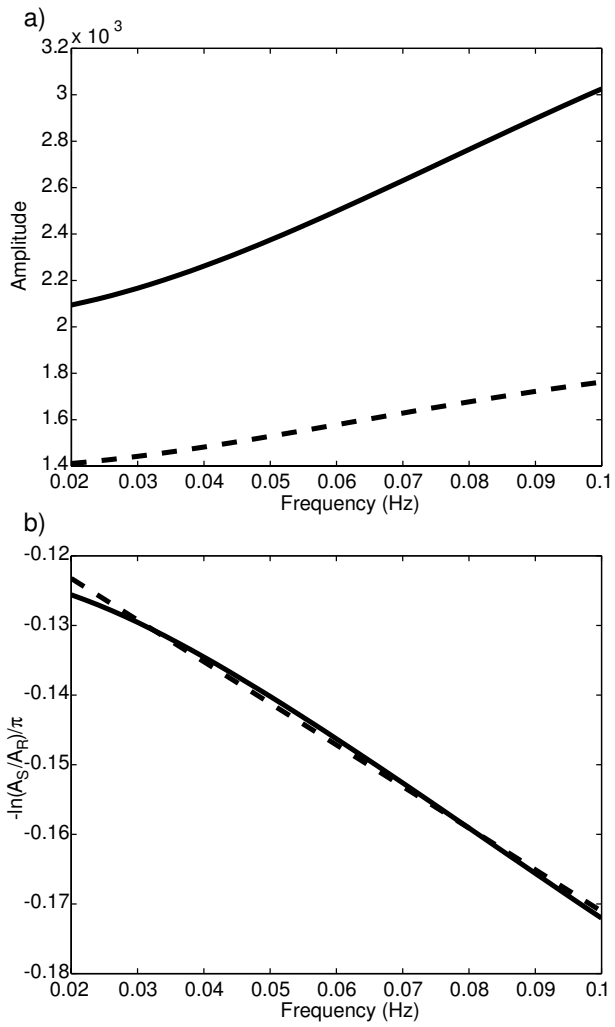

Figure 5. (a) Example spectra for the signal (solid line) and reference (dashed line) and (b) spectral ratio (solid line) with linear fit (dashed line). (a) The signal spectrum is that shown in Figure 3b limited to the frequency range 0.02 to 0.1 Hz. The reference spectrum is the average of spectra from all stations present for a given event. (b) The solid line is the natural log of the ratio of amplitudes between the station and the reference divided by -π. The dashed line is the linear fit to the solid line over the frequency range 0.02 to 0.1 Hz. For this example, δt^* is –0.59. The difference to the value given in Table 3 is due to the removal of the event mean.

where f is the frequency, G is the geometrical spreading, S is the source function, I is the instrument response, R is the crustal response, and $e^{-\pi f t^*}$ results from the energy loss along the ray's path from source to receiver. The subscripts S and R refer to the station and reference respectively. To find δt^*, we look at the ratio of spectral

amplitudes, $A_S(f)/A_R(f)$. Relative t^* is calculated for a given event to facilitate the cancellation of the source term in the spectral ratio. If the geometrical spreading is frequency independent, δt^* will not be a function of G. The instrument response cancels because we have removed the station instrument response, $I_S(f)$, and reconvolved the waveform with a common instrument response, $I_R(f)$. At this point, the crustal response terms are removed. Synthetic tests are performed to further examine thecontribution of crustal response terms (Appendix 1.1) and a correction to δt^* is made using estimated basin thicknesses, shear velocities and impedance contrasts. The remaining spectral ratio is

$$\frac{A_S(f)}{A_R(f)} = e^{-\pi f (t_S^* - t_R^*)}. \tag{4}$$

Solving for δt^*, we have

$$\delta t^* = t_S^* - t_R^* = \partial \left[\ln\left(\frac{A_S(f)}{A_R(f)} \right) \Big/ -\pi \right] \Big/ \partial f \quad . \tag{5}$$

The slope of the curve between $\ln(A_S(f)/A_R(f))/(-\pi)$ and f is δt^*. We make δt^* measurements by finding the slope of the straight line that is fit to the curve of $\ln(A_S(f)/A_R(f))/(-\pi)$ vs. f over the frequency range 0.02 to 0.1 Hz (Figure 5b). This frequency range is used in the measurements for two reasons. The spectral energy at these frequencies is high, the spectral decay at higher frequencies can be dominated by scattering attenuation, and the spectral energy at lower frequencies can be contaminated by decreased sensitivity of the sensors.

The total number of traces for which δt^* is calculated is 380 (Table 3). The number of traces originating from the northwest is 280, the northeast, 25, the southeast, 75, and southwest, 0. After removing apparent δt^* due to basin reflections (Appendix 1.1), the variance of δt^* is 0.63 seconds. Appendix 1.2 uses synthetics to determine that 75% of this variance could be due to normally distributed random noise. This may seem excessive but Appendix 2 shows that a properly weighted inversion can produce a reasonable model.

Figure 6 is an average δt^* map for events originating from the northwest (top) and southeast (bottom) for uncorrected (left) and basin corrected (right) δt^* values. All δt^* values for events originating from a given direction for a given station are weighted by the inverse of the standard deviation of δt^* error due to normally distributed random noise (Appendix 1.2) and averaged, and the resulting weighted average is placed at the station location. The basin corrections tend to be negative resulting in an increase in δt^* in the basins after the correction is applied. Observations of the spatial distribution of δt^* in dependence on backazimuth are inconclusive. It appears possible that high δt^* moves to the northwest when examining events from the southeast and to the southeast for events from the northwest. The lack of an obvious pattern may mean that the measurements have considerable error or that the distribution of attenuation in the upper mantle is sufficiently complex to make the examination of these δt^* maps inconclusive.

Table 3. δt^* Data and Information

Station Name	Event Num	Original δt^*	δt^* corrected	δt^* correction	SN
MGP	21	0.46	0.63	0.17	14.5
CRG	21	-1.24	-0.69	0.55	15.7
HLD	21	0.29	0.29	0.00	39.3
GRM	21	-0.91	-0.68	0.22	14.1
MGP	39	0.12	0.24	0.12	18.5
CRG	39	-0.88	-0.40	0.48	9.3
HLD	39	0.03	0.03	0.00	18.7
GRM	39	-0.14	0.03	0.17	13.4
PAR	39	-0.69	-0.41	0.29	13.7
KRM	39	0.05	0.07	0.03	22.9
SOP	39	-0.47	-0.54	0.00	30.2
MON	39	0.82	0.80	-0.02	14.3
YJK	39	-0.78	-0.66	0.12	26.7
BTO	39	0.04	0.02	-0.02	46.3
GUN	39	0.07	0.07	0.00	21.3
DGO	39	-1.61	-1.55	0.06	15.0
WIG	39	-0.07	0.15	0.22	10.7
YUM	39	0.10	0.16	0.06	19.4
LMN	39	-1.13	-0.88	0.25	13.0
CES	39	1.04	1.04	0.00	30.9
PKS	39	0.43	0.43	0.00	41.5
MGP	64	-0.21	-0.03	0.18	14.8
CRG	64	-1.24	-0.94	0.31	18.8
HLD	64	0.10	0.10	0.00	22.8
GRM	64	-0.30	-0.06	0.24	11.3
PAR	64	-0.35	-0.06	0.29	39.8
BTO	64	0.09	0.11	0.01	31.3
MON	64	0.35	0.34	-0.01	41.9
YJK	64	-0.46	-0.30	0.16	18.0
LED	64	-1.66	-1.66	0.00	4.5
GUN	64	0.35	0.35	0.00	22.4
DGO	64	-0.50	-0.40	0.10	28.5
CCR	64	0.31	0.31	0.00	41.4
YUM	64	0.00	0.11	0.11	16.5
LMN	64	0.03	0.33	0.30	11.9
BLA	64	0.44	0.44	0.00	2.1
ORD	64	-0.50	-0.41	0.09	0.8
BUR	64	0.21	0.28	0.07	4.2
CES	64	0.41	0.41	0.00	14.3
PKS	64	-0.14	-0.14	0.00	12.5

Table 3. δt* data and information. Station name, Event number from NEIC, the original t*, corrected t*, and t* correction, and the waveforms signal to noise ratio.

Table 3. δt^* Data and Information (continued)

Station Name	Event Num	Original δt^*	δt^* corrected	δt^* correction	SN
PKS	68	0.48	0.48	0.00	17.6
WSG	68	0.18	0.19	0.01	42.6
CES	68	-0.68	-0.68	0.00	6.9
BUR	68	-0.92	-0.76	0.16	3.7
LMN	68	-1.60	-1.13	0.47	9.0
LIZ	68	-0.82	-0.15	0.68	7.3
YUM	68	-1.17	-0.95	0.22	17.1
GUN	68	0.25	0.25	0.00	12.2
YJK	68	-0.50	-0.24	0.26	9.9
LED	68	1.47	1.47	0.00	1.6
MON	68	-0.36	-0.35	0.00	7.2
WIG	68	-0.86	-0.43	0.44	12.9
BTO	68	0.28	0.36	0.07	4.7
PAR	68	0.10	0.55	0.44	6.9
GRM	68	0.23	0.62	0.39	14.6
KRM	68	1.02	1.19	0.16	4.9
HLD	68	-0.10	-0.10	0.00	6.1
CRG	68	-0.94	-0.39	0.55	23.8
MGP	68	0.01	0.33	0.32	37.8
CRG	77	-1.07	-0.58	0.49	18.1
HLD	77	0.02	0.02	0.00	11.6
PAR	77	0.04	0.39	0.34	11.5
GRM	77	0.03	0.28	0.25	11.9
KRM	77	-0.10	-0.02	0.08	11.0
YJK	77	0.58	0.75	0.17	16.6
MON	77	0.63	0.61	-0.01	22.9
BTO	77	0.12	0.13	0.01	13.2
GUN	77	0.40	0.40	0.00	11.4
LED	77	-0.58	-0.58	0.00	3.1
WIG	77	-0.77	-0.47	0.30	10.7
LIZ	77	-0.92	-0.38	0.54	21.2
YUM	77	-0.36	-0.24	0.12	8.4
LMN	77	-1.52	-1.18	0.33	15.7
BUR	77	0.07	0.14	0.08	8.1
WSG	77	1.13	1.12	-0.02	8.6
CES	77	0.40	0.40	0.00	12.2
PKS	77	-0.35	-0.35	0.00	30.6
PKS	82	-1.20	-1.20	0.00	7.6
WSG	82	-0.03	-0.03	0.01	6.4
CES	82	-2.61	-2.61	0.00	5.3
BUR	82	-0.96	-0.85	0.11	5.3
DGO	82	2.24	2.36	0.13	4.0
WIG	82	-1.48	-1.19	0.29	3.6
LED	82	0.76	0.76	0.00	8.2

Table 3. δt^* Data and Information (continued)

Station Name	Event Num	Original δt^*	δt^* corrected	δt^* correction	SN
YJK	82	-0.03	0.14	0.17	24.8
BTO	82	-0.36	-0.31	0.05	3.0
KRM	82	-0.46	-0.35	0.11	3.9
GRM	82	1.65	1.91	0.26	4.2
HLD	82	0.98	0.98	0.00	7.9
CRG	82	-0.68	-0.42	0.26	6.4
MGP	82	0.29	0.51	0.22	5.8
CRG	138	-0.51	-0.32	0.19	10.1
GRM	138	-0.72	-0.70	0.02	12.6
PAR	138	0.01	0.04	0.03	9.5
KRM	138	0.17	0.17	0.00	1.7
SOP	138	-0.43	-0.41	0.00	15.1
MON	138	-0.09	-0.10	-0.01	20.3
BTO	138	-0.28	-0.29	-0.01	23.3
LED	138	0.51	0.51	0.00	17.5
WIG	138	0.63	0.65	0.02	11.6
SFK	138	-0.06	-0.06	0.00	16.9
CCR	138	0.75	0.75	0.00	18.3
YUM	138	0.30	0.30	0.00	12.5
LMN	138	-0.39	-0.37	0.02	7.4
BLA	138	-0.34	-0.34	0.00	3.4
PKS	138	0.15	0.15	0.00	17.0
MGP	142	-0.10	0.10	0.20	20.4
CRG	142	-0.97	-0.68	0.29	54.9
HLD	142	0.59	0.59	0.00	35.1
GRM	142	-0.42	-0.16	0.25	18.3
PAR	142	0.19	0.49	0.30	29.6
SOP	142	-0.23	-0.35	0.00	29.2
MON	142	0.74	0.72	-0.01	25.5
BTO	142	-0.20	-0.18	0.01	25.7
LED	142	0.30	0.30	0.00	29.5
WIG	142	-0.69	-0.39	0.29	18.9
SFK	142	-0.15	-0.15	0.00	28.0
CCR	142	1.02	1.02	0.00	34.6
LIZ	142	-1.48	-1.02	0.46	16.7
YUM	142	-0.40	-0.28	0.12	24.1
LMN	142	-0.94	-0.62	0.32	18.6
BLA	142	0.02	0.02	0.00	34.3
WSG	142	2.62	2.60	-0.02	2.8
CES	142	-0.89	-0.89	0.00	9.5
PKS	142	-0.94	-0.94	0.00	25.4
CRG	146	-0.34	0.04	0.38	13.4
HLD	146	0.64	0.64	0.00	5.8
KRM	146	-1.47	-1.29	0.18	12.0

Table 3. δt^* Data and Information (continued)

Station Name	Event Num	Original δt^*	δt^* corrected	δt^* correction	SN
SOP	146	-0.08	-0.16	0.00	30.3
BTO	146	0.06	0.15	0.09	37.0
MON	146	0.75	0.76	0.01	10.1
LED	146	2.01	2.01	0.00	6.1
WIG	146	-1.43	-1.01	0.42	11.7
CCR	146	1.28	1.28	0.00	13.4
LIZ	146	-1.91	-1.33	0.57	12.1
SFK	146	-0.22	-0.22	0.00	12.2
YUM	146	-0.94	-0.70	0.24	5.7
LMN	146	-1.04	-0.59	0.45	4.5
BLA	146	1.08	1.08	0.00	11.4
ORD	146	0.07	0.28	0.21	9.9
PKS	146	-0.69	-0.69	0.00	7.6
PKS	147	0.29	0.29	0.00	38.8
WSG	147	0.53	0.50	-0.03	19.1
CES	147	-2.04	-2.04	0.00	19.2
ORD	147	0.58	0.64	0.06	4.8
BLA	147	-0.60	-0.60	0.00	13.2
LMN	147	-0.72	-0.43	0.28	13.2
YUM	147	-0.71	-0.62	0.09	17.1
CCR	147	0.36	0.36	0.00	20.4
LIZ	147	0.15	0.61	0.46	13.1
WIG	147	-0.40	-0.15	0.25	13.7
LED	147	-0.17	-0.17	0.00	11.0
BTO	147	1.46	1.45	-0.01	15.0
SOP	147	-0.07	-0.18	0.00	15.7
KRM	147	0.02	0.06	0.04	14.7
GRM	147	-0.12	0.09	0.21	16.0
HLD	147	-0.19	-0.19	0.00	20.6
MGP	147	0.32	0.47	0.15	14.3
MGP	161	-0.03	-0.02	0.01	32.6
HLD	161	0.36	0.36	0.00	96.8
KRM	161	0.21	0.20	-0.01	71.8
SOP	161	0.29	0.29	0.00	66.8
MON	161	0.10	0.08	-0.01	70.3
BTO	161	-0.24	-0.27	-0.03	84.8
LED	161	0.16	0.16	0.00	41.1
GUN	161	0.58	0.58	0.00	15.6
WIG	161	-0.19	-0.14	0.05	48.4
SFK	161	0.17	0.17	0.00	44.3
LIZ	161	-0.67	-0.48	0.19	9.3
YUM	161	0.04	0.04	0.00	26.2
LMN	161	-0.37	-0.31	0.06	47.6
CRG	161	-0.87	-0.53	0.34	27.8

Table 3. δt^* Data and Information (continued)

Station Name	Event Num	Original δt^*	δt^* corrected	δt^* correction	SN
ORD	161	0.33	0.32	-0.01	27.3
WSG	161	0.72	0.70	-0.02	17.8
PKS	161	0.32	0.32	0.00	42.3
MGP	165	0.17	0.23	0.06	2.8
CRG	165	-0.61	-0.15	0.46	6.3
HLD	165	2.41	2.41	0.00	6.0
KRM	165	0.45	0.43	-0.02	5.6
SOP	165	-0.41	-0.49	0.00	3.6
MON	165	0.82	0.79	-0.03	6.9
BTO	165	0.08	0.03	-0.05	6.8
LED	165	0.72	0.72	0.00	2.9
GUN	165	0.88	0.88	0.00	3.2
DGO	165	-3.54	-3.51	0.03	7.0
WIG	165	-0.87	-0.70	0.17	3.6
SFK	165	0.70	0.70	0.00	7.4
YUM	165	-0.18	-0.16	0.02	5.3
LMN	165	-0.39	-0.19	0.20	8.1
PKS	165	-0.17	-0.17	0.00	2.4
MGP	171	-0.18	0.01	0.19	12.8
HLD	171	0.62	0.62	0.00	20.5
SOP	171	0.00	-0.11	0.00	3.2
MON	171	0.89	0.87	-0.02	15.1
BTO	171	-0.35	-0.35	0.00	18.9
LED	171	0.83	0.83	0.00	18.1
GUN	171	0.68	0.68	0.00	10.0
WIG	171	-0.98	-0.68	0.29	26.1
SFK	171	-0.23	-0.23	0.00	11.3
YUM	171	-0.72	-0.61	0.11	9.5
LMN	171	-1.25	-0.92	0.33	20.6
PKS	171	0.53	0.53	0.00	7.3
YUM	180	-0.13	0.14	0.27	15.1
WIG	180	-0.07	0.30	0.37	11.2
PKS	180	0.03	0.03	0.00	28.2
BTO	180	0.37	0.52	0.15	55.0
CRG	180	0.01	0.26	0.25	39.4
KRM	180	0.07	0.30	0.23	45.2
MGP	180	-0.65	-0.30	0.34	54.4
LED	180	-0.07	-0.07	0.00	41.4
ORD	180	0.30	0.55	0.25	33.9
GRM	180	-0.17	0.20	0.37	44.7
HLD	180	-0.53	-0.53	0.00	83.4
GUN	180	-3.83	-3.83	0.00	6.2
MON	180	-0.13	-0.09	0.04	85.3
WSG	180	0.14	0.20	0.07	46.4

Table 3. δt^* Data and Information (continued)

Station Name	Event Num	Original δt^*	δt^* corrected	δt^* correction	SN
SFK	180	0.01	0.01	0.00	20.0
MGP	189	0.02	0.15	0.13	6.6
HLD	189	0.41	0.41	0.00	19.1
GRM	189	-0.31	-0.12	0.18	15.7
KRM	189	0.51	0.53	0.02	6.8
MON	189	0.32	0.29	-0.03	17.3
BTO	189	-0.49	-0.52	-0.03	7.6
WIG	189	-0.75	-0.52	0.23	10.0
SFK	189	0.13	0.13	0.00	47.9
LIZ	189	-1.51	-1.07	0.43	7.4
LMN	189	-0.38	-0.11	0.26	4.7
BUR	189	0.04	0.06	0.02	7.9
CES	189	-0.72	-0.72	0.00	6.7
MGP	202	0.08	0.24	0.16	22.1
HLD	202	0.54	0.54	0.00	33.2
GRM	202	-0.20	0.01	0.21	32.7
PAR	202	-0.71	-0.41	0.31	108.9
KRM	202	0.52	0.59	0.07	45.1
YJK	202	0.04	0.18	0.14	17.9
BTO	202	-0.17	-0.14	0.02	79.7
WIG	202	-0.68	-0.43	0.25	17.0
SFK	202	-0.06	-0.06	0.00	59.1
LIZ	202	-1.55	-1.06	0.49	17.3
BUR	202	0.19	0.26	0.07	16.2
CES	202	-0.49	-0.49	0.00	24.4
MGP	229	0.21	0.41	0.20	51.2
GRM	229	-0.38	-0.14	0.24	70.5
PAR	229	-0.23	0.07	0.30	46.2
KRM	229	0.47	0.58	0.11	12.1
MON	229	0.11	0.12	0.01	55.1
SOP	229	-0.16	-0.22	0.00	23.9
BTO	229	-0.20	-0.14	0.06	133.2
LED	229	-0.62	-0.62	0.00	30.7
SHL	233	0.79	0.97	0.18	3.2
BUR	233	-0.52	-0.34	0.18	2.7
YUM	233	-0.27	-0.03	0.24	2.7
WIG	233	0.93	1.37	0.44	3.8
BTO	233	1.65	1.73	0.08	8.9
MON	233	-1.77	-1.77	0.01	8.7
GRM	233	-1.68	-1.27	0.40	5.6
PAR	239	-0.22	-0.05	0.18	4.0
KRM	239	0.86	0.93	0.06	8.1
SOP	239	-1.44	-1.49	0.00	9.9
MON	239	0.13	0.14	0.00	5.8

Table 3. δt^* Data and Information (continued)

Station Name	Event Num	Original δt^*	δt^* corrected	δt^* correction	SN
BTO	239	-0.02	0.01	0.03	19.2
LED	239	-0.19	-0.19	0.00	8.4
SFK	239	-1.13	-1.13	0.00	7.2
WIG	239	0.56	0.71	0.15	5.2
LMN	239	-0.07	0.09	0.16	5.7
SHL	239	-0.12	-0.06	0.06	10.6
PKS	239	1.14	1.14	0.00	11.7
MGP	251	-0.24	-0.01	0.23	18.4
HLD	251	0.05	0.05	0.00	28.3
GRM	251	-0.18	0.11	0.29	39.5
KRM	251	1.20	1.30	0.10	11.0
SOP	251	-0.21	-0.35	0.00	25.7
MON	251	0.63	0.62	-0.01	19.2
LED	251	0.22	0.22	0.00	16.2
GUN	251	0.60	0.60	0.00	19.1
WIG	251	-0.84	-0.51	0.33	17.1
YUM	251	-0.43	-0.28	0.15	12.7
LMN	251	-0.81	-0.46	0.36	17.0
BUR	251	-0.96	-0.86	0.10	5.3
SHL	251	-0.16	-0.06	0.10	13.8
CES	251	-0.15	-0.15	0.00	4.4
PKS	251	0.05	0.05	0.00	20.1
KRM	293	0.73	0.81	0.08	3.7
LMN	293	-0.73	-0.43	0.30	3.7
GUN	293	-0.38	-0.38	0.00	11.2
BLA	293	0.63	0.63	0.00	4.6
GUN	306	0.66	0.66	0.00	5.7
SFK	306	-0.15	-0.15	0.00	4.4
LMN	306	-1.56	-1.26	0.31	7.4
BLA	306	1.17	1.17	0.00	2.5
PKS	306	0.23	0.23	0.00	14.3
BTO	323	0.44	0.44	0.00	4.1
SFK	323	-0.17	-0.17	0.00	6.3
MON	323	-0.19	-0.21	-0.01	3.6
MON	326	0.75	0.73	-0.02	11.5
BTO	326	0.20	0.21	0.00	15.7
GUN	326	0.88	0.88	0.00	8.6
SFK	326	1.21	1.21	0.00	3.0
LIZ	326	-1.38	-0.88	0.49	7.2
BLA	326	1.81	1.81	0.00	6.6
LMN	326	-1.72	-1.40	0.32	11.4
BUR	326	-1.48	-1.42	0.06	7.5
CES	326	-0.39	-0.39	0.00	4.4
MON	330	0.38	0.37	-0.01	9.9

Table 3. δt^* Data and Information (continued)

Station Name	Event Num	Original δt^*	δt^* corrected	δt^* correction	SN
BTO	330	0.05	0.08	0.03	26.8
GUN	330	0.21	0.21	0.00	11.5
SFK	330	-0.33	-0.33	0.00	14.9
LIZ	330	-0.86	-0.43	0.43	8.2
LMN	330	-0.93	-0.60	0.34	6.3
BUR	330	-0.27	-0.17	0.10	10.1
CES	330	0.52	0.52	0.00	10.8
MON	331	1.01	1.01	0.00	31.5
BTO	331	-0.55	-0.53	0.02	31.0
GUN	331	0.13	0.13	0.00	14.8
SFK	331	0.08	0.08	0.00	21.8
LIZ	331	-0.88	-0.12	0.76	15.2
BLA	331	0.52	0.52	0.00	32.6
LMN	331	-1.58	-1.24	0.34	43.6
BUR	331	0.01	0.08	0.07	21.3
SHL	331	-0.37	-0.30	0.07	4.6
CES	331	0.79	0.79	0.00	21.5
MON	333	1.07	1.07	0.00	7.1
BTO	333	-0.25	-0.21	0.04	24.1
GUN	333	-0.24	-0.24	0.00	7.7
SFK	333	0.62	0.62	0.00	6.7
LIZ	333	-2.18	-1.40	0.78	21.5
BLA	333	0.15	0.15	0.00	5.1
LMN	333	-1.94	-1.59	0.35	5.7
BUR	333	0.50	0.59	0.10	14.8
SHL	333	2.10	2.19	0.10	2.9
CES	333	1.42	1.42	0.00	13.3
MON	335	0.15	0.13	-0.01	3.5
BTO	335	0.82	0.84	0.02	13.1
SFK	335	0.27	0.27	0.00	2.8
LIZ	335	-0.50	0.08	0.58	4.3
LMN	335	-1.42	-1.03	0.38	17.7
BUR	335	-0.49	-0.40	0.10	14.2
CES	335	1.75	1.75	0.00	6.5
MON	342	0.80	0.80	0.00	19.6
BTO	342	-0.87	-0.83	0.04	17.7
GUN	342	0.06	0.06	0.00	7.1
SFK	342	0.20	0.20	0.00	13.1
BLA	342	0.48	0.48	0.00	8.7
BUR	342	-1.07	-0.97	0.10	5.3
PKS	342	-0.36	-0.36	0.00	8.9
PKS	355	1.00	1.00	0.00	17.1
SHL	355	-1.46	-1.45	0.01	3.7
BUR	355	0.98	0.99	0.01	8.8

Table 3. δt^* Data and Information (continued)

Station Name	Event Num	Original δt^*	δt^* corrected	δt^* correction	SN
LMN	355	-1.12	-1.09	0.03	12.5
BTO	355	-0.95	-0.95	0.00	7.2
PKS	359	0.24	0.24	0.00	7.5
ORD	359	-0.59	-0.58	0.01	10.3
BLA	359	0.55	0.55	0.00	15.3
LMN	359	-0.31	-0.23	0.08	9.2
LIZ	359	-0.40	-0.22	0.18	9.2
BTO	371	0.61	0.66	0.04	35.3
LIZ	371	-0.75	-0.21	0.54	10.1
LMN	371	-0.63	-0.21	0.42	12.5
ORD	371	-0.35	-0.19	0.16	9.9
CES	371	-1.65	-1.65	0.00	6.6
PKS	371	-0.44	-0.44	0.00	14.8
PKS	405	0.05	0.05	0.00	3.7
LMN	405	-0.05	0.13	0.19	5.4
LIZ	405	-1.22	-0.88	0.34	4.6
BTO	405	0.28	0.26	-0.02	12.8
BTO	412	0.18	0.24	0.07	4.0
LIZ	412	0.79	1.66	0.86	1.7
LMN	412	-1.25	-0.67	0.58	2.3
PKS	412	-1.05	-1.05	0.00	2.2
SHL	436	1.49	1.54	0.05	6.4
SFK	436	-0.30	-0.30	0.00	27.0
LMN	436	-0.45	-0.19	0.26	16.0
BTO	436	0.05	0.05	0.00	18.5
LMN	437	0.50	0.77	0.27	3.7
BTO	437	1.63	1.67	0.04	2.6
SFK	437	-3.47	-3.47	0.00	2.1
BTO	442	0.63	0.66	0.02	3.4
SFK	442	1.56	1.56	0.00	2.0
LMN	442	-1.18	-0.84	0.34	5.6
SHL	442	-0.52	-0.44	0.09	1.6

2.4 δQ^{-1} INVERSION

Solving for differential attenuation is a relatively straightforward inverse problem. Relative t^* is related to attenuation, Q^{-1}, through the following expression:

$$\delta t^* = \int_S Q_R^{-1} d\tau_R - \int_S Q_S^{-1} d\tau_S \tag{6}$$

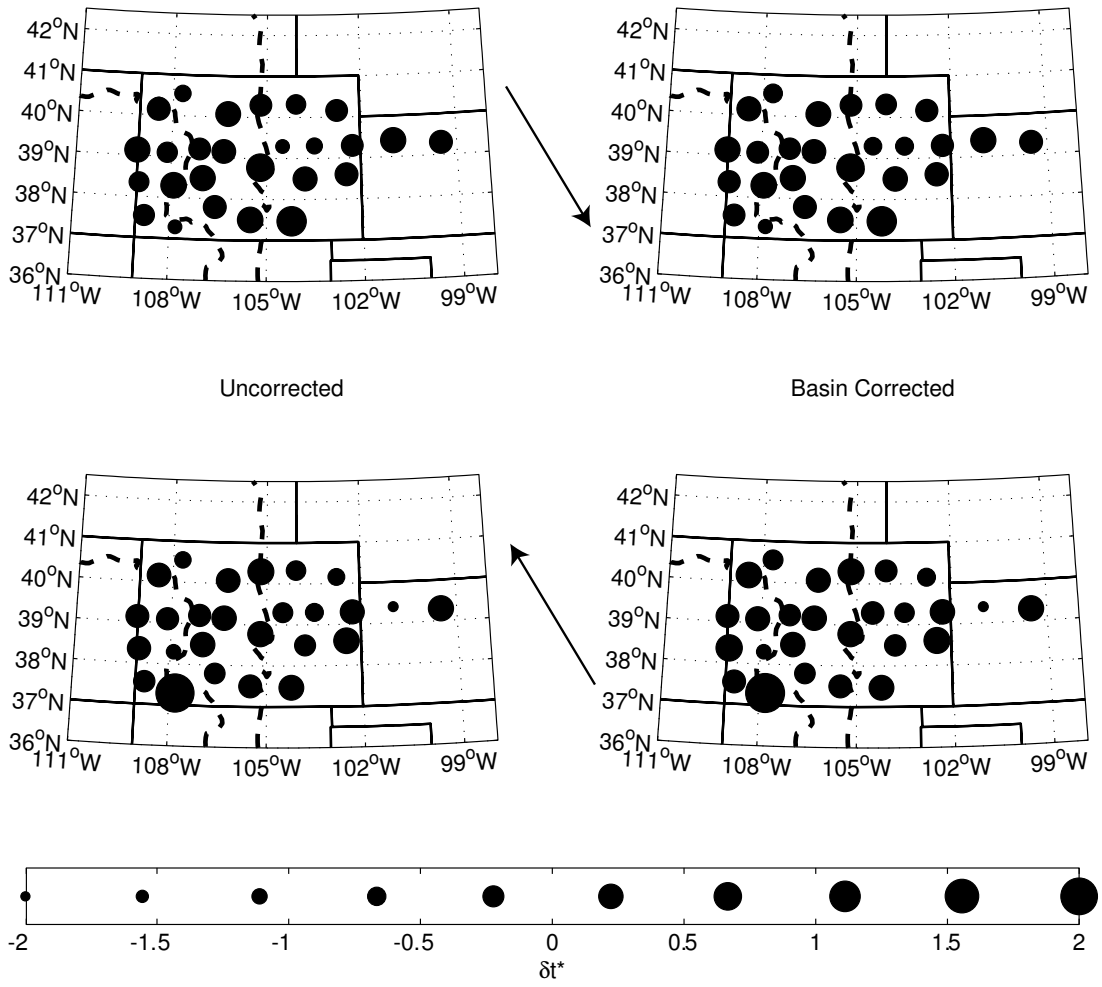

Figure 6. Weighted average δt* maps for events originating from the northwest (top) and southeast (bottom) for uncorrected (left) and sediment corrected (right) values of δt*. The weight is the inverse of the expected standard deviation of δt* due to random noise (Appendix 1.2). Symbols are placed at station locations. Larger symbols indicate greater δt^*.

where τ is the travel time. As before, the subscripts S and R refer to the station and reference respectively. δt^* is the difference in the integrated effect of energy loss along the ray path between a reference trace and a station trace. In order to turn (6) into a tractable inverse problem, we assume that $d\tau_R = d\tau_S = d\tau$ such that

$$\delta t^* = \int \Delta Q^{-1} d\tau \tag{7}$$

where

$$\Delta Q^{-1} = Q_R{}^{-1} - Q_S{}^{-1} . \tag{8}$$

We use the δt^* measurements, the ray path derived from 2-D ray tracing and the western U.S. one dimensional velocity model, TNA [*Grand and Helmberger*, 1984], to invert for variations in Q^{-1} in the study area. We assume that variations in Q^{-1} between seismic rays for a given event are confined to the upper 400 km of the mantle.

Singular value decomposition [*Menke*, 1984] is used to do the inversion. Equation 7 can be written in the form

$$\delta t_i^* = \sum_M d\tau_{ij} \Delta Q_i^{-1} \tag{9}$$

where δt_i^* is the data vector consisting of N δt^* measurements, ΔQ_j^{-1} is the model vector of differential attenuation in each of M blocks, and $d\tau_{ij}$ is the data kernel matrix with ray path travel time information. Singular value decomposition seeks a solution to

$$\Delta Q^{-1} = d\tau^{-1} \delta t^* \tag{10}$$

where

$$d\tau^{-1} = D_p \Lambda_p M_p^T . \tag{11}$$

Equation 11 is referred to as the natural generalized inverse. It is composed of D, a matrix of eigenvectors that span the data space, M, a matrix of eigenvectors that

span the model space, and Λ, a matrix of eigenvalues whose diagonal elements are the singular values. The parameter p corresponds to the number of largest singular values kept when calculating $d\tau^{-1}$. In our case we have chosen to use all singular values within two orders of magnitude of the largest. Using only the largest p singular values is referred to as a truncated singular value decomposition (TSVD) and is equivalent to damping the solution, reducing model variance at the expense of model resolution.

In order to reduce the adverse effects of significant random noise, we use a weighted TSVD where the weights, W, are the inverse of the standard deviation of δt^* error due to normally distributed random noise (Appendix 1.1) [*Meju*, 1994]. Multiplying both sides of (9) by W, we have

$$W\delta t^* = Wd\tau\Delta Q^{-1}. \tag{12}$$

We now seek a solution to

$$\Delta Q^{-1} = (Wd\tau)^{-1} W\delta t^*. \tag{13}$$

The eigenvectors and eigenvalues of equation (11) are now found for the quantity $(Wd\tau)^{-1}$. The inversion is solved for average attenuation values in $100 \times 100 \times 100$ km bins extending from 113.7°W to 96°W, 33.7°N to 43.6°N, and 0 to 400 km depth. The bins are offset by 10 km in each direction and the inversion is repeated, producing a total of 1000 inversions. This procedure is done twice. In the first iteration, a solution for the event mean is included. In the second, the 1000 estimates of the event mean from the first iteration are averaged, removed from the δt^* data,

and the inversion is performed again without the solution for the event mean. The inversions are sequentially combined, generating a psuedo-effective resolution of 10 km, and smoothed by convolving the model with a $200 \times 200 \times 50$ km unit box.

For regions in the model with a resolution derived from the resolution matrix (A2.1) greater than 0.3, the range in ΔQ^{-1} is 0.04. The variance reduction of the corrected δt^* data due to the resulting model is 10%, a value that is expected given the amount of random error in δt^* (Appendix 2). Romanowicz [1995] reports a variance reduction of 49% for her global model of upper mantle shear wave attenuation, a value approaching the variance reduction achieved in velocity tomography. Reid et al. [2001] generate a variance reduction of 23% in their upper mantle shear wave Q model while their velocity model is able to produce a variance reduction of 67%.

The ray path travel times are calculated using a one-dimensional velocity model. Because of this assumption, the resulting Q^{-1} model is incorrect by an amount approximately equal to the fractional difference between the one-dimensional velocity model and the true Earth velocity structure. For example, where the Earth velocities are 5% lower than the one-dimensional velocities, the actual Q^{-1} model should also be reduced by 5%. A competing effect not accounted for is that due to focusing and defocusing of the seismic energy from lateral velocity heterogeneities. Our analysis of this phenomenon suggests that when using our technique for measuring t^* and the velocity perturbations of Lee and Grand, Q^{-1} will decrease by less than 5% in regions of low velocity (focusing) and increase by less than 5% in regions of high velocity (defocusing). These regions will be flanked by decaying

oscillations of high and low Q^{-1}. Work by Allen et al. [1999] indicates that focusing/defocusing effects on t^* in the vicinity of the Icelandic plume could be more than two orders of magnitude larger than those determined here. The difference is primarily due to the potentially small radius of the Iceland plume, 100 km, its vertical orientation, and its large shear velocity anomaly, -12%. We calculate that the combined errors due to the focusing/defocusing and ray path travel time effects are minimal.

Figure 7 provides horizontal slices of the resulting differential shear wave attenuation model. When basin corrections are not applied, the negative attenuation anomalies correlate very well with the positions of the basins. The primary feature of this corrected model is the large relative attenuation trending north-northwest directly beneath the eastern Colorado Rockies. This feature extends to around 150 km depth and coincides with a modest decrease in shear wave velocity (Figure 1). An anomalous region exists just to the west where a decrease in attenuation coincides with the lowest velocities. Is this relationship a consequence of the high temperature side of an attenuation peak or compositional variability? At greater depths, the correlation to features at shallow levels disappears.

2.5 THE PHYSICAL STATE OF THE UPPER MANTLE

To fully appreciate these results, attenuation measurements are combined with velocity measurements [*Roth et al.*, 2000; *Anderson*, 1989; *Nowick and Berry*, 1972]. This analysis can be used to estimate the temperature [*Karato*, 1993; *Sato and Ryan*, 1994; *Goes et al.*, 2000], percent partial melt [*Hammond and Humphreys*, 2000b;

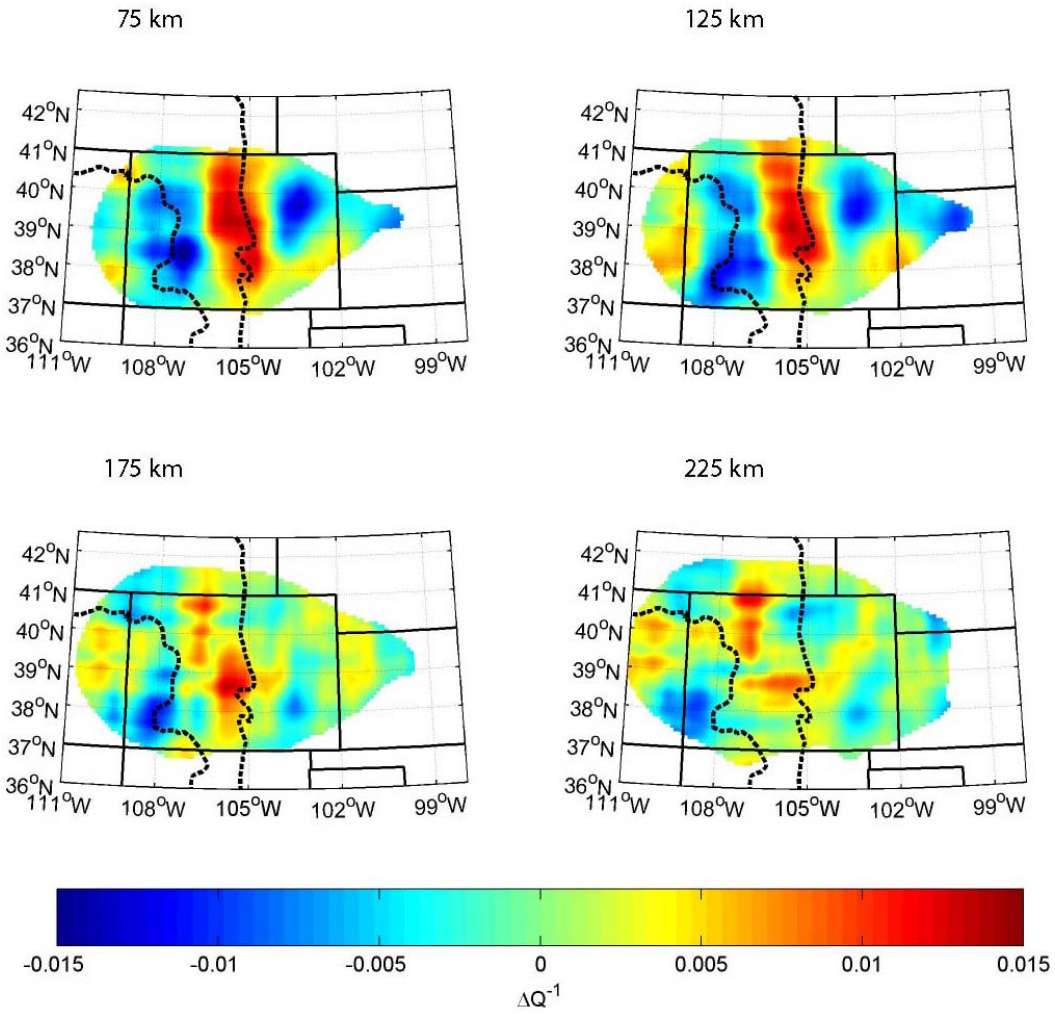

Figure 7. Differential attenuation tomography results at four depths. Relatively strong attenuation occurs beneath the eastern Rocky Mountains to depths of ~150 km and trends north from the Rio Grande Rift.

Hammond and Humphreys, 2000a; *Sato and Ryan*, 1994], and composition [*Karato and Jung*, 1998; *Duffy and Anderson*, 1989] of the material through which the seismic wave has passed. Most regional velocity studies have either assumed a constant one dimensional Q profile with depth or assumed a simple relationship between velocity and Q [*Goes et al.*, 2000; *Sobolev et al.*, 1996]. Not knowing the true value of Q or its relationship to temperature, frequency, or velocity can be detrimental in the interpretation of sub-surface anomalies.

Based on laboratory experiments [*Jackson*, 1993], attenuation is commonly observed to follow a power-law relationship where Q is proportional to angular frequency, w, raised to some positive power α. This model is believed to be due to the movement of dislocations having a range of thermally activated strengths and relaxation times and/or activation energies encompassing periods of at least 10^{-1} to 10^{2} seconds. Minster and Anderson [1981] proposed that there should be a minimum and maximum relaxation time spanning two to three decades in frequency. Above and below these values, attenuation is predicted to drop off to zero and produce an attenuation band or peak [*Nowick and Berry*, 1972]. Anderson and Given [1982] presented frequency dependent attenuation results in the mantle to which they ascribed an attenuation band, but their results as to the maximum and minimum relaxation times was inconclusive. From frequency dependent t^* measurements, Warren and Shearer [2000] are unable to conclusively observe an attenuation band but are able to state that attenuation decreases with increasing frequency.

2.5.1 Effects of Composition

The relationships between the shear attenuation model and shear velocity model are presented in Figure 8. The relative shear velocity model is converted to absolute velocities by assuming the values given by Lee and Grand [1996] are relative to PREM and that the average shear velocities in the model below 250 km depth are equal to PREM. To make this comparison and perform the analysis below, we must also assume that the frequencies used to measure velocity and attenuation are the same, ~0.06 Hz.

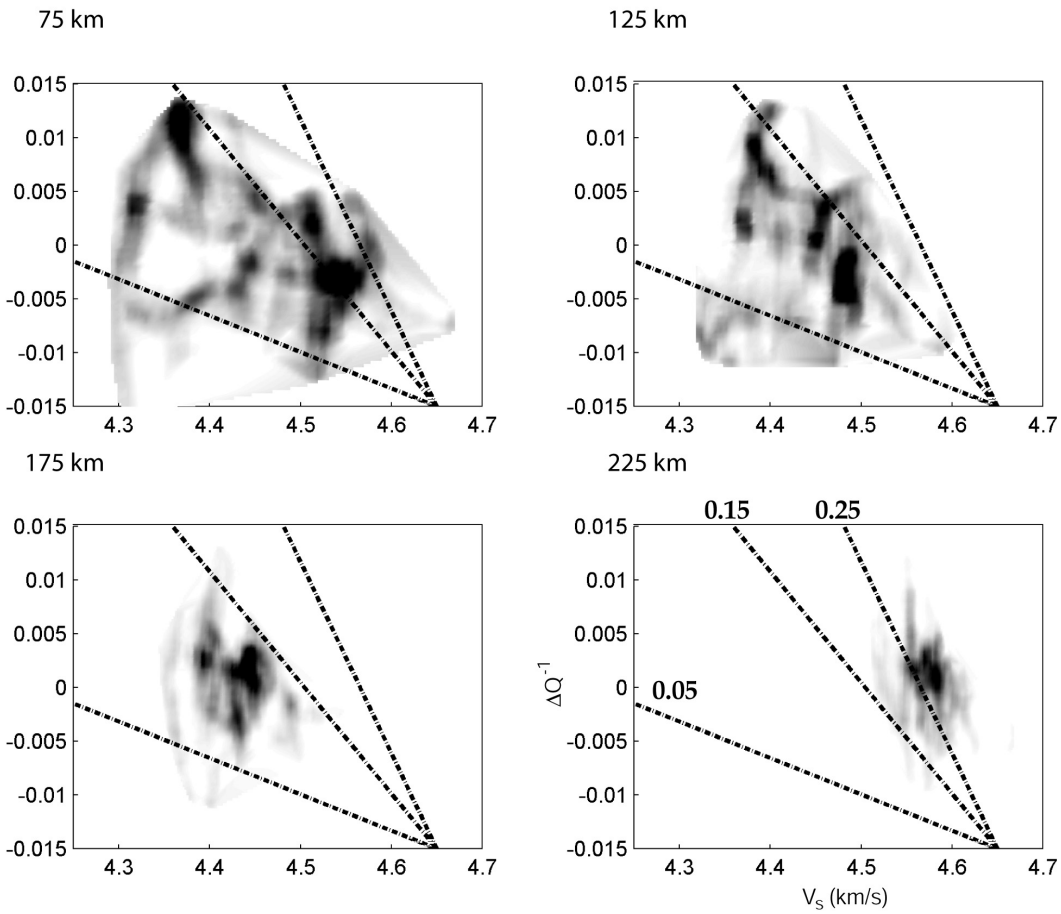

Figure 8. Velocity versus relative attenuation for four depths. The gray scale is proportional to the number of model points having that velocity and attenuation, a 2-D histogram. The dashed-dot lines are plots of velocity versus attenuation according to equation 14 for different values of α. Movement along a line is due to changing temperature while movement across a line is due to changing V_U or composition. Seismological studies have found α equal to 0.15 [*Warren and Shearer*, 2000; *Sobolev et al.*, 1996] while laboratory experiments have found α between 0.2 and 0.3 [*Karato and Spetzler*, 1990].

Compositional and thermal effects can result in a given value of attenuation and velocity. If we assume that Q has a positive power law dependence with respect to frequency ($\alpha > 0$), Minster and Anderson [1981] provide the following relationship between velocity and attenuation

Table 4. Density – Velocity Relationships

R	$\frac{\partial \ln \rho}{\partial \ln V_S}$	$\frac{\partial \ln \rho}{\partial \ln V_P}$	$\frac{\partial \ln V_S}{\partial R}$	$\frac{\partial \ln V_P}{\partial R}$	$\frac{\partial \ln V_S}{\partial \ln V_P}$
1	-0.98	-1.58	0.27	0.17	1.6
2	0.66	0.46	-0.01	0.02	0.7
3	0.38	0.46	-0.07	-0.06	1.2
4	0.30	0.40	-0.63	-0.47	1.3
5	0.31	0.58	-0.92	-0.48	1.9
6	0.86	0.57	0.10	0.14	0.7
7	0.14 to 0.43	0.15 to 0.53	-2.32×10^{-4} to -0.76×10^{-4}	-2.18×10^{-4} to -0.62×10^{-4}	1.1 to 1.2
8	0.03	0.06	-7.90	-3.60	2.2
9	-0.01	-0.02			2.8

Table 4. Density-velocity relationships for various conditions corresponding to a pressure of 3 GPa and temperature of 1240 K or ~ 100 km depth. R is the reaction number corresponding to the following scenarios: 1. Increasing Mg# (Mg/(Mg + Fe)) [*Griffin et al.*, 1999], 2. Increasing garnet at the expense of orthopyroxene and corundum [*Aranovich and Berman*, 1997], 3. Increasing phlogopite at the expense of garnet (above 4.5 GPa) [*Sato et al.*, 1997], 4. Increasing phlogopite at the expense of olivine (below 4.5 GPa) [*Sato et al.*, 1997], 5. Increasing antigorite at the expense of olivine [*Bromiley and Pawley*, 2003], 6. Formation of olivine and garnet at the expense of orthopyroxene and spinel [*Danckwerth and Newton*, 1978], ∂R expressed as an increase in the fraction of olivine, 7. Rising temperature where the upper number results from a quality factor of 50 and the lower number results from an infinite quality factor [*Karato*, 1993], 8. Increasing partial melt [*Hammond and Humphreys*, 2000b], and 9. Increasing partial melt with depletion of iron [*Humphreys and Dueker*, 1994]. ∂R is the fractional increase of the appropriate mineral (R 1-6), change in temperature (R 7) having units of K, or fractional increase in partial melt. For reactions 1-6, values were obtained using the method of Bina and Helffrich [1992] and Holland and Powell [1998] and the mineralogical data of Hacker et al. [2003]. Values for reaction 7, changes in temperature, were obtained from Karato [1993]. Values for melt were obtained from Hammond and Humphries[2000b] assuming $\partial \ln\rho/\partial R$ is -0.2 [*Humphreys and Dueker*, 1994] and the following relationship for melt with depletion of iron in the residuum

$$\frac{\partial \ln \rho}{\partial \ln V} = \frac{A\left\{\partial \ln \rho / \partial \ln V\right\}_{\alpha} + \left\{\partial \ln \rho / \partial \ln V\right\}_{\beta}}{A+1}$$

where α represents values for melt and β represents values for depletion of iron. A is equal to

$$A = \frac{\left\{\partial \ln V / \partial R\right\}_{\alpha}}{\left\{\partial \ln V / \partial R\right\}_{\beta}}.$$

$$V_S(w) \approx V_U\left[1-\frac{1}{2}\cot\frac{\alpha\pi}{2}Q_S^{-1}(w)\right]. \quad (14)$$

V_U is the unrelaxed shear velocity due either to sufficiently high frequency or low temperature where anelastic mechanisms do not have time or energy to operate. The unrelaxed velocity depends primarily on composition. For example, the fractional change in the unrelaxed shear velocity relative to the fractional change in the iron content for Proterozoic sub continental lithospheric mantle (SCLM) [*Griffin et al.*, 1999], $\partial \ln V_S / \partial X_{Fe}$, is approximately -0.3 (Table 4). A 1% decrease in iron content increases the shear velocity by 0.3%. Decreasing iron content, an effect that accompanies older and more mature SCLM and the melting of mantle peridotite, increases the seismic velocity. Another compositional effect that can change shear velocity is simply the bulk mineralogy. More mature SCLM typically has less garnet and more olivine. In going from the Phanerozoic to Archean compositions reported by Griffin et al. [1999] where garnet decreases by 4% and olivine increases by 3%, shear velocity increases by 5%.

If the relationship provided by Minster and Anderson is correct and we know α, then we can use velocity and attenuation models to solve for changes in V_U, an indicator of compositional variation. Values for α measured in the laboratory on polycrystalline aggregates under upper mantle conditions at seismic frequencies range from 0.2 to 0.3 [Karato and Spetzler, 1990]. Seismological estimates for α are on the order of 0.15 [Warren and Shearer, 2000; Sobolev et al., 1996].

The straight lines in Figure 8 represent different values of α in equation 14. For the upper layers at 75 and 125 km depth, the overall trend in the data shows low

values of α, on the order of 0.15. If we examine the slope of the smaller scale trends and trends at greater depth, 175 and 225 km, we see that the slope increases to values of α closer to 0.25. We therefore examine compositional variability by rearranging equation 14, using the V_S and Q^{-1} models and assuming α equals 0.25, and solving for the percent change in unrelaxed shear velocity, $\%\Delta V_U$. The resulting compositional models presented below do not change significantly for α equal to 0.15.

Figure 9 contains horizontal slices of the relative unrelaxed shear velocity. Unrelaxed shear velocities tend to increase gradually to the east and may reflect temperature dependent phase changes such as the reactions in Table 4. Application of equation 14 predicts very low unrelaxed shear velocities beneath the southwestern Colorado Rocky Mountains. If this were partial melt and the local fluid flow attenuation mechanism were operating [*Hammond and Humphreys*, 2000b; *Hammond and Humphreys*, 2000a], we would see relatively low unrelaxed velocities. A shear velocity reduction of 6.5% would indicate 0.8% partial melt (Table 4). But conventional models of attenuation in which attenuation simply increases with temperature suggest that attenuation would remain high since high temperatures would presumably be needed to produce partial melt. Since the shear wave attenuation has dropped considerably, we have either observed a very unusual composition or the high temperature side of an attenuation peak [*Anderson and Given*, 1982]. If we are in fact on the high temperature side of an attenuation peak, equation 14 no longer holds in this region and unrelaxed velocities are greater than presented in Figure 9. After assessing the possible changes in temperature, we will return to the question of composition.

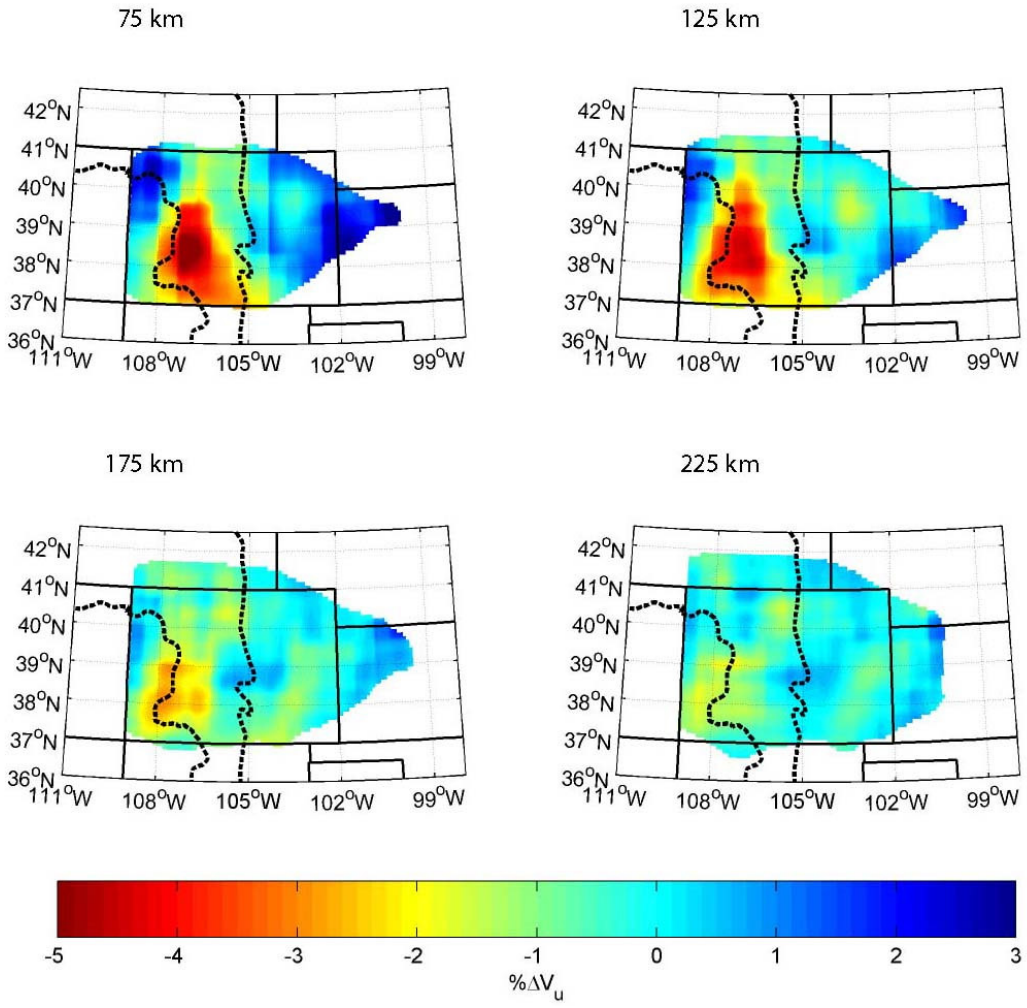

Figure 9. Unrelaxed shear velocity at four depths. Unrelaxed shear velocity gradually increases to the east from the Colorado Rockies. A significant drop in unrelaxed shear velocity occurs beneath the southwest Colorado Rocky Mountains and may indicate either high temperatures and an attenuation peak or unusual compositions.

2.5.2 Effects of Temperature

We can calculate changes in temperature for the case of either unusual composition or the high temperature side of an attenuation peak. We adopt the relation for the temperature derivative with respect to shear velocity given by Karato [1993] including effects of pressure,

$$\frac{\partial \ln V_S(\omega)}{\partial T} = \frac{\partial \ln V_U}{\partial T} - F(\alpha)\frac{Q^{-1}(\omega)}{\pi}\frac{H^* + PV^*}{RT^2}. \quad (15)$$

$\partial \ln V_U/\partial T$ is the normalized derivative of the shear velocity with respect to temperature for the unrelaxed state. From 50 to 400 km depth, $\partial \ln V_U/\partial T$ for olivine, assumed to be the dominant mineral in the upper mantle for this region, is approximately -0.76 x 10^{-4} K^{-1} [*Karato*, 1993]. ω is the angular frequency. $F(\alpha)$ is a constant related to the frequency dependence of attenuation where Q is proportional to ω^{α}. $F(\alpha)$ is given by

$$F(\alpha) = \frac{\pi\alpha}{2}\cot\frac{\pi\alpha}{2}. \quad (16)$$

Again we choose $\alpha = 0.25$ which gives $F(\alpha) = 0.95$. As α goes to 0, $F(\alpha)$ goes to 1. A larger value of α reduces the dependence of (15) on Q. H^* is the activation energy of the thermally activated process, V^* is the activation volume, P is the pressure, R is the gas constant and T is the reference temperature. We use H^* = 500 kJ/mol, the activation energy for the diffusion of oxygen through olivine [*Karato and Spetzler*, 1990]. The activation volume, V^*, controls how pressure affects the activation energy. We use V^* = 4 x 10^{-6} m^3/mol [*Anderson*, 1989]. The pressure in the mantle is taken from PREM [*Dziewonski and Anderson*, 1981] and the reference temperature is taken from the geotherm reported by Stacey [1992], ~1200 to 1800 K from 50 to 400 km depth.

This formulation requires absolute attenuation. In addition, to account for composition, we must consider $\delta \ln V_S$ for velocities relative to the unrelaxed shear velocity, $(V_S - V_U)/V_U$, for which the calculation of V_U also requires absolute

attenuation. We determine absolute attenuation by assuming that the smallest absolute attenuation in our model is close to zero and add a constant value to our differential attenuation model. We add 0.015 to our relative attenuation model and require attenuation to be positive and greater than 0.005. The requirement that absolute attenuation be greater than 0.005 is done only to inhibit extreme changes in temperature.

We must now consider two cases when applying (15) to derive changes in temperature. The first case assumes that the power-law relation between velocity and attenuation, equation 14, holds in all regions and that the composition of the upper mantle beneath the southwest Colorado Rocky Mountains is unusual. In this case, changes in temperature derived from equation 15 are independent of velocity since the fractional change in velocity becomes a function of only attenuation,

$$\Delta \ln V_S = -\frac{1}{2} \cot \frac{\alpha \pi}{2} Q_S^{-1} . \qquad (17)$$

Changes in temperature are then proportional to attenuation with the greatest increase in temperature beneath the eastern Colorado Rocky Mountains (Figure 10a). At 125 km depth, temperatures are elevated to about 80 K greater than the anomalous region to the southwest and only 50 K greater than the Great Plains. For the second case, where the anomalous region is due to an attenuation peak, the unrelaxed shear velocity is not allowed to fall below the highest unrelaxed shear velocity along the boundaries of this anomalous region. Equation 15 for velocity-temperature relations still holds, though for a different value of α as it goes to zero and becomes negative on the high temperature side of the attenuation peak. We continue to use α equals

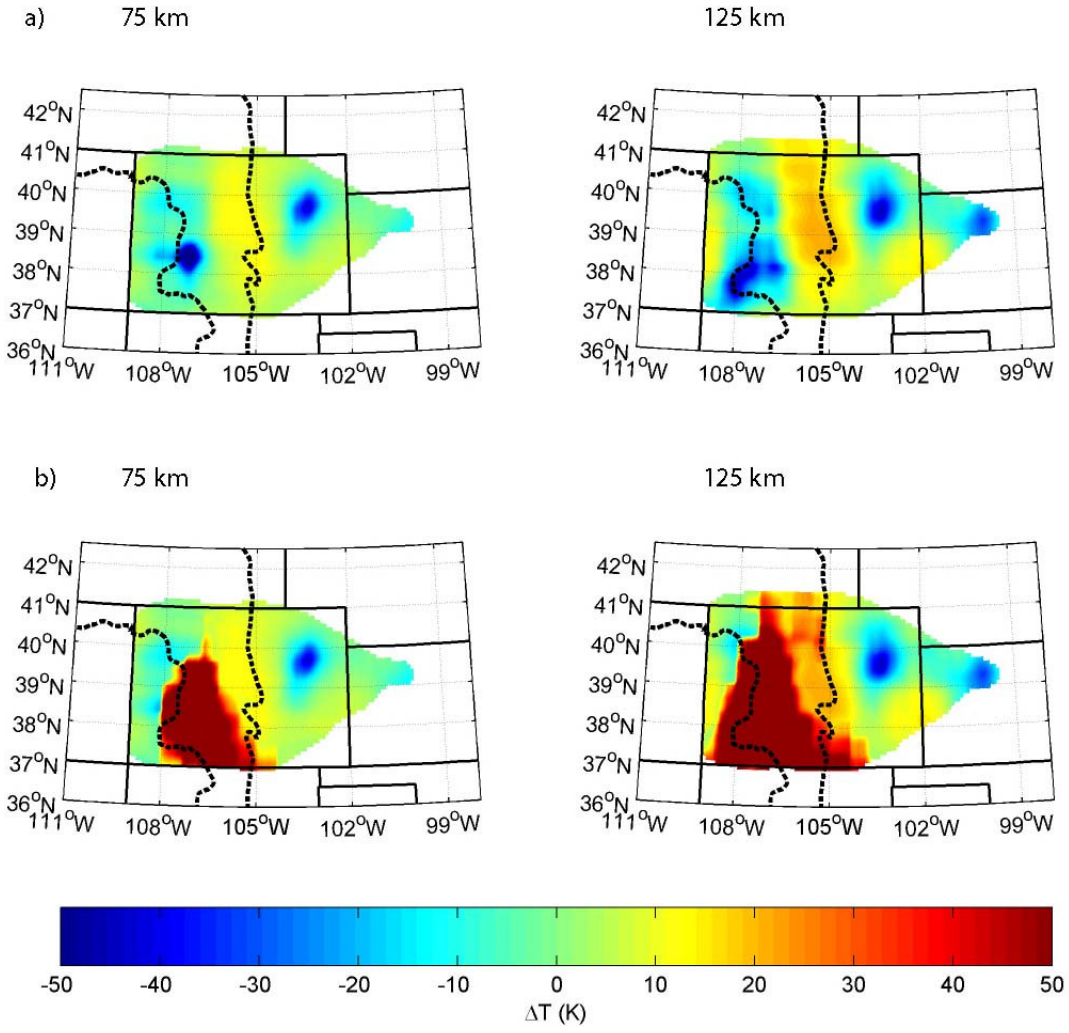

Figure 10. Temperature contrast at 75 and 125 km depth from the use of equation 15. In a) equation 14 holds in all regions, i.e. there is no attenuation peak. Maximum temperature contrasts are limited to elevated values of 80 K at 125 km beneath the eastern Colorado Rockies. In b) equation 14 holds everywhere except in the region of very low unrelaxed shear velocity, i.e. the low velocities beneath southwest Colorado are due to an attenuation peak resulting from very high temperatures. Unrelaxed shear velocity is not allowed to drop below the values on the edge of the anomalously slow region, -2%ΔV_U. Maximum temperature contrasts increase to elevated values of over 300 K at 75 km beneath the southwestern Colorado Rockies.

0.25 and incur a small penalty. For this case, temperatures at 125 km depth beneath the southwest Colorado Rocky Mountains increase by over 300 K (Figure 10b).

2.5.3 Upper Mantle Composition and Isostatic Compensation

An additional constraint to help us differentiate the possible thermal and compositional models is the subsurface density distribution required to support the Rocky Mountains and surrounding regions. We first account for thermal contributions to upper mantle isostacy for the two temperature models and isostatic compensation due to thickened crust [*Li et al.*, 2002] assuming a constant density contrast across the Moho of 400 kg/m^3. We then look for the relationship between density and velocity in the upper mantle that produces the best variance reduction of the residual topography. This relationship is compared to predicted values to estimate the compositional heterogeneity in the upper mantle. The remaining topography, after accounting for the above factors, is due to density anomalies in the crust.

Fractional changes of density with respect to velocity, $\partial \ln \rho / \partial \ln V_S$, are estimated for several different mineral reactions, changes in temperature, and partial melt (Table 4). Density, velocity and thermal expansivity (~ 3.3×10^{-5} K^{-1}) are calculated using the techniques of Bina and Helffrich [1992] and Holland and Powell [1998] and the mineral data compiled by Hacker et al. [2003]. A starting mineral assemblage of preferred Proterozoic SCLM [*Griffin et al.*, 1999] is used and the above values are averaged from 50 to 200 km depth. We compute the mantle thermal component of isostatic compensation using the two differential temperature models described previously while assuming that mass anomalies affecting compensation are confined to between 50 and 200 km depth. The mass needed to compensate the mass deficit in the mantle results in topography having a density of 2700 kg/m^3 [*Snelson et al.*, 1998]. We also calculate the crustal component of isostatic compensation using the

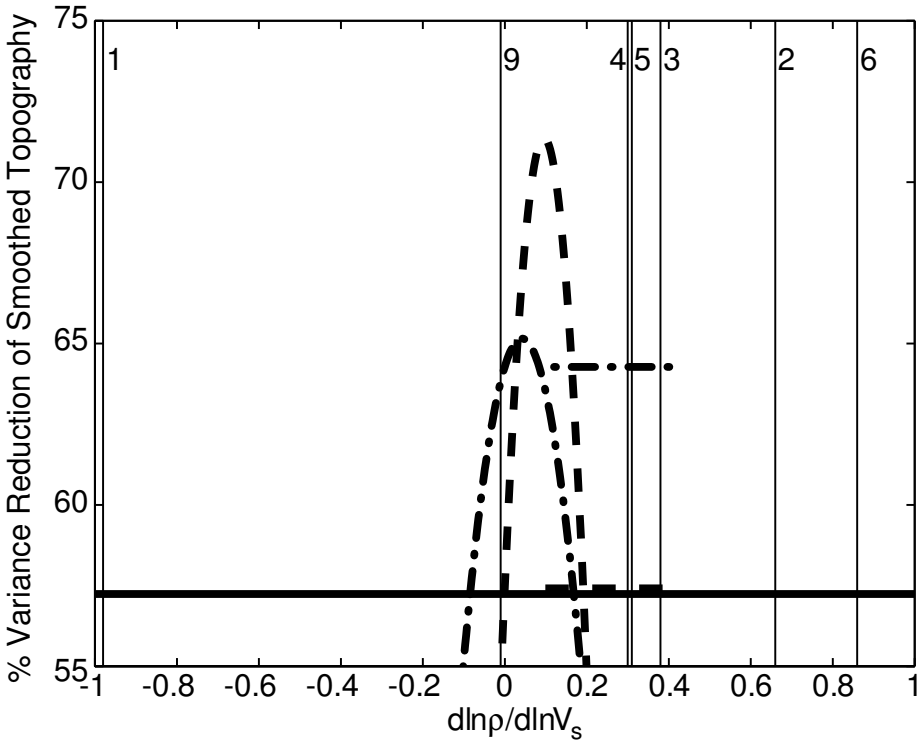

Figure 11. Variance reduction of elevation data versus fractional derivative of density with respect to shear velocity. The solid horizontal line is the variance reduction for thickened crust. The dashed line represents the low temperature model while the dashed-dot line represents the high temperature model. The short horizontal lines indicate the variance reduction due to the addition of thermal effects and span the appropriate range of $\partial \ln \rho / \partial \ln V_S$ for that phenomenon. The curved lines represent the addition of the compositional component of mantle compensation for a range of $\partial \ln \rho / \partial \ln V_S$. The vertical lines are values of $\partial \ln \rho / \partial \ln V_S$ for the different compositional effects in Table 4.

crustal thickness map of Li et al. [2002] and a density contrast across the Moho of 400 kg/m^3.

Figure 11 shows the variance reduction of smoothed topography in dependence on $\partial \ln \rho / \partial \ln V_S$ for the upper mantle due to changes in composition while accounting for upper mantle thermal and crustal thickness contributions. Thickened crust alone accounts for 57% of the topographic variance (solid horizontal line). Up to an additional 7% of the variance can be explained by the thermal variations in the upper

mantle (short horizontal lines spanning their associated values of $\partial \ln \rho / \partial \ln V_S$). Two cases are presented representing the two possible relationships between velocity and attenuation. Each case results in a thermal model and compositional model. The dashed-dot line represents mantle contributions to isostacy when there is an attenuation peak (case 1) while the dashed line represents contributions when attenuation has a simple linear relationship to velocity (case 2). The vertical lines are values of $\partial \ln \rho / \partial \ln V_S$ for the different compositional effects in Table 4. For case 1 where high temperatures coincide with the lowest shear velocities, the thermal model increases the variance reduction by 7%. The compositional counterpart for this case adds little improvement. For case 2 where unusual composition coincides with the lowest shear velocities, the thermal model increases the variance reduction by less than 1% but the corresponding compositional model improves the variance reduction by 14%.

For both relationships between velocity and attenuation, the best $\partial \ln \rho / \partial \ln V_S$ lies somewhere between melt with basalt depletion and the other mineral reactions. Assuming that no Fe/Mg fractionation occurs for reactions 1-6 (Table 4), the measured value of $\partial \ln \rho / \partial \ln V_S$ implies that some melt is present. The high temperature case would make hydrous phases unstable. Antigorite is stable below 1000 K [*Bromiley and Pawley*, 2003] while phlogopite can remain stable up to 1600 K [*Sato et al.*, 1997]. Increasing temperature is likely to drive garnet to orthopyroxene and corundum (reaction 2) [*Aranovich and Berman*, 1997] or garnet and olivine to orthopyroxene and spinel (reaction 6) [*Danckwerth and Newton*, 1978]. These reactions have the correct sense in that higher temperatures produce compositions that

are slower and lighter, however reaction 2 is unlikely to produce a large signal because of its small values of $\partial \ln V_S / \partial R$ (Table 4) and $\partial R / \partial T$ [*Aranovich and Berman*, 1997]. Though the high temperature model with its associated compositional variations produces a consistent interpretation, the second case in which velocity has a simple linear relationship with respect to attenuation produces a better variance reduction. For such a model, elevated temperatures are slight and melt will only be present if the melting temperature has been reduced by the presence of hydrous phases. Antigorite is unlikely to be stable very far below the Moho while phlogopite could be stable throughout most of the mantle lithosphere. The presence of phlogopite in the upper mantle beneath southwest Colorado is consistent with its presence in lamproite dikes in the Colorado Plateau [*Wannamaker et al.*, 2000] and highly potassic magmatism in southwest Colorado [*Mutschler et al.*, 1987].

Researchers have speculated on the presence of phlogopite in the upper mantle beneath southwest Colorado but have not been able to determine its subsurface extent. If we assume that our data is explained by the presence of phlogopite and partial melt, we can derive their proportions from the estimated $\partial \ln \rho / \partial \ln V_S$ in Figure 11, 0.096, and the relations

$$\partial \ln \rho = \{\partial \ln \rho\}_A + \{\partial \ln \rho\}_B \tag{18}$$

$$\partial \ln V_S = \{\partial \ln V_S\}_A + \{\partial \ln V_S\}_B \tag{19}$$

which give

$$\frac{\partial \ln \rho}{\partial \ln V_S} = \left\{\frac{\partial \ln \rho}{\partial \ln V_S}\right\}_A \frac{\{\partial \ln V_S\}_A}{\partial \ln V_S} + \left\{\frac{\partial \ln \rho}{\partial \ln V_S}\right\}_B \frac{\partial \ln V_S - \{\partial \ln V_S\}_A}{\partial \ln V_S} \quad . \tag{20}$$

The subscript *A* denotes reaction 9, melt with depletion, and subscript *B* denotes reaction 4, substitution of olivine with phlogopite. In solving for $\{\partial \ln V_S\}_A / \partial \ln V_S$, the fraction of velocity anomaly due to partial melt, we find that 66% of the velocity anomaly is due to melt and the remainder, 34%, to phlogopite. Using the derivatives of velocity versus phlogopite or melt fraction (Table 4) and the fractional change in the unrelaxed velocity, we conclude that if up to 6% of the unrelaxed velocity anomaly is due to these processes, there is up to 0.5% partial melt and up to 3% substitution of olivine with phlogopite beneath the southwest Colorado Rockies. If the unrelaxed shear velocities beneath southwest Colorado were higher due either to greater anelastic shear velocities or greater attenuation, the value of $\partial \ln \rho / \partial \ln V_S$ for which there is a maximum variance reduction of residual topography would be greater. Because of this and the reduction in the velocity anomaly, there would be less partial melt.

The residual elevation anomaly after accounting for thickened crust and the thermal effects of the low temperature upper mantle model and its associated compositional effects as stated in the previous paragraph is shown in Figure 12. Nearly 1.5 km of elevation remains in central Colorado. Work by Li et al. [2002] have found slow shear wave velocities in the crust of central Colorado and attributed these slow velocities to low density granitic intrusions [*Decker et al.*, 1988]. To

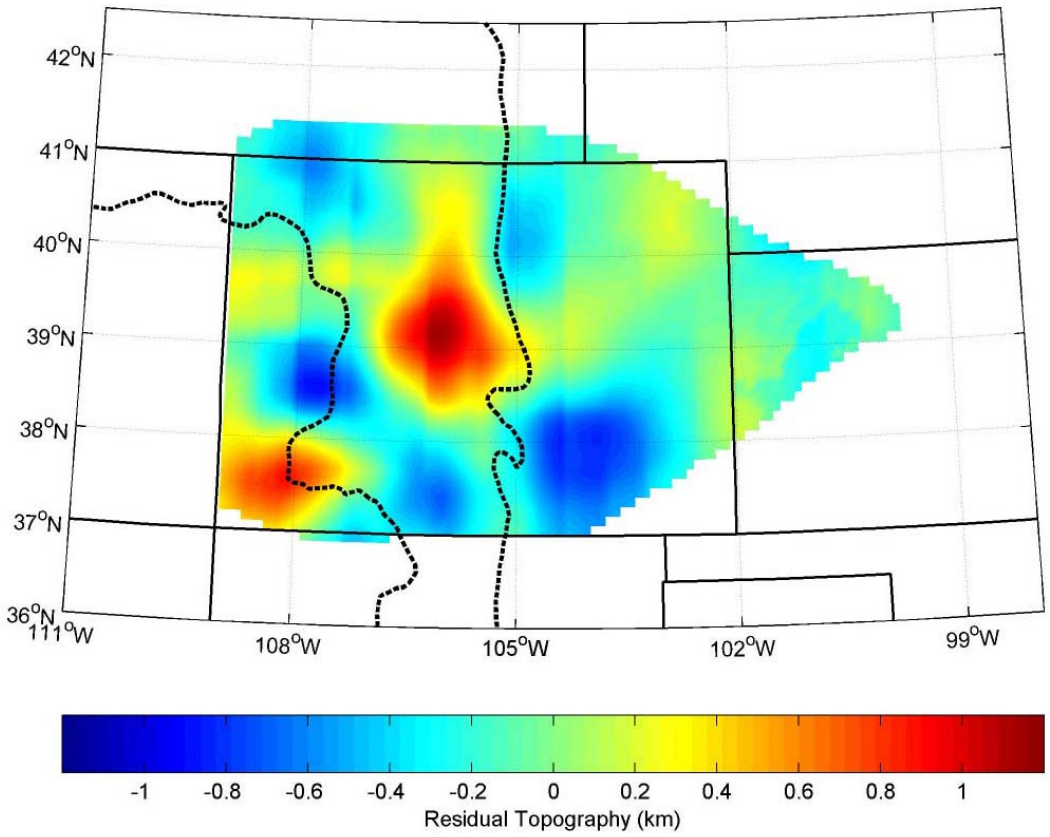

Figure 12. Residual topography after the compensation of thickened crust and upper mantle density contrasts. The remaining uncompensated topography is in the central Colorado Rockies, a position coinciding with low crustal shear velocities and the inferred presence of a large low density granitic intrusion.

account for the residual elevations in central Colorado, the density of this material distributed over the full height of the crust, 45 km, should be reduced by about 3%. Decker et al. suggested 4.5% but distributed the anomaly over 30 km of the upper crust.

Some of the negative elevation residual anomalies coincide with the thickest crust (e.g. southwest Colorado). Li et al. point out that their crustal thickness model would allow a 5 km reduction in crustal thickness to be compensated by a 3% reduction in shear velocity. If limited to the negative anomalies in the southwest

Colorado Rocky Mountains, this effect would reduce the variance of the elevation residual and provide a better correlation between the velocity models of Li et al. [2002] and that of Lee and Grand [1996].

2.6 CONCLUSIONS

Before too much weight is given to any interpretation, we must respect the amount of uncertainty. The primary problem with the results presented above and most field t^* measurements is the significant amount of noise expected for each measurement. Appendix 1 sheds light on some of the possible errors present in the δt^* measurement while Appendix 2 evaluates the effect of some of this error on model resolution. Errors considered for the δt^* measurement include normally distributed random noise and non random noise from basin reflections. Additional errors that are not considered include anisotropy, multipathing, improper ray tracing resulting from not using a three dimensional velocity model and frequency dependent variations in amplitudes across the array resulting from source radiation patterns. In addition to the uncertainty of the observations, the theoretical relationship between shear velocity and attenuation is uncertain. Rock physics experimentation has made progress but has had difficulty making absorption and dispersion measurements under mantle conditions at seismic frequencies with rocks of appropriate composition. Further, the temperature models presented above are relative and knowing the correct phase relationships between mineral assemblages requires knowing the absolute pressure and temperature.

Aside from the uncertainties, several results can be stated. High attenuation underlies the eastern Colorado Rockies and is likely due to elevated temperatures. East of the Rockies, attenuation gradually decreases as velocity gradually increases reflecting at least a simple decrease in temperature. To the west low attenuation coincides with the lowest velocities, and the interpretation is less conclusive. If a frequency limited attenuation band is active, the low velocities and low attenuation may be very hot mantle, over 300 K above its surroundings. If attenuation obeys a more simple relationship to velocity as in equation 14, this anomalous region is due to compositional variation. Our preferred model assumes a linear relationship between velocity and attenuation over the temperatures and frequencies encountered in this study and suggests that the southwest Colorado Rockies are underlain by up to 0.5% partial melt and the substitution of up to 3% olivine with phlogopite.

After the addition of various density anomalies, we find that the Colorado Rocky Mountains are supported by low density mantle, thick crust [*Li et al.*, 2002], and in some cases, low density crust [*Li et al.*, 2002]. The low density mantle may either be thermal and/or compositional in origin. The presence of recent and potassic magmatism above the anomalous region suggests that partial melt and the presence of phlogopite are responsible for at least some of the decrease in velocity and density.

Acknowledgements. We thank Karen Fischer and Steve Grand for thorough reviews that helped to substantially improve this manuscript and Randy Keller for his work as editor. Instruments used in the Rocky Mountain Front study were from the IRIS Passcal instrument pool. This work was supported in part by National Science Foundation grants EAR-9614410 and EAR-0003747.

3. FOUNDERING LITHOSPHERE IMAGED BENEATH THE SOUTHERN SIERRA NEVADA, CALIFORNIA, USA

3.1 ABSTRACT

Seismic tomography reveals garnet-rich crust and mantle lithosphere descending into the upper mantle beneath the southeastern Sierra Nevada. The descending lithosphere consists of two layers: an iron-rich eclogite above a magnesium-rich garnet peridotite. These results place descending eclogite above and east of high P wavespeed material previously imaged beneath the southern Great Valley, suggesting a coherence in the lithospheric removal process previously unsuspected.

3.2 INTRODUCTION

The Sierra Nevada mountain range of California is one of the highest (about 3 km mean elevation) in the United States, however the crust is only 35 km thick [*Wernicke et al.*, 1996] and requires some unusual structure in the mantle. Xenoliths [*Ducea and Saleeby*, 1996] and volcanic rocks [*Manley et al.*, 2000; *Farmer et al.*, 2002] suggest that the upper mantle source for these materials, beneath the Sierra Nevada, changed from an eclogite facies garnet pyroxenite to a garnet-free spinel peridotite about 4 million years ago (Ma). Eclogitic rocks may still be present in the upper mantle below the Sierra Nevada [*Zandt*, 2003] and knowing where and how much is left constrains how lithospheric material is removed and how continental crust grows and changes beneath mountain ranges [*Ducea*, 2002]. To determine whether there are any eclogitic rocks left, we used three dimensional models of P and

S wave speeds to define compositional and thermal characteristics of the lithosphere. We measure attenuation to correct the velocities for anelastic effects which include temperature and hydration. The corrected wave speeds are subsequently termed anharmonic wave speeds and are compared with laboratory predictions.

Low Pn velocities directly beneath the high Sierra [*Jones et al.*, 1994; *Fliedner et al.*, 1996] and high attenuation in the upper mantle in the region [*Al-Khatib and Mitchell*, 1991] are consistent with high temperature, low-density material. SKS splitting measurements [*Polet and Kanamori*, 2002] (Fig. 1) indicate strong seismic anisotropy oriented N80°E beneath the central Sierra, probably due to the presence of strained, olivine-rich, peridotitic mantle. Less splitting beneath the eastern and western Sierra may indicate largely isotropic material, such as eclogite [*Christensen and Mooney*, 1995], little strain, or a vertical fast axis of anisotropy. The region of large SKS splitting and low Pn velocity correlates well with high mantle electrical conductivity that is probably due to 1% partial melt beneath the southern Sierra Nevada [*Ducea and Park*, 2000]. These observations are consistent with the presence of a peridotitic uppermost mantle near asthenospheric temperatures near the Sierran crest today.

3.3 METHOD AND RESULTS

We recorded 40 teleseismic events that yielded 800 seismic wave traces on 24 broadband seismometers (Fig. 1). We measured direct P-wave, S_{fast}, and S_{slow}-wave travel time delays (t_p, t_{sf}, and t_{ss}) and S_{fast} and S_{slow}-wave path integrated attenuation, Δt^* [*Sheehan and Solomon*, 1992], to invert for variations in P-wave speed, v_p, fast

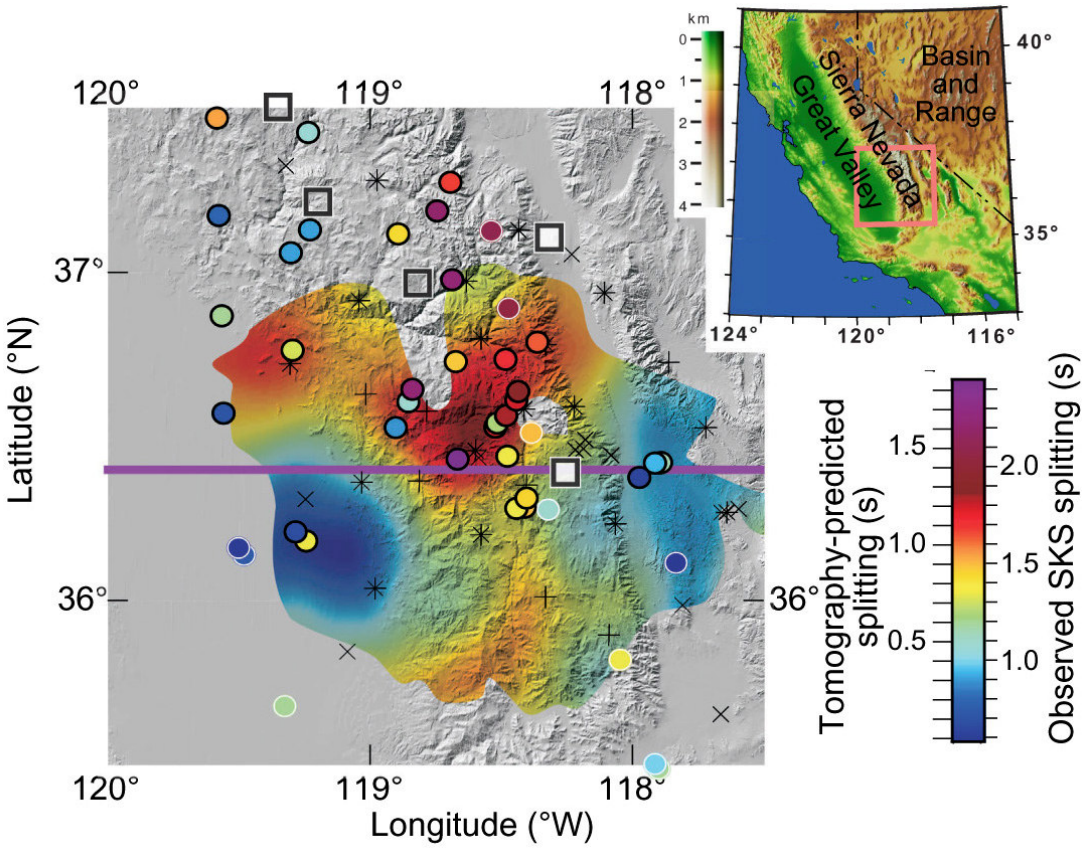

Figure 1. Topographic map of the southern Sierra Nevada overlain with tomographically predicted shear wave splitting (this study) and independently determined SKS splitting measurements, filled circles ([*Polet and Kanamori*, 2002] – white outline, [*Jones and Phinney,* 1999] – black outline). Map of Nevada and California with pink outline of study area given in the upper right for reference. The SKS measurements are placed at 125 km depth along the SKS ray path. The tomographically predicted splitting time is determined by integrating differences between the fast and slow S-wave speed models in the upper 200 km for regions with greater than 150 km thickness of resolution greater than 0.5. Thick purple line crossing at 36.4° N is the latitudinal position of the vertical slices in figure 2. The +'s are seismograph stations used for the tomography, the x's are stations used to measure SKS splitting, and the stars, + overlain by x, are stations used for both tomography and SKS splitting. The open boxes are garnet peridotite and garnet pyroxenite xenolith localities, filled boxes are spinel peridotite xenolith localities.

and slow S-wave speed (v_{sf} and v_{sf}) and fast and slow oriented S-wave attenuation (Q^{-1}_{sf} and Q^{-1}_{ss}). These were combined to examine variations in the ratio of P-wave to S-wave velocity, v_p/v_s, and transverse S-wave anisotropy. Our tomographic inversions

reduce the variance of the data by more than half of that available while measurement noise and station and event statics account for the remainder (Appendix 3).

The tomographic models reveal regions of alternating high and low velocity and attenuation that dip ~55° to the east southeast (Fig. 2). The region of high P-wave velocity at 36.4° N extends from -119.5° W to -118° W and may be what has been referred to as the Isabella anomaly. The volume above this anomaly consists of a slow P and S wave region. The S-wave velocities decrease more across this contrast than do the P-wave velocities, giving rise to an increase in the v_p/v_s ratio. These seismic anomalies trend northeast (Fig. 3c).

Upon vertically integrating the differences in S_{fast} and S_{slow} travel times for the top 200 km, we are able explain more than 50% of the variance of the SKS splitting measurements (Fig. 1, Fig. S1, Appendix 3), an independent verification of our subsurface distribution in anisotropy. Note that the SKS measurements were not used in the inversion; we used only the orientation of fast S wavespeed derived from the splitting analysis. The shallow depth for the origin of the splitting (<200 km) is consistent with the 1 second variation in splitting amplitudes over short distances (<50 km) and inconsistent with splitting distributed over greater depths.

3.4 DISCUSSION

Attenuation is needed to distinguish between the effects on wave speed from thermal and compositional variations [*Boyd and Sheehan*, in Press; *Karato*, 1993]. Anisotropy [*Christensen and Mooney*, 1995] and Poisson's ratio [*Christensen*, 1996] can then be used to constrain the composition (Table 1). Due to anelasticity,

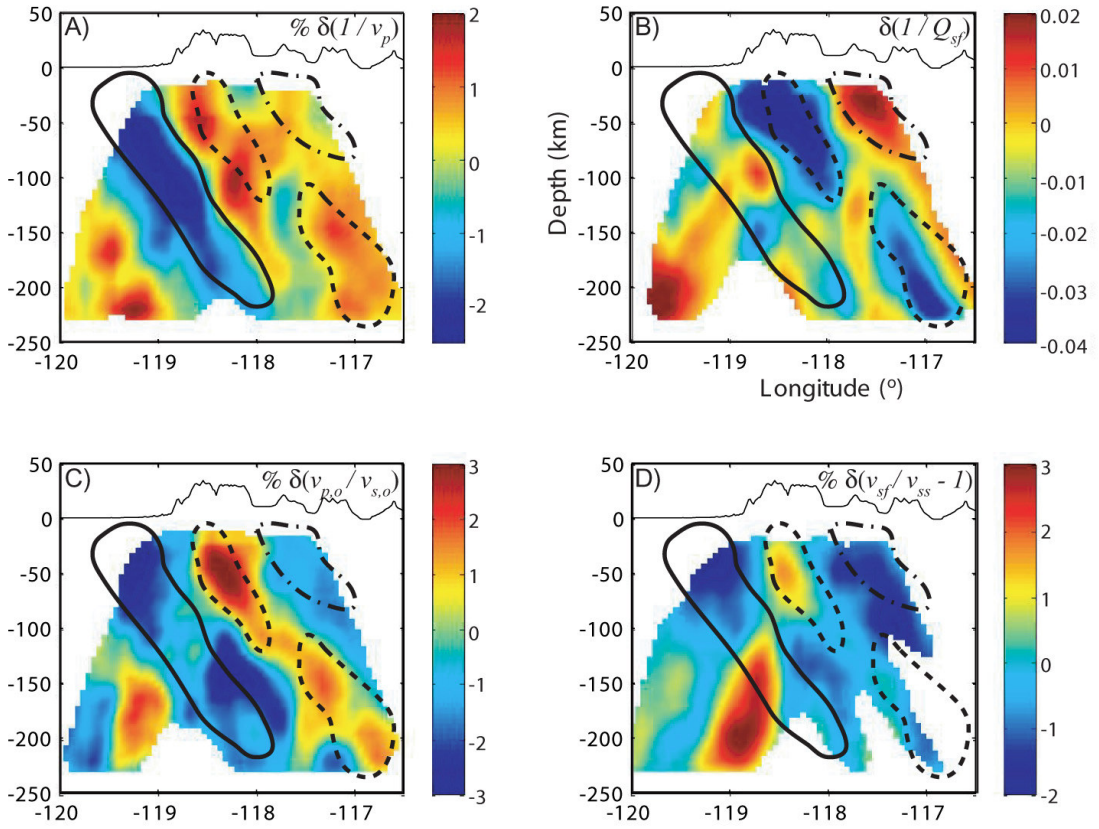

Figure 2. Vertical slices of our tomographic models and derived quantities, percent change in P-wave slowness (**A**), change in attenuation (**B**), percent change in anharmonic v_p/v_s ratio where v_s is taken from the average of the fast and slow models (**C**), and shear wave anisotropy where the slow model is derived as residuals from the fast model (**D**). The solid line indicates the region of descending garnet peridotite and the dashed lines delineate the region of garnet pyroxenite. The region of low velocities and high attenuation above the garnet pyroxenite is presumably the infilling of asthenospheric spinel peridotite (dashed-dot outline). Topography is depicted with 10X vertical exaggeration.

temperature variations will cause seismic velocities and attenuation to vary predictably [*Jackson*, 1993]. We interpret deviations from the thermal relationship as being caused by variations in composition.

Since the dipping layer of low wave speeds is accompanied by low attenuation, temperatures are relatively low (~200 K lower than the material to the east) and partial melt or partially water-saturated minerals are not likely present. This leaves

Table 1. Changes in geophysical properties in the mantle from different causes.

Factor Increasing:	***Change to Observable:***				
	P wavespeed	v_P/v_s *ratio*	*Attenuation*	*Anisotropy*	*Density*
Temperature	decrease	increase	increase	No change	decrease
Melt	decrease	increase	*	?	decrease
Magnesium	increase	decrease	No change	No change	decrease
Garnet/olivine ratio	increase	increase	No change	decrease	increase

*: attenuation will only increase if high temperatures are required to produce melt (*14*).
?: anisotropy may increase or change orientation if melt pockets/bands are favorably oriented.

some sort of compositional effect producing, in addition to low velocities, a high v_P/v_s ratio and variable anisotropy. High v_P/v_s ratios can indicate an increase in the amount of pyroxene and garnet relative to olivine or a decrease in the Mg# [Mg/(Mg+Fe)]. The variable anisotropy is more difficult to interpret. Lower anisotropies can be from an absence of olivine, an absence of strain, or a heterogeneously strained peridotite. In response to infilling asthenosphere, the low anisotropy in the inferred region of spinel peridotite (Fig. 2D) could be anisotropic but have a near vertical axis of orientation. Normally isotropic lithologies like eclogites might be anisotropic if pervasively cut by dikes or if the pyroxenes have become preferentially aligned (Appendix 3). The large anisotropy appearing below the dipping layer of high P-wave velocities may reflect lateral extrusion of asthenospheric peridotite in response to delaminating mantle lithosphere.

Ambiguity in interpreting the tomographic results can be reduced by examining the xenoliths erupted nearby in the central Sierra Nevada. There are three groups of

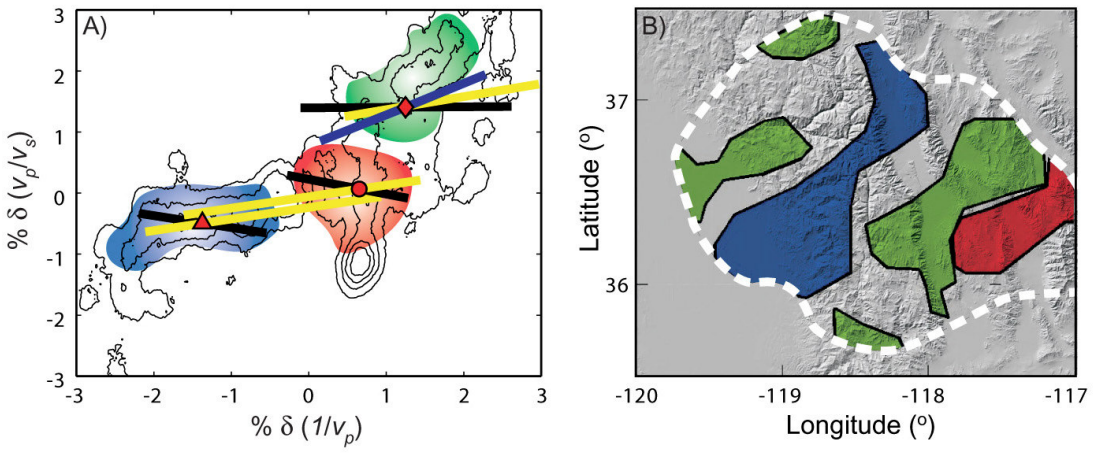

Figure 3. (**A**), Percent change in anharmonic v_p/v_s ratio versus percent change in anharmonic P-wave slowness for a range of model compositions at a pressure of 3 GPa and a range of temperatures. Compositions defined in the text that best match the seismic observations are garnet pyroxenite (red diamond) at 1000° C, spinel peridotite (red circle) at 1200° C, and garnet peridotite (red triangle) at 1000° C. Thick black lines represent range in composition where garnet is substituted for pyroxene. For the garnet pyroxenite, garnet varies from 20% (right end of black line, slower wave speeds) to 40%, the spinel peridotite, 0 to 10%, and the garnet peridotite, 0 to 10%. Yellow lines represent a 400 K variation in temperature (900 to 1300° C), with faster wave speeds (to the left) accompanying lower temperatures. The blue line spans the range of Mg# for the garnet pyroxenite samples. Contours denote anharmonic P-wave slowness and v_p/v_s from our Sierran tomography from 75 to 100 km depth. Each contour interval represents 20% of the data. Colored areas correspond to compositional regions outlined in the tomography of figure 2 and shaded areas in the 100 km depth slice (**B**), garnet pyroxenite (green), spinel peridotite (red), and garnet peridotite (blue). Compositional zones in (B) derived from tomography using composition relations (Appendix 3) with P wave slowness, Poisson's ratio, anisotropy, and attenuation. The white dashed line delimits the part of the tomography model with resolution greater than 0.4.

xenoliths: garnet pyroxenites and garnet peridotites (both erupted before 8 Ma) comprising the old mantle lithosphere [*Ducea and Saleeby*, 1996; *Dodge et al.*, 1988] and fertile, olivine-rich, garnet-free spinel peridotites (erupted since 4 Ma) having an asthenospheric affinity [*Ducea and Saleeby*, 1996]. Chemically, the garnet and pyroxene in the pyroxenites tend to have low Mg# while the olivine in the peridotites

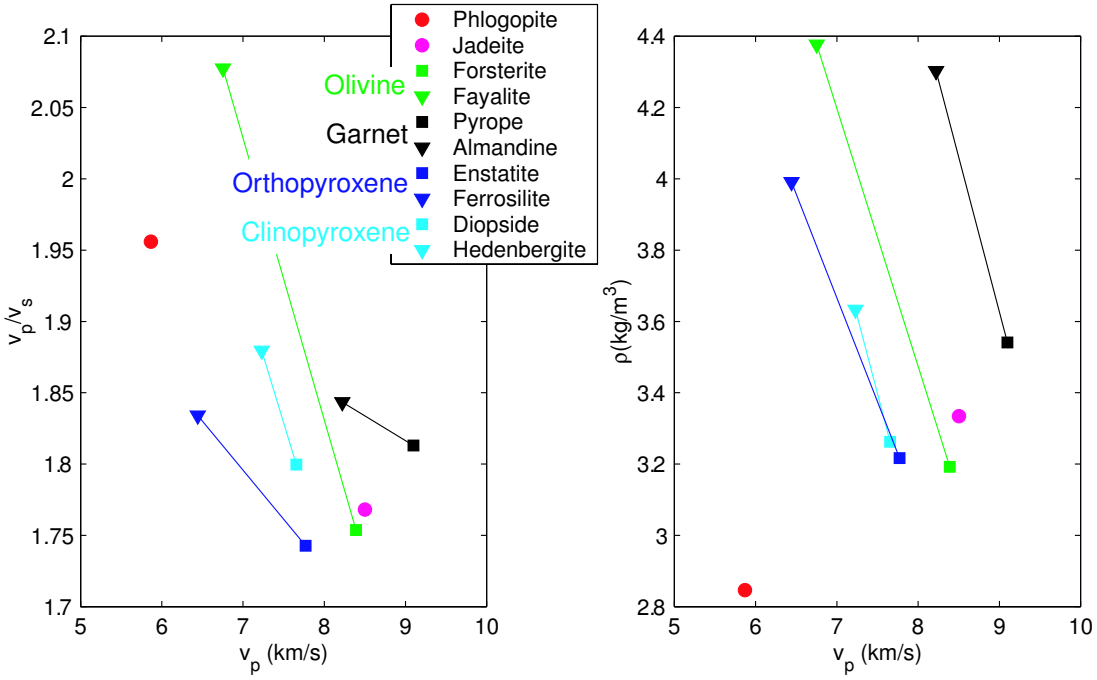

Figure 4. P-wave speed plotted against v_p/v_s ratio (**A**) and density (**B**) for various upper mantle minerals. Triangles are Mg endmembers of solid solution series with the Fe endmembers denoted by squares.

has a higher Mg# [*Ducea and Saleeby*, 1996]. This observation means that the garnet pyroxenite will have higher v_p/v_s ratios relative to the peridotites.

We calculate the P and S wave speeds [*Hacker and Abers*, 2004] (Appendix 3) for a range of expected compositions and compare these values to our observations of anharmonic wave speed (Appendix 3) to broadly determine the mineralogy and Mg# in the observed seismic anomalies (Figure 3). Figure 4 displays the values of P-wave speed, v_p/v_s ratio and density for various minerals. The modal proportions for the garnet pyroxenite xenolith samples are predicted to be about 65% clinopyroxene and 35% garnet [*Saleeby et al.*, 2003]. The Mg# ranges from 0.6 to 0.9 for the clinopyroxenes and 0.3 to 0.6 for the garnet [*Ducea and Saleeby*, 1996]. The composition that best matches our seismic observations averages 70% pyroxene and 30% garnet (Appendix 3). Compositions having as much as 40% garnet would be

acceptable if a Reuss average, as opposed to the Voight-Reuss-Hill average [*Watt et al.*, 1976] used here, is favored. One garnet peridotite sample has 75% olivine, 15% orthopyroxene, 5% clinopyroxene and 5% garnet [*Ducea and Saleeby*, 1998] while the Mg# are reported to be on average 0.91, 0.91, 0.92, and 0.85 for those minerals, respectively [*Ducea and Saleeby*, 1996]. Our seismically determined composition averages 75% olivine, 20% pyroxene and 5% garnet. The young peridotite samples are devoid of garnet and average 80% olivine with the remainder orthopyroxene, clinopyroxene and spinel [*Wilshire et al.*, 1988]. Their Mg# average 0.89, 0.89, 0.87, and 0.67 respectively [*Ducea and Saleeby*, 1996]. Since a majority of the young samples have been classified as harzburgites, we restrict our analysis to clinopyroxene-free assemblages. We find a composition having on average 80% olivine, 16% pyroxene, and 4% garnet.

Many eclogites are seismically fast because they have a large proportion of garnet and much of the pyroxene is in the form of jadeite [*Coleman et al.*, 1965]. The xenoliths found here however, have large amounts of clinopyroxene [*Ducea and Saleeby*, 1998] and very little jadeite [*Ducea and Saleeby*, 1996]. The garnet pyroxenites are therefore slower than common eclogites and have a higher v_p/v_s ratio relative to the peridotites (Fig. 3A). A comparison of the characteristics of the seismic anomalies to calculated values for mineral assemblages (Fig. 3A) reveals that the dipping layer of high velocity is the garnet peridotite, the low velocity layer above, garnet pyroxenite, and the seismically intermediate region above and to the east, asthenospheric spinel peridotite (Fig. 2). A map view of the older garnet-bearing assemblages at 100 km depth indicates a NE strike to this structure (Fig. 3B). The

seismically determined compositions imply that at 100 km depth, densities increase from close to neutrally buoyant garnet peridotite below to very dense, negatively buoyant ($\Delta\rho \approx 185$ kg/m^3), garnet pyroxenite above.

3.5 CONCLUSIONS

Though we have suggested specific differences in composition and temperature for the three rock assemblages identified, the most robust conclusion is that three distinct rock types exist in the upper mantle beneath the Sierra Nevada. This observation is made possible by correcting measured P and S-wave seismic velocities for attenuation and comparing these values to laboratory results. The apparent dip of the two garnet-bearing packages and the asymmetry of the package (garnet peridotite to the west of the garnet pyroxenite) are important constraints on the mechanism of removal of this material. The asymmetry resembles delamination of stratified mantle lithosphere from the crust, and is inconsistent with most numerical models of removal by development of a Rayleigh-Taylor instability [*Houseman and Molnar*, 1997], though such asymmetry might be produced by an initially asymmetric instability [*Jull and Kelemen*, 2001]. The eastward plunge of this body indicates that either material has moved directly downward or somewhat to the east relative to the overlying crust, in contrast to motion to the west relative to the crust inferred from older images of this structure [*Zandt*, 2003]. Imaging one of the very few (if not the only) examples of ongoing removal of mantle lithosphere from beneath continental crust, this tomography provides some of the best observational constraints on the process of removing dense material from continental crust.

Acknowledgements. Thanks to Peter Molnar and Lang Farmer for helpful discussion and Bob Phinney and several land use agencies (Forest Service, Sequoia and Kings canyon National Parks, Bureau of Land Management) for help in obtaining the data. We also acknowledge two anonymous reviewers and Linda Rowan for thorough reviews. This work was supported by NSF grants 9526974 and 0003747 and a CIRES Research Fellowship.

4. ILLUMINATING UPPER MANTLE STRUCTURE BENEATH COOK STRAIT, NEW ZEALAND, WITH RECEIVER FUNCTIONS

4.1 ABSTRACT

Utilizing teleseismic receiver functions derived from broadband seismic arrays on the north end of the South Island and south end of the North Island of New Zealand, we image seismic impedance discontinuities in the upper mantle beneath Cook Strait. Impedance discontinuities imaged include the top of the subducting Pacific Plate and the mineral phase boundaries associated with the mantle transition zone. The subducting slab continues south to the extent of our data. Our data is consistent with seismicity that indicates that the slab dips steeply beneath the northwest region of the study area. We also find a thick mantle transition zone, suggesting that the Pacific Plate has penetrated the transition zone. Lastly, the 410 km P to S conversion has significant energy on the transverse component, evidence of shear wave splitting produced by anisotropy. This observation can be explained by shear wave anisotropy above the transition zone having a fast axis oriented between N1E and N46E.

4.2 INTRODUCTION

The islands of New Zealand represent a unique confluence of two plates generating opposing subduction zones separated by an oblique transform boundary (Figure 1) [*Cande and Stock*, 2004]. The Pacific Plate subducts beneath the Australian Plate on the North Island and uppermost South Island while the Australian

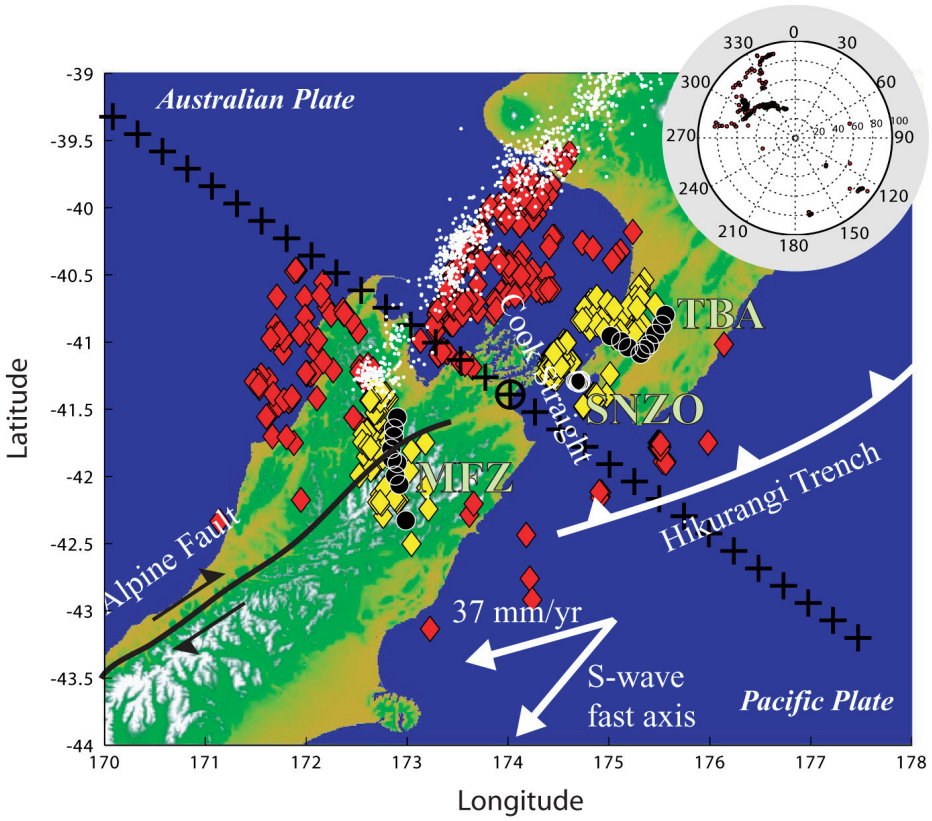

Figure 1. Map of New Zealand with locations of the Tararua Broadband Array (TBA), SNZO, and Marlborough Seismic Study (MFZ) (black circles). The North and South Islands are separated by the Cook Strait. The Pacific Plate moves SW relative to the Australian Plate at 37 mm/yr and subducts beneath the North Island at the Hikurangi Trench. The dextral Alpine fault separates the two plates along much of the South Island. The black crosses are grid points used for the deeper CCP stack (Figure 5) and are separated by 25 km. The cross with the circle is the center of the grid corresponding to Y = 0. The red (yellow) diamonds are piercing points of seismic rays at 400 (100) km depth for our data set. The white dots are earthquakes from greater than 150 km depth and give some idea of the northwestern extent of the subducting plate. The polar figure in the upper right shows the distribution of azimuths and distances for the events in this study.

Plate subducts beneath the far southern portion of the South Island. The Southern Alps on the South Island bridges the two subduction zones and is an oblique dextral strike slip fault separating the Pacific and Australian plates. The islands are marked with various natural hazards due to this complex plate boundary from volcanic on the North Island to seismic throughout.

Patterns of seismicity in the northern subduction zone suggest a strongly bending plate which approaches a near vertical orientation at 200 km depth [*Anderson and Webb*, 1994]. Focal mechanisms indicate compression and thrust faulting in the overlying crust resulting from strong coupling between the two plates and tension in the subducting plate beneath about 50 km depth [*Reyners et al.*, 1997]. Deeper seismicity, >100 km depth, ends abruptly beneath the Nelson region, which may mean a termination of the subducting plate. However, focal mechanisms do not change at this location and so some argue that the subducting plate continues to the southwest, albeit without sufficient stress to cause seismicity [*Reyners and Robertson*, 2004]. In the transform region of the South Island, the shallower seismicity at 30 to 100 km depth is suggested to be due to high shear strain and depressed geotherms [*Kohler and Eberhart-Phillips*, 2003].

Many seismic velocity investigations have been carried out to learn about the seismic structure of New Zealand. Tomographically, a high P-wave velocity body dipping to the northwest north of the Fiordlands has been imaged using teleseismic P-wave residuals [*Kohler and Eberhart-Phillips*, 2002]. It has been corroborated by fast P-wave travel time anomalies across the midsection of the southern Alps [*Stern et al.*, 2000]. Though the tomography is of relatively low resolution and Stern et al. [2000] suggest the fast P-wave speeds in the midsection of the southern island is not due to subduction but rather to lithospheric thickening, it is possible subduction continues through the Southern Alps.

More detailed investigations have been performed to elucidate the finer structure of the crust and uppermost mantle. In an attempt to explain *ScSp* precursors,

Bourne and Stuart [2000] inferred the presence of a low velocity layer at the top of the subducting slab which they believe to be subducted sediments. This covers a thick oceanic crust which increases in thickness across the Cook Strait from 10 to 15 km [*Bourne and Stuart*, 2000; *Eberhart-Phillips and Reyners*, 1997].

From previous studies, it is evident that the southern extent of Pacific Plate subduction beneath New Zealand is not known. Our receiver function study sheds some light on this problem through observations of slab seismic discontinuities as well as transition zone topography. As a byproduct, we are also able to help substantiate various observations in the Cook Strait region from the seismic structure of the slab to upper mantle anisotropy.

4.3 METHOD

This study combines the data from several broadband seismic arrays on either side of Cook Strait, New Zealand (Figure 1). On the North Island, the Tararua Broadband Array (TBA) acquired data from February of 1991 to July of 1992 and consists of 9 broadband seismometers [*Stuart et al.*, 1995]. The broadband Incorporated Research Institutions for Seismology (IRIS) station SNZO has been continuously recording since March of 1992 and was supplemented with 4 additional broadband seismometers during most of 1998 [*Stewart*, 1998]. The Marlborough seismic study (MFZ) on the South Island was active from October 2000 to May 2002 and utilized 9 broadband seismometers in addition to 45 short period seismometers [*Wilson et al.*, 2001; *Wilson et al.*, 2004]. Many local and teleseismic events have been recorded with these arrays. For our receiver function study, over 100

earthquakes between 30 and 90 degrees epicentral distance with a body wave magnitude ≥ 5 were utilized, yielding 275 broadband traces from which to make and interpret receiver functions. The distribution of backazimuths is limited (Figure 1). Most hail from the northwest. There are several from the southeast, and very few come from the northeast and southwest.

The receiver function technique is relatively straight forward. A receiver function is basically a time series consisting of bumps which represent the subsurface S-wave impedance contrasts. A P-wave that impinges from below and encounters a seismic impedance contrast will generate reflected and refracted P and S-waves. For horizontal interfaces, these refracted S-waves will appear primarily on the radial component of motion. We can then deconvolve the vertical component from the radial to obtain a series of bumps corresponding to the P-wave impedance contrasts. The resulting time series is a radial receiver function [*Langston*, 1977]. The vertical can also be deconvolved from the transverse component of motion which is then a transverse receiver function. Arrivals on the transverse receiver function can be indicative of dipping interfaces or seismic anisotropy. Unfortunately, free surface multiples, also referred to as reverberations, also appear in and contaminate the receiver functions (Figure 2).

Deconvolution can be performed in the frequency domain with a water level [*Dueker and Sheehan*, 1998] or in the time domain [*Ligorria and Ammon*, 1999]. In addition to these traditional techniques, we attempted a modification to the spiking deconvolution. In spiking deconvolution, the receiver function is produced by cross-correlating the vertical with the radial. We modified this by deconvolving the

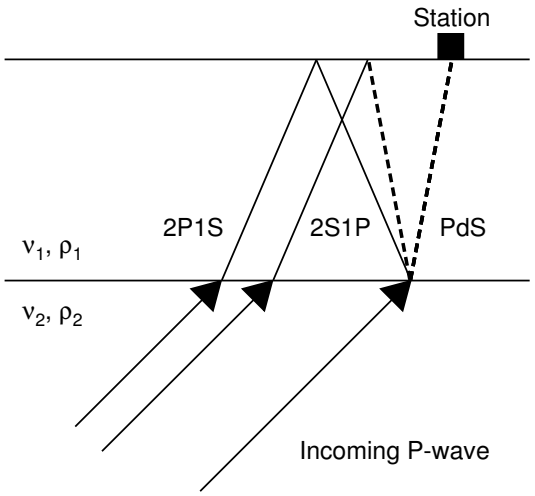

Figure 2. Schematic representation of how a receiver function is produced by subsurface impedance contrasts. Solid (dashed) lines are P (S)-waves. The incoming P-wave will generate reflected and refracted P and S-waves. The refracted S-wave, P_dS, is of primary interest while the refracted P-wave will generate free surface multiples 2S1P and 2P1S.

autocorrelation sequence of the vertical from the vertical-radial cross-correlation sequence. In comparing the frequency domain, iterative time domain [*Ligorria and Ammon*, 1999], and modified spiking deconvolutions with synthetic traces having various amounts of normally distributed random noise, we found that the modified spiking deconvolution best recovered the amplitudes. However, when evaluating ray parameter plots, the iterative time domain deconvolution looked most coherent.

We therefore employ the iterative time domain deconvolution in which the vertical component of the broadband seismometer is iteratively correlated and subtracted from the radial revealing various types of multiples as well as P to S conversions off of subsurface seismic discontinuities. The P to S conversions, PdS where d represents the subsurface position of a P-wave impedance contrast, are of primary interest. The resulting receiver functions are filtered by convolution with a Gaussian wavelet to remove high and very low frequency noise. For shallow

discontinuity structure, the Gaussian wavelet a peak period of 3 seconds and for deeper structure, 10 seconds.

The subsurface images of seismic discontinuities result from common conversion point (CCP) stacking of the receiver functions [*Dueker and Sheehan*, 1998]. The CCP stacking technique is analogous to the common midpoint (CMP) or common depth point (CDP) techniques used in reflection seismology. Stacking of receiver functions enhances coherent PdS conversions while decreasing random noise and reducing the amplitudes of free surface multiples. Seismic rays are traced from the station towards the event using a one dimensional velocity model and the receiver function is stretched along this ray path, corrected from time to distance using a modified one dimensional velocity model. A two dimensional grid of subsurface bins is then defined (Figure 1) where the receiver function amplitudes for all traces (receiver functions) that pierce a given subsurface bin are averaged. The horizontal grid spacing for shallow discontinuities is 10 km with 3 horizontally adjacent bins being averaged. For deeper discontinuities, the horizontal grid spacing is 25 km with 5 horizontally adjacent bins being averaged.

Before interpreting a subsurface CCP stack, it is helpful to view ray parameter plots which can help identify subsurface seismic conversions and various multiples (Figure 3). This may prevent misinterpretation of signals appearing in the stack that are multiples rather than direct P to S conversions. In a ray parameter plot, also called a moveout plot, PdS conversions have a prograde moveout, i.e. with increasing ray parameter, PdS conversions come in later. Free surface multiples however, have a retrograde moveout, i.e. with increasing ray parameter the multiples come in sooner.

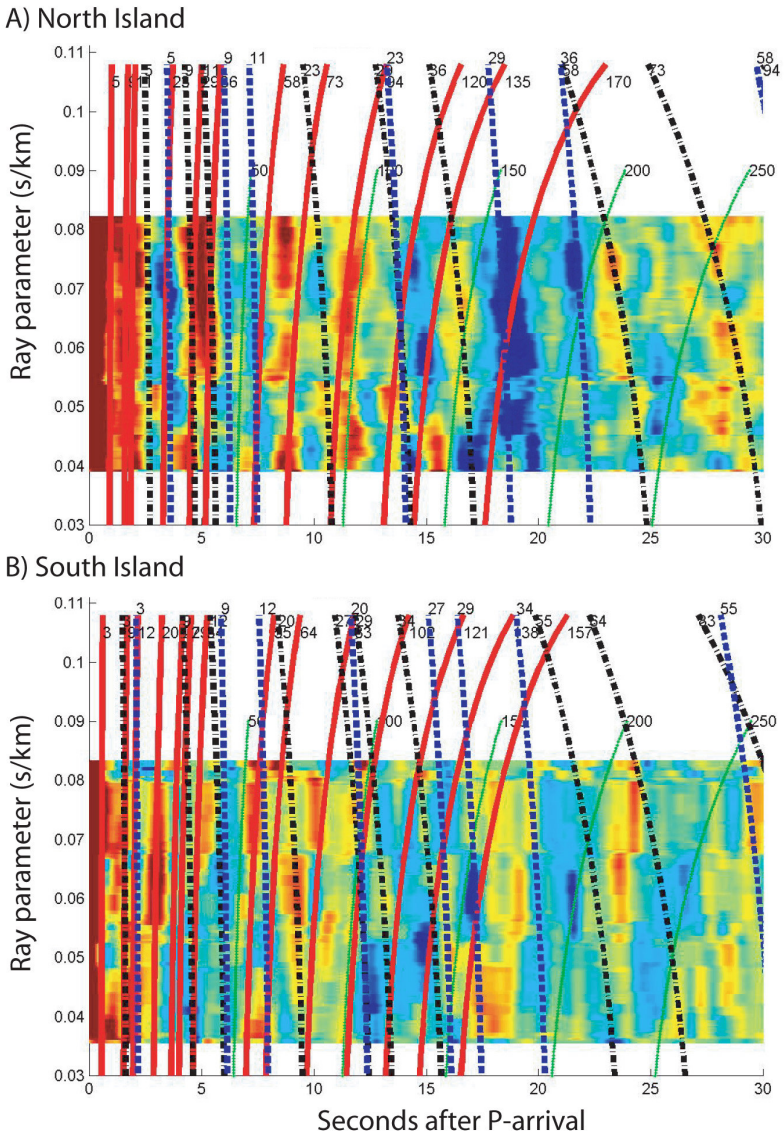

Figure 3. Radial receiver function ray parameter (moveout) plots for the North (A) and South (B) Island. 197 receiver functions were used in (A) and 78 in (B). All backazimuths are present, with most events coming from the NW. Receiver function red/blue color scale corresponds to receiver function amplitude relative to direct P on the radial receiver functions, with red being positive amplitude (positive impedance contrast) and blue being negative amplitude (negative impedance contrast). Predicted timing of primary P to S (P_dS) conversions are given by red lines (green for reference depths) assuming horizontal interfaces and applying a modified one dimensional velocity model of Bourne and Stuart [2000], 2P1S reverberations – black dashed lines, and 2S1P reverberations – blue dashed lines. Impedance contrasts increasing with depth produce a positive PdS, positive 2P1S and negative 2S1P while impedance contrasts decreasing with depth produce negative PdS, negative 2P1S and positive 2S1P. The numbers correspond to the depths at which the interfaces occur.

4.4 RESULTS

Many possible seismic discontinuities have been identified in the ray parameter plots (Figure 3). These plots are produced using all of the receiver functions. They are organized and binned according to ray parameter. Neighboring bins are averaged which helps to suppress random noise. We begin on the North Island because its data tends to be less noisy and then continue to the south using the discontinuities found in the north as a guide. The same discontinuities are generally found on both islands though their precise subsurface position is variable. We find a positive velocity gradient near 10 km depth evidenced by a positive prograde arrival (PdS) near 2 seconds and positive (2P1S) and negative (2S1P) retrograde arrivals at 5 and 7 seconds respectively. This is followed by a strong negative velocity gradient near 20 km depth supported by a negative prograde arrival (PdS) near 4 seconds and negative (2P1S) and positive (2S1P) retrograde arrivals at 10 and 14 seconds respectively. Continuing in this fashion by identifying prograde PdS conversions and retrograde 2P1S and 2S1P multiples with the appropriate sign, we identify the remaining subsurface seismic discontinuities. A positive velocity gradient is inferred near 30 km depth and may be slightly shallower on the South Island. It is likely to be the Moho though it may also be the top of the slab. The velocity continues to increase with another possible positive gradient near 70 and 90 km depth. Velocities then decrease near 130 and 170 km depth, the deeper position possibly marking the bottom of the Pacific mantle lithosphere. Discontinuities at 410 and 660 km are not observed in our ray parameter plots with the exception of a possible 410 in the North Island data.

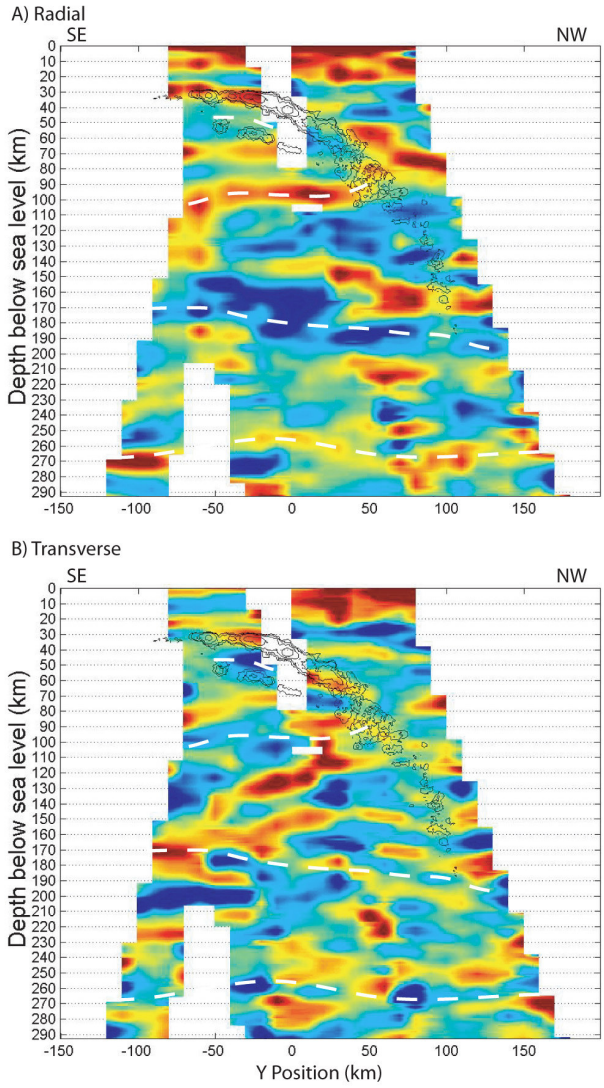

Figure 4. Common conversion point (CCP) stack of North and South Island receiver functions for the radial (A) and transverse (B) components of motion. Amplitudes have been normalized to improve stacking. Contours of seismicity [*GeoNet*, 2004] are overlain on the receiver functions. The center of the grid is located at 174.03, -41.40 (circled cross on Figure 1). Numbers on the y-axis increase to the northwest. Dashed white lines are interpreted velocity discontinuities and discussed in the text.

In accounting for this distribution of seismic discontinuities, we can better interpret the CCP stack representing subsurface seismic discontinuities (Figure 4). In figure 4, as a reference for the expected position of the subducting slab, seismicity within 50km of the grid from 2000 through 2003 is contoured [*GeoNet*, 2004]. We

see that the 10 km discontinuity is continuous to the northwest while the negative just below dips slightly to the southeast. The positive near 30 km depth increases in dip to the northwest approaching a maximum dip above the location of the slab inferred from seismicity. The deeper and presumably intraslab discontinuities at 73 and 94 km depth are more horizontal than the 30 km discontinuity. The '94' km discontinuity moves from 100 km depth to 90 km depth to the NW as it approaches the 30 km northwest dipping interface. Strong negative amplitudes are observed at about 170 km depth, some of which is likely due to strong negative retrograde 2S1P arrivals from the 29 km depth discontinuity observed in the moveout plots. There is however, based on the moveout plots and a negative prograde arrival, a hint of a negative discontinuity near 170 km.

Energy on the transverse receiver function CCP stack (Figure 4b) does not correlate well with the radial receiver function CCP stack. Yet because there is significant and coherent energy on the transverse receiver function CCP stack, seismic anisotropy and/or dipping interfaces are likely to be present [*Savage et al.*, 2004].

Since the South Island tends to have much lower signal to noise ratio due partly to the relatively short period of time over which the array was deployed, we must be sure that observed discontinuities are not a result of noise. To help verify certain discontinuities, we compare the North and South Island data sets individually to see if discontinuities are continuous across and between the data sets (Figure 5). For example, we find that the 94 km discontinuity spans the same subsurface position in both datasets. In contrast, the arrival at 73 km is seen in the North Island but not in

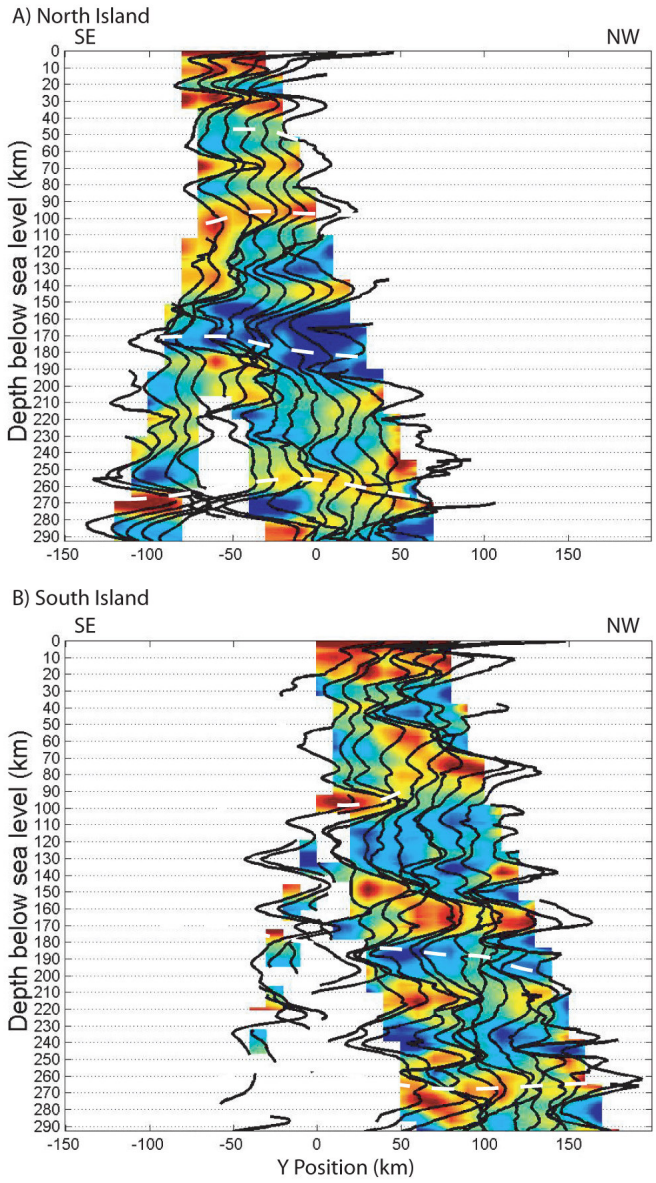

Figure 5. Radial CCP stacks individually for the North (A) and South (B) Island arrays. In regions of overlap we are able to verify arrivals such as the 94 km and 170 km discontinuities which appear at the same depth in both sections.

the south which may indicate reverberations from shallow structure or intraslab discontinuities not present beneath the South Island. The negative polarity arrival at 130 km depth is continuous across the datasets while the negative polarity arrival at 170 km depth is strong beneath the North Island and weak in the South Island.

Several deeper discontinuities appear in the CCP stacks with the aid of additional low pass filtering, lateral smoothing and modest amplification (Figure 6). These include upper mantle discontinuities at 250 and 325 km depth and the transition zone discontinuities at 410, 500, and 660 km depth. The 410 and 660 km discontinuities move apart by nearly 50 km in the northwest section of the CCP stack, consistent with the effect predicted by the temperatures associated with a subducting slab. Significant energy is observed on the transverse component of the P to S conversion for the 410 and 660 km discontinuities ($P_{410}S$, $P_{660}S$), suggesting the presence of anisotropy somewhere above the discontinuity.

4.5 DISCUSSION

A reasonable question to ask is whether the observed interface at 30 km depth in the SE section of figure 4a, which increases in dip to the NW, is in fact the top of the slab. We have investigated this question by synthesizing receiver functions using 2nd order finite difference simulations [*Kelly et al.*, 1976] (Figure 7). The model is composed of a constant velocity contrast in the shape of the expected subducting slab superimposed upon a uniform media. The upper surface is dictated by seismicity [*Anderson and Webb*, 1994] and the lower is based on the expected thickness of the lithosphere using equations for a cooling oceanic plate and the age of the subducting lithosphere. Though, in the real world, a sharp velocity contrast is likely present at the top of the slab, a sharp contrast at the bottom is not expected. The lithospheric age is approximately 120 Ma near the Hikurangi trench [*Muller et al.*, 1997] and is only slightly older (0.5 Ma) in the upper mantle beneath New Zealand because of the fast

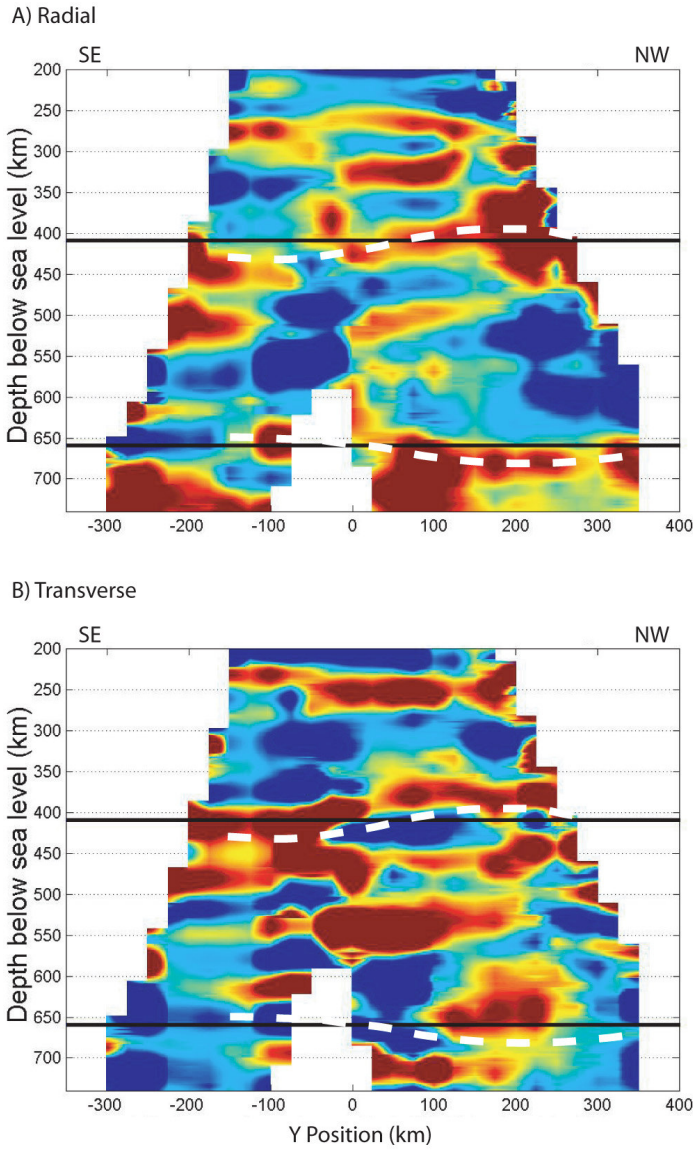

Figure 6. CCP stacks for transition zone discontinuity structure. (A) Radial and (B) transverse. 410 and 660 km depths are indicated by the horizontal black lines while the inferred positions of these discontinuities are indicated by dashed white lines. Stacks utilize data from both North and South Island arrays.

rate of subduction. Applying the equations for a half space model [*Turcotte and Oxburgh*, 1967], the thickness of the lithosphere is predicted to be 140 km. However, for oceanic lithosphere older than about 70 Ma, it seems to reach thermal equilibrium and its thickness becomes relatively constant at about 110 km [*McKenzie*, 1967]. For

the synthetic model, I have chosen a value of 130 km. The synthetic seismograms are generated using the same distribution of ray paths as for the real North and South Island data sets, though the ray paths for the synthetics are projected into the plane of the slab. The same distribution of rays paths are used to more closely simulate the real data going into the CCP profile.

There are several interesting consequences of this simple model slab geometry. Receiver functions from the top and bottom of the slab in the synthetic CCP stack increase in dip and eventually diverge from the expected position of the slab. This happens because of non-migrated stacking. Since receiver functions are traced back along the Ps-wave ray paths produced from 1D velocity models, arrivals from dipping interfaces will not be placed in their proper subsurface position. We have elected not to migrate our data because of the limited backazimuthal coverage. The increase in dip and eventual divergence from the expected position of the top of the slab is precisely what we see in our stack sections made with real data. Another event that could be misinterpreted without the careful forward modeling tests that we perform here results from a diffracted P-wave. It is observed near 20 km depth and appears to be limited to offsets of $Y > 0$ (to the NW). The precise position of this arrival depends on the subsurface P and S wavespeeds and the subsurface position of the slab. This diffracted P-wave may explain the 20 km depth arrival seen in the South Island data set (Figure 5b). An artifact produced from the model geometry is an arrival that appears to be from 80 km depth, while there is no 80 km velocity discontinuity in the input model. The arrival is in fact a 2P1S reverberation from the top of the slab. This arrival seen in the synthetic receiver function CCP stack matches well with the arrival

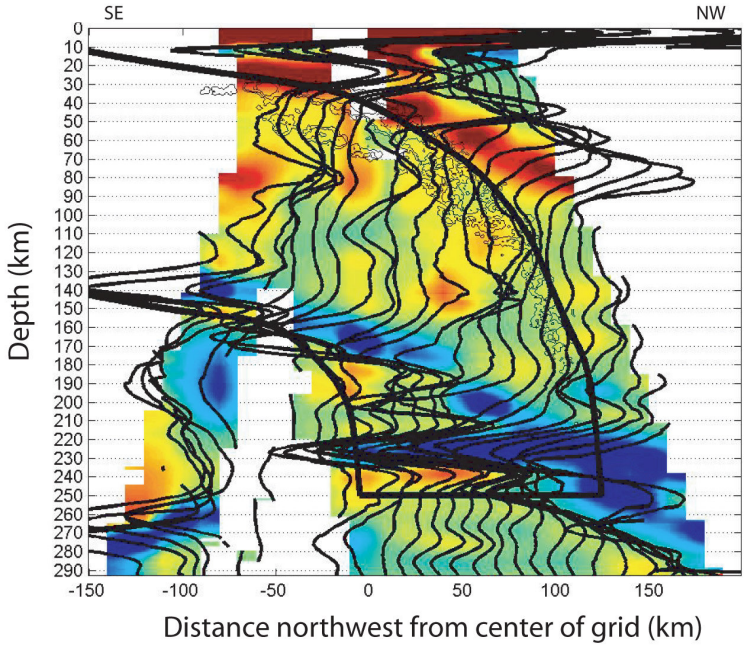

Figure 7. Synthetic radial CCP stack using the geometry of the North and South Island data sets. The thick black line delineates the synthetic slab which has a positive velocity contrast relative to a uniform velocity/density background. Contour of seismicity overlain for reference.

seen for the North Island data at an apparent depth of 73 km, implying that this event may very well be the 2P1S from the top of the slab at 30 km depth. In contrast, ray parameter plots (Figure 3) suggest that 2P1S from a 30 km depth discontinuity would not interfere until a depth of 120 km. This discrepancy may be due to the fact that the ray parameter plots were constructed assuming horizontal interfaces whereas the imaged structure is dipping. Another possibility is that the velocities used to construct the curves in the ray parameter plots for the upper 30 km are too slow.

The 96 km apparent intraslab discontinuity proves difficult to interpret. It does not appear to be related to anisotropy because of an absence of corresponding energy on the transverse. A mineral phase change such as spinel to garnet, the Hales (H) discontinuity [*Hales*, 1969], would occur closer to 60 km depth but was not observed

for *ScS* paths between Tonga-Fiji and SNZO [*Revenaugh and Jordan*, 1991]. The Gutenberg (G) discontinuity [*Gutenburg*, 1948] marking the top of the low velocity zone, on the other hand, was observed by Revenaugh and Jordan [1991] at a depth of 88 km but has a negative impedance contrast thereby producing a negative P_dS, compared to the positive P_dS that we have observed.

Though limited to the relatively thin mafic crust, the only phase change that would produce a significant positive seismic impedance contrast at about 90 km depth would be the production of anhydrous eclogite [*Hacker et al.*, 2003]. If the arrival that we have observed at 96 km is due to the basalt to anhydrous eclogite phase change, we are then observing a diffraction hyperbola from the tip of the resulting seismic discontinuity, one that appears restricted to the southeast – an unlikely scenario. An alternative explanation results from the seismic structure of the slab. Many investigators have found two seismic discontinuities at the top of the slab and have suggested that these represent the top and bottom of the oceanic crust [*Bourne and Stuart*, 2000]. Based upon *ScSp* precursors, this layer is believed to be about 14 km thick [*Bourne and Stuart*, 2000]. The phase 2P1S off of the bottom of this layer at ~45 km depth could easily produce the discontinuity at an apparent depth of 96 km.

A strong negative arrival at 170 km depth is observed in the receiver function CCP stack and is reproduced in the synthetic model. In the synthetic model the 170 km depth arrival is produced from the bottom of the oceanic lithosphere. We initially thought that in the real CCP stack this might be due to a 2S1P phase from the top of the slab, yet this phase does not appear in the synthetic CCP stack. It is therefore possible that the 170 km arrival represents a seismic discontinuity rather than a

reverberation and may in fact be the bottom of the oceanic lithosphere. This would correspond to the G discontinuity, which has been observed globally between 50 and 150 km depth [*Gutenberg*, 1948; *Revenaugh and Jordan*, 1991]. Revenaugh and Jordan [1991] found a very strong negative shear wave impedance contrast across this boundary for *ScS* paths from Tonga-Fiji to SNZO. The deeper position of the G discontinuity observed in our profile may reflect depressed geotherms resulting from subduction. We observe that this boundary has less dip than the upper slab surface and fades to the northwest. This may be due to warming and thinning of the mechanically stronger portion of the oceanic plate and widening of the velocity discontinuity as the slab steepens and penetrates warmer upper mantle. This effect is not incorporated in the synthetic model.

The transition zone discontinuities appear consistent with penetration of a relatively cold subducting slab, e.g. a thickened transition zone [*Gilbert et al.*, 2001; *Flanagan and Shearer*, 1998a; 1998b; *Gu et al.*, 2003]. Decreasing the temperature of olivine moves the $\alpha \rightarrow \beta$ phase transition (410 km depth) to lower pressures or shallower depths. Decreasing the temperature at the γ-spinel$\rightarrow$perovskite and magnesiowustite phase transition (660 km depth) has the opposite effect. The boundary moves to higher pressure or greater depths. Evaluated separately, the deflection of the 410 implies a drop in temperature of (10 km * 38 MPa/ km / 2.9 MPa/K) 130 K while that of the 660 implies a drop in temperature of (-20 km * 40 MPa/km / -2.0 MPa/K) 400 K [*Bina and Helffrich*, 1994].

Temperature perturbations within and around a subducting slab are likely to become smaller with depth [*Stein and Stein*, 1996], especially if the slab becomes

horizontal after hitting the bottom of the transition zone, and are therefore not entirely consistent with our observations of transition zone topography. Models of the thermal structure of subduction zones indicate temperatures could be depressed within the subducting slab by as much as 500 to 1000° relative to the surrounding mantle [*Stein and Stein*, 1996; *Keken et al.*, 2002] implying a 410 km discontinuity elevated by 40 to 80 km. This is not observed near the projected 410 km position of the slab based on seismicity. If the slab were deflected to the northwest by 80 km at 410 km depth, the arrival near 350 km depth would be consistent with the expected thermal anomaly. Still, greater topography on the 660 km discontinuity relative to the 410 km discontinuity is usually observed [*Flanagan and Shearer*, 1998a; *Gu et al.*, 2003; *Bina and Helffrich*, 1994]. In many cases, this is explained by poor resolution of large topographic gradients on the 410 km discontinuity [*Flanagan and Shearer*, 1998a; *Bina and Helffrich*, 1994].

In producing our CCP stacks, we have employed a one dimensional velocity model, clearly an approximation to this complicated structure. Other authors routinely correct for lateral velocity heterogeneities [*Dueker and Sheehan*, 1998; *Gilbert et al.*, 2001; *Flanagan and Shearer*, 1998a], but we have not because an adequate velocity model is not available. If we account for expectations of lateral velocity anomalies, our predicament worsens. All other variables aside, decreasing the temperature of the transition zone due to the presence of the slab should increase its seismic velocity. Accounting for this change in velocity in the CCP stack would not affect the position of the 410 km discontinuity but would move the 660 km to greater depths, further increasing our need for greater temperature contrasts between 410 km depth and 660

km depth. If we increase the velocity above the 410 along the cold fast slab (though in reality this effect might be offset by slower velocities in the mantle wedge) both the 410 and 660 would deepen and the problem persists. To reduce the topography on the 660, we would have to decrease the velocity in the transition zone. This can be accomplished by hydrating the transition zone phases of olivine [*Smyth and Frost*, 2002]. Hydration has the effects of broadening and slowing the transition zone which would serve to reduce the temperature perturbations required at the 410 and 660 to explain the topography. Yet increased transition zone thickness is generally accompanied by faster seismic velocities [*Gilbert et al.*, 2001; *Flanagan and Shearer*, 1998a]. Besides, the observed deflection of the 410 is too small for the expected thermal anomaly. An explanation may be, rather counter intuitively, that there is relative dehydration of the upper transition zone in the region of the subducting slab. Alternatively, reduced temperatures in the slab could inhibit the olivine phase change [*Rubie and Ross*, 1994].

If in fact the temperature contrast at the 660 is significantly greater than at the 410, then the 660 temperature contrast may not be directly related to temperatures in the slab but temperatures in the lower mantle. In this case, some of the deflection of the 660 could represent the top of a convective downwelling in the lower mantle.

Transition zone thickening seems to be a good indicator for the penetration of a cold slab. When our observations are restricted to the South Island stations, we again see a thickened transition zone and conclude that at the latitude of the South Island stations, the Pacific Plate has entered the transition zone. Unfortunately, a single trace comes from the southwest, and because of our poor signal to noise ratio, conclusions

about the depth and southern extent of the slab based on this single trace are uncertain.

In addition to the inferred presence of a slab at the southern extent of our stations, the splitting of the $P_{410}S$ phase as evidenced in the offset between the radial and transverse receiver functions (Figure 6) is a good indication of anisotropy above the transition zone. Traditionally, the orientation of anisotropy would be derived from the dependence of radial and transverse amplitudes on backazimuth. Unfortunately, our backazimuthal coverage is exceptionally limited. Nearly all of our backazimuths are from the northwest. We are therefore left to use alternate means to derive the orientation of anisotropy.

We may initially suggest that the fast direction is probably close to being parallel to the strike of the slab since the transverse arrival leads the radial and most of our backazimuth coverage is from the northwest. To be more specific, after accounting for the multiple normalizations and the damping from filtering, the ratio of the positive amplitude on the radial to that of the positive fast on the transverse is of similar magnitude. From Figure 8, this means that our backazimuths are coming in on average close to 45° degrees counterclockwise from the fast axis. Our average backazimuth is 316° which results in an azimuth of the fast axis of anisotropy of about N1E. The fast axis is probably clockwise from N1E based on the observation that the peak of the radial occurs after the inflection between positive and negative transverse arrivals, e.g. the slow arrival on the radial has greater amplitude then the fast. Further, the clockwise rotation of the fast axis is certainly less than N46E, at which point, no transverse amplitudes would be observed. The range in direction of

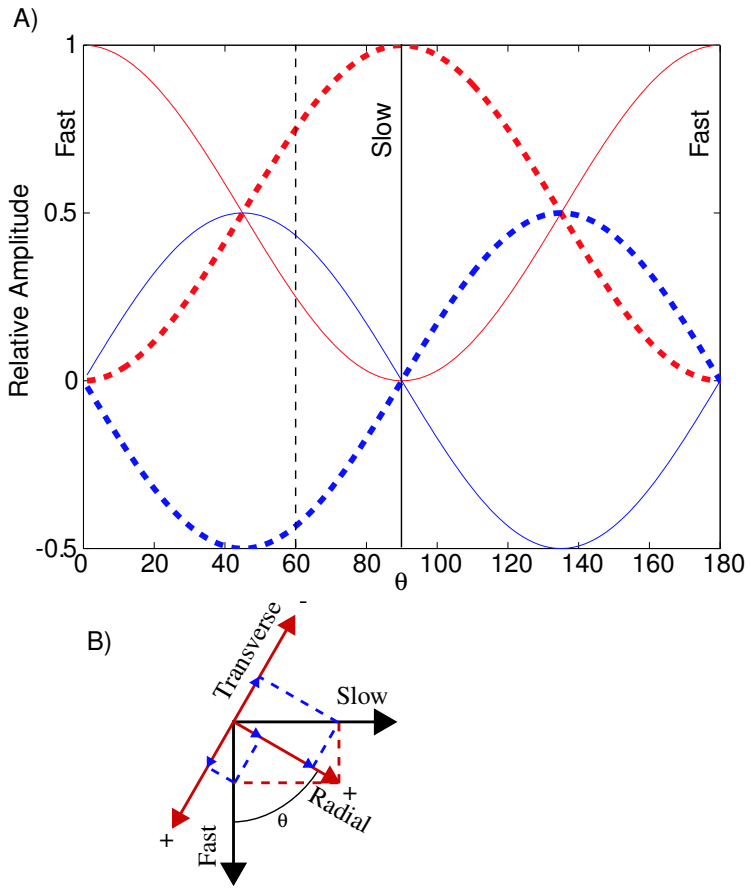

Figure 8. (A) Relative amplitude of fast (solid) and slow (dashed) arrivals on the radial (red) and transverse (blue) components in dependence on the angle between the radial and fast directions. (B) Schematic of orientations of radial and transverse directions relative to the fast and slow directions and an indication of how initial polarizations are mapped into surface radial and transverse motions. The anisotropy we observe is close to the vertical black dashed line, 60 degrees counterclockwise from the fast direction.

the fast axis we have suggested, N1E to N46E encompasses the strike of the slab at this latitude (N35E) and anisotropy inferred from SKS splitting [*Molnar et al.*, 1999]. This orientation is expected for the strain of the upper mantle associated with the relative motion of the Australian and Pacific plates [*Molnar et al.*, 1999; *Marson-Pidgeon and Savage*, 2004]. We are unable to infer the magnitude of anisotropy due to the lack of useful high frequency information. The true distance between the positive fast and negative slow transverse arrivals, which is needed to infer the

magnitude of splitting, has been pushed apart because of the relatively low frequency content of the receiver functions.

4.6 CONCLUSIONS

Our receiver function common conversion point stacks have further substantiated the location of the subducting Pacific Plate inferred from seismicity in the region of Cook Strait, New Zealand. Synthetic seismograms helped us to test this hypothesis and also helped us to conclude that some events observed in the real CCP stack may be due to multiples from slab structure. We have also found that the subducting Pacific plate penetrates the transition zone at the southern extent of our data. While investigating the transition zone discontinuities, we noticed significant energy on the transverse component at the 410 km seismic discontinuity. Based on the relative amplitudes and positions of the radial and transverse positive arrivals for our limited set of backazimuths, we were able to argue that seismic anisotropy must exist above the transition zone and have a fast axis oriented between N1E and N46E but is probably much closer to N1E. This orientation is consistent with both transform deformation inferred from relative plate motions and trench parallel anisotropy observed in many subduction zones.

Acknowledgements: We acknowledge the New Zealand GeoNet project and its sponsors EQC, GNS and FRST, for providing earthquake locations used in this study.

5. CONCLUSIONS

5.1 ABSTRACT

In utilizing several seismic datasets to produce tomographic models and receiver functions and then comparing these results with mineral physics predictions, we have been able to quantify regions of variable composition and thermal structure. Significant amounts of phlogopite and melt are predicted to exist beneath the San Juan mountain range which lie to the west of a minor amount of extension and upwelling north of the Rio Grande rift. Beneath the southern Sierra Nevada, a dipping, seismically slow body has been interpreted as high density iron-rich eclogite in the process of delamination. And in New Zealand, a subduction zone has been imaged with receiver functions in which a thickened transition zone heralds the penetration of the relatively cold Pacific Plate.

5.2 REVIEW

5.2.1 Colorado Rocky Mountains

This study derived the seismic attenuation structure underlying part of the Southern Rocky Mountains and surrounding areas through measurements of differential t^* of S-phase waveforms. It was performed because previous studies of the area, including P, S and surface wave travel time tomography, all indicate slow upper mantle velocities below the Rocky Mountain region and without some knowledge of attenuation, changes in temperature were unknown. A tomographic

model of intrinsic attenuation was then derived. Coupled with current velocity models, we were able to determine the change in temperature as well as address partial melt distributions and compositional variations. A N-S zone of high shear wave attenuation ($Q_s \approx 30$) is found in the mantle beneath the Rocky Mountains and lies east of the region of lowest shear wave velocity. Relationships between shear wave attenuation and shear wave velocity are consistent with both thermal and compositional variability. Along the eastern Colorado Rockies and due north of the Rio Grande Rift, the relationships are consistent with an interpretation of elevated temperatures, up to 50 K at 125 km depth. West of this region low velocities and low attenuation suggest either unusual composition or very high temperatures. We expect that a compositional aspect is most likely in that 3% phlogopite and 0.5% partial melt best accounts for the seismic observations and increased elevations. We then conclude that the low density mantle material beneath the Colorado Rocky Mountains in addition to increased crustal thickness and low density crustal intrusions provides a density contrast sufficient to support its overburden.

5.2.2 Sierra Nevada

Work for the Sierra Nevada follows in a similar sense to the Rocky Mountains except that we also make tomographic models for P and S wavespeeds. Additionally, S wavespeeds are measured in the fast and slow anisotropic directions resulting in S-fast and S-slow tomographic models. This study reveals garnet-rich crust and mantle lithosphere descending into the upper mantle beneath the southeastern Sierra Nevada. Our approach permitted petrological interpretation using only seismic constraints.

Our interpretation predicts layering within the descending lithosphere combining a layer of dense and seismically low-velocity, iron-rich eclogite above a magnesium-rich garnet peridotite layer. These results place descending eclogite above and east of high P wavespeed material previously imaged beneath the southern Great Valley, suggesting a coherence in the lithospheric removal process. We also verified our fast and slow shear wavespeed models and inferred a shallow source for seismic anisotropy by vertically integrating shear wave anisotropy derived from our seismic tomography to reproduce independent SKS splitting measurements.

5.2.3 New Zealand

The work in New Zealand covered not the depths of an ancient mountain belt, but the depths of a complex and active subduction zone. Nor did we create tomographic models but instead generated teleseismic receiver functions derived from broadband seismic arrays on the north end of the South Island and south end of the North Island of New Zealand to image seismic impedance discontinuities in the upper mantle beneath Cook Straight. Impedance discontinuities imaged include the top of the subducting Pacific Plate and the mineral phase boundaries associated with the mantle transition zone. We found that the subducting slab continues south to the extent of our data and is consistent with seismicity that indicates that the slab dips steeply beneath the northwest region of the study area. We also found a thick mantle transition zone, suggesting that the Pacific Plate has penetrated to 660 km. Lastly, we addressed the anisotropic nature of the upper mantle by observing that the 410 km P to S conversion has significant energy on the transverse component and calculating

that the radial and transverse amplitudes can be explained by shear wave anisotropy above the transition zone having a fast axis close to but greater than N1E.

5.3. INNOVATIVE FEATURES AND MAJOR CONTRIBUTIONS

A key to being able to make many of these deductions is correcting the seismic observations for anelasticity. This allows comparison of tomographic models and laboratory measurements. It also allows for the differentiation of compositional and thermal variability. In this regard, contributions to our understanding of the state of the upper mantle in several key locations were made. In the process, several challenges were addressed including the difficulty in interpreting a t* measurement and the correction for anelastic behavior.

5.3.1 Recognizing uncertainty in t*

Though the uncertainty in t* due to random and non-random noise was addressed empirically in Appendix 1, Appendix 4 of this dissertation addresses the problem of temporal interference analytically. This interference can be due to any spurious waveforms including reflections off of the bottom of sedimentary basins for the case of many stations in the Rocky Mountain region or from anisotropy as in the Sierra Nevada.

The correction for t* can be significant. In the work done for the Colorado Rocky Mountains, half of the variance reduction resulted from corrections due to sedimentary basin reverberations. In the Sierra Nevada, rotating the waveforms into

the fast and slow directions reduced the variance of t* by 10% relative to the radial and transverse directions. Interference from spurious waveforms can distort the spectra and result in errors in t* of several hundred percent. We addressed this issue and either corrected for or minimized some types of interference.

5.3.2 Correcting seismic velocities for anelasticity

Seismic velocities must be corrected for anelasticity if comparisons are to be made with laboratory measurements. Investigators can not know if reduced velocities are a result of increased temperatures or anomalous compositions unless attenuation is measured as well. Once attenuation is known, these effects can be separated and potential compositions can be assessed. For the Colorado Rocky Mountains and Sierra Nevada, these effects were separated and compositions were proposed to account for the corrected seismic anomalies.

The correction of velocity for attenuation depends on the frequency dependence of attenuation. In the process of working on the Colorado Rocky Mountains, this dependence was investigated and attenuation was found to vary with frequency raised to the power of 0.25.

5.3.3 The physical state of the upper mantle

The improvements to existing techniques mentioned in the previous sections allowed several breakthroughs in our understanding of the physical state of the upper mantle beneath the Colorado Rocky Mountains and the Sierra Nevada. In the Rocky

Mountains, when seismic velocities were considered in isolation, the true nature of the upper mantle could not be appreciated. Adding the necessarily complementary measurement of attenuation to the measured velocities allowed us to distinguish thermal from compositional anomalies. Whereas previous investigators believed very high temperatures were present beneath the San Juans, we found low attenuation and suggested compositional variability was the culprit. With the added constraint of topography, we concluded that this compositional anomaly might consist of 3% phlogopite and 0.5% partial melt.

A similar analysis was performed for the Sierra Nevada. Previous low resolution tomography revealed an amorphous body of fast P wavespeed material. Many believed this to be the downwelling remnants of the Sierran eclogitic lithosphere. Our much higher resolution tomography showed that this body is rather slab like and rests below a slow P wavespeed body. Further analysis allowed us to suggest that the slow body is iron-rich eclogite, contrary to the common belief that eclogite is relatively seismically fast. Our high resolution tomography also showed a distinct geometry and orientation of delamination of the Sierran lithosphere, thus placing constraints on the lithospheric delamination process.

Several contributions were made to our understanding of the upper mantle beneath New Zealand as well. These include recognizing that the subducting Pacific Plate penetrates the transition zone at the latitude of our southern stations, a contentious issue, placing constraints on the depth dependence of anisotropy - there must be some seismic anisotropy in the upper mantle having a fast axis oriented in nearly the same direction as that measured on SKS waves, and confirming that the

deflections of the transition zone discontinuities are a result of the predicted thermal structure of the subducting slab.

5.4 CHALLENGES FOR THE FUTURE

5.4.1 Technique

One significant contribution of this work was correcting seismic velocities for anelasticity such that comparisons with laboratory measurements are feasible. This was made possible by both being able to interpret t* and knowing the relationship between attenuation and velocity.

Removing or minimizing interference causing uncertainty in t* is vital to obtaining useful attenuation values. Interference can be caused by, as stated before, crustal reverberations and anisotropy, but also by focusing and defocusing, topographic scattering, various converted phases, or any number of other sources. Ideally, synthetics would be created for a given local velocity model incorporating proper topography. t* would then be calculated for these synthetics and applied as corrections (this process could continue through several iterations). These corrections to t* will constantly improve as wavefield simulations garner greater speed and resolution and the resulting attenuation models will have significantly less uncertainty.

Correcting for anelastic behavior is still largely unresolved yet adequate theory exists and must be applied in order to compare seismic tomographic models with laboratory experiments. Perhaps the biggest unknown is whether the relationship

between attenuation and velocity is constant. When we limit our analysis to the region in which we believe there are only thermal variations, e.g. east of the Rocky Mountains, the relationship between velocity and attenuation clearly implies a constant frequency dependence of attenuation with an exponent of about 0.25. However, recent work by Wahr and Benjamin [*Personal communication*] suggests the same exponent at much longer periods but requires attenuation to become very small at the lowest seismic frequencies. Their work is primarily sensitive to the lower mantle, but if it also represents the upper mantle with an appropriate shift in frequency and our datasets are to be consistent, an absorption band must be present. A more accurate definition of the frequency dependence of attenuation is being pursued and will eventually lead to better estimates of composition and thermal structure which are required to assess tectonic models and the processes that forge our Earth.

5.4.2 Tectonics

Though I have been fairly successful in arguing for various tectonic arrangements, greater resolution could certainly strengthen my arguments. Beyond that simple point, the next step in using the understanding obtained from my work is to determine how deformation of the lithosphere will be influenced by these thermal and compositional anomalies. How can various fault and fold systems be reconciled with the predicted deformation?

These techniques can also be applied elsewhere to asses the thermal structure and chemical evolution of upper mantle settings including mountain ranges, subduction zones, and stalled rifts. The resulting knowledge can also be used to

address, as was stated earlier for the Sierra Nevada, the dynamics of the upper mantle, e.g. delamination.

Working in New Zealand sparked an interest in addressing the hydration of the transition zone. Observing the positions of the 410 and 660 km discontinuities and having some appreciation for the upper mantle velocity and transition zone thermal structure will allow an estimate to be made for the hydration of the transition zone. Having this knowledge will allow one to address whether the transition zone is a source or a sink for Earth's water. Eventually we may know at what rate water is being added to or taken from the transition zone, a fact that could have serious consequences for our understanding of the evolution of the Earth's climate. Generous amounts of seismic data exist with which to address this problem and I expect the problem to be solved in the near future.

6. BIBLIOGRAPHY

Aki, K., and P.G. Richards, *Quantitative Seismology*, University Science Books, Sausalito, 2002.

Aleksandrov, K.S., T.V. Ryzhova, and B.P. Belikov, The elastic properties of pyroxenes, *Sov. Phys. Crystallogr.*, *8*, 738, 1963.

Al-Khatib, H.H., and B.J. Mitchell, Upper Mantle Anelasticity and Tectonic Evolution of the Western United-States from Surface-Wave Attenuation, *Journal of Geophysical Research*, *96* (B11), 18129-18146, 1991.

Allen, R.M., G. Nolet, W.J. Morgan, K. Vogfjord, B.H. Bergsson, P. Erlendsson, G.R. Foulger, S. Jakobsdottir, B.R. Julian, M. Pritchard, S. Ragnarsson, and R. Stefansson, The thin hot plume beneath iceland, *Geophysical Journal International*, *137*, 51-63, 1999.

Anderson, D.L., Anelasticity, in *Theory of the Earth*, pp. 279-302, Blackwell Scientific Publications, Boston, 1989.

Anderson, D.L., and J.W. Given, Absorption Band Q Model for the Earth, *Journal of Geophysical Research*, *87* (B5), 3893-3904, 1982.

Anderson, H., and T. Webb, New-Zealand Seismicity - Patterns Revealed by the Upgraded National-Seismograph-Network, *New Zealand Journal of Geology and Geophysics*, *37* (4), 477-493, 1994.

Aranovich, L.Y., and R.G. Berman, A new garnet-orthopyroxene thermometer based on reversed Al_2O_3 solubility in FeO-Al_2O_3-SiO_2 orthopyroxene, *American Mineralogist*, *82*, 345-353, 1997.

Babuska, V., J. Fiala, M. Kumazawa, I. Ohno, and Y. Sumino, Elastic properties of garnet solid-solution series, *Phys. Earth Planet. Inter.*, *16*, 157, 1978.

Bass, J.D., and D.L. Anderson, Composition of the upper mantle: Geophysical tests of two petrological models, *Geophysical Research Letters*, *11*, 237-240, 1984.

Bhattacharyya, J., G. Masters, and P. Shearer, Global lateral variations of shear wave attenuation in the upper mantle, *Journal of Geophysical Research*, *101* (B10), 22273-22289, 1996.

Bhattacharyya, J., Comaprison between Time-Domain and Frequency-Domain Measurement Techniques for Mantle Shear-Wave Attenuation., *Pure and Applied Geophysics*, *153*, 399-417, 1998.

Bina, C.R., and G.R. Helffrich, Calculation of elastic properties from thermodynamic equation of state principles, *Annu. Rev. Earth Planet. Sci.*, *20*, 527-552, 1992.

Bina, C.R., and G. Helffrich, Phase transition Clapeyron slopes and transition zone seismic discontinuity topography, *Journal of Geophysical Research*, *99* (B8), 15853-15860, 1994.

Bostock, M.G., and S. Rodenay, Migration of scattered teleseismic body waves, *Geophysical Journal International*, *173* (3), 732-746, 1999.

Bourne, M., and G. Stuart, *ScSp* observed on North Island, New Zealand: implications for subducting plate structure, *Geophys J Int*, *142* (3), 925-932, 2000.

Biot, M.A., Theory of propagation of seismic waves in a fluid saturated porous solid, I. Low-frequency range, *Journal of the Acoustical Society of America*, *28*, 168-178, 1956.

Boyd, O.S., and A.F. Sheehan, Attenuation tomography beneath the Rocky Mountain Front: Implications for the physical state of the upper mantle, in *AGU Monograph: Lithospheric Structure and Evolution of the Rocky Mountain Region*, edited by K.E. Karlstrom, and G.R. Keller, in Press.

Bromiley, G.D., and A.R. Pawley, The stability of antigorite in the systems MgO-SiO_2-H_2O (MSH) and MgO-Al_2O_3-SiO_2-H_2O (MASH): The effects of Al^{3+} substitution on high-pressure stability, *American Mineralogist*, *88* (1), 99-108, 2003.

Brunner, W., and H.A. Spetzler, Observations of time-dependent meniscus behavior with implications for seismic attenuation in three-phase systems, *Geophysical Research Letters*, *28* (9), 1867-1870, 2001.

Burchfiel, B.C., Tectonostratigraphic map of the Cordilleran Orogen belt: Conterminous United States, Plate 1A in *The Cordilleran Orogen: Conterminous U. S.*, *The Geology of North America*, edited by B. C. Burchfiel, P.W. Lipman, M.L. Zoback, Geol. Soc. of Amer., Boulder, 1992.

Cande, S.C., and J.M. Stock, Pacific-Antarctic-Australia motion and the formation of the Macquarie Plate, *Geophys J Int*, *157* (1), 399-414, 2004.

Catchings, R.D., Regional Vp, Vs, Vp/Vs, and Poisson's Ratios across earthquake source zones from Memphis, Tennessee, to St. Louis, Missouri, *Bulletin of the Seismological Society of America*, *89* (6), 1591-1605, 1999.

Chen, K.C., J.M. Chiu, and Y.T. Yang, Q(P)-Q(S) relations in the sedimentary basin of the Upper Mississippi Embayment using converted phases, *Bulletin of the Seismological Society of America*, *84* (6), 1861-1868, 1994.

Christensen, N.I., Poisson's ratio and crustal seismology, *Journal of Geophysical Research*, *101* (B2), 3139-3156, 1996.

Christensen, N.I., and W.D. Mooney, Seismic velocity structure and composition of the continental crust: A global view, *J. Geophys. Res.*, *100*, 9761, 1995.

Coleman, R.G., D.E. Lee, J.B. Beatty, and W.W. Brannock, Eclogites and eclogites: Their differences and similarities, *Geol. Soc. Am. Bull.*, *76*, 483, 1965.

Danckwerth, A., and R.C. Newton, Experimental determination of the spinel peridotite to garnet peridotite reaction in the system MgO-Al_2O_3-SiO_2 in the range 900-1000^o C and Al_2O_3 isopleths of enstatite in the spinel field, *Contributions to Mineralogy and Petrology*, *66*, 189-201, 1978.

Decker, E.R., H.P. Heasler, K.L. Buelow, K.H. Baker, and J.S. Hallin, Significance of past and recent heat-flow and radioactivity studies in the Southern Rocky Mountain region, *Geological Society of America Bulletin*, *100*, 1851-1885, 1988.

Dodge, F.C.W., J.P. Lockwood, and L.C. Calk, Fragments of the mantle and crust from beneath the Sierra Nevada batholith: Xenoliths in a volcanic pipe near Big Creek, California, *Geol. Soc. Am. Bull.*, *100* (6), 938, 1988.

Ducea, M., Constraints on the bulk composition and root foundering rates of continental arcs: A California arc perspective, *J. Geophys. Res.*, *107* (B11), doi:10.1029/2001JB000643, 2002.

Ducea, M., and S.K. Park, Enhanced mantle conductivity from sulfide minerals, southern Sierra Nevada, California, *Geophys. Res. Lett.*, *27* (16), 2405, 2000.

Ducea, M., and J. Saleeby, Buoyancy sources for a large unrooted mountain range, the Sierra Nevada, California: Evidence from xenolith thermobarometry, *J. Geophys. Res.*, *101*, 8229, 1996.

Ducea, M., and J. Saleeby, The age and origin of a thick mafic-ultramafic keel from beneath the Sierra Nevada batholith., *Contrib. Mineral. Petrol.*, *133*, 169, 1998.

Duffy, T.S., and D.L. Anderson, Seismic Velocities in Mantle Minerals and the Mineralogy of the Upper Mantle, *Journal of Geophysical Research*, *94* (B2), 1895-1912, 1989.

Dueker, K.G., and A.F. Sheehan, Mantle Discontinuity Structure beneath the Colorado Rocky Mountains and High Plains, *J. Geophys. Res.*, *103*, 7153-7169, 1998.

Durek, J.J., and G. Ekstrom, A radial model of anelasticity consistent with long-period surface-wave attenuation, *Bulletin of the Seismological Society of America*, *86* (1), 144-158, 1996.

Dziewonski, A.M., and D.L. Anderson, Preliminary reference Earth model, *Physics of the Earth and Planetary Interiors*, *25* (4), 297-356, 1981.

Eberhart-Phillips, D., and M. Reyners, Continental subduction and three-dimensional crustal structure: The northern South Island, New Zealand, *Journal of Geophysical Research-Solid Earth*, *102* (B6), 11843-11861, 1997.

Farmer, G.L., A.F. Glazner, and C.R. Manley, Did lithospheric delamination trigger late Cenozoic potassic volcanism in the southern Sierra Nevada, California, *Geol. Soc. Am. Bull.*, *114* (6), 754, 2002.

Fei, Y., C.M. Bertka, and B.O. Mysen, Mantle Petrology: Field Observations and High Pressure Experimentation: A tribute to Francis R. (Joe) Boyd, edited by S.M. McLennan, The Geochemical Society, Houston, 1999.

Flanagan, M.P., and P.M. Shearer, Global mapping of topography on transition zone velocity discontinuities by stacking SS precursors, *J. Geophys. Res.*, *103* (B2), 2673-2692, 1998a.

Flanagan, M.P., and P.M. Shearer, Topography on the 410-km seismic velocity discontinuity near subduction zones from stacking of sS, sP, and pP precursors, *J. Geophys. Res.*, *103* (B9), 21156-21182, 1998b.

Fliedner, M.M., S.L. Klemperer, and N.I. Christensen, Three-dimensional seismic model of the Sierra Nevada arc, California, and its implications for crustal and upper mantle composition, *J. Geophys. Res.*, *105* (B5), 10899, 2000.

Fliedner, M.M., S. Ruppert, P.E. Malin, S.K. Park, G. Jiracek, R.A. Phinney, J.B. Saleeby, B. Wernicke, R. Clayton, R. Keller, K. Miller, C. Jones, J.H. Luetgert, W.D. Mooney, H. Oliver, S.L. Klemperer, and G.A. Thompson, Three-dimensional crustal structure of the southern Sierra Nevada from seismic fan profiles and gravity modeling, *Geology*, *24* (4), 367, 1996.

GeoNet, www.geonet.org.nz, 2004.

Ghahremani, F., Effect of grain-boundary sliding on anelasticity of polycrystals, *International Journal of Solids and Structures*, *16* (9), 825-845, 1980.

Gilbert, H.J., A.F. Sheehan, D.A. Wiens, K.G. Dueker, L.M. Dorman, J. Hildebrand, and S. Webb, Upper mantle discontinuity structure in the region of the Tonga Subduction Zone, *Geophysical Research Letters*, *28* (9), 1855-1858, 2001.

Goes, S., R. Govers, and P. Vacher, Shallow mantle temperatures under Europe from P and S wave tomography, *Journal of Geophysical Research*, *105* (B5), 11153-11169, 2000.

Grand, S.P., and D. Helmberger, Upper mantle shear structure of North America, *Geophysical Journal International*, *76*, 399-438, 1984.

Griffin, W.L., S.Y. O'Reilly, and C.G. Ryan, The composition and origin of sub-continental lithospheric mantle, in *Mantle Petrology: Field observations and High Pressure Experimentation: A tribute to Francis R. (Joe) Boyd*, edited by Y. Fei, C.M. Bertka, and B.O. Mysen, pp. 13-46, The Geochemical Society, Houston, 1999.

Gu, Y.J., A.M. Dziewonski, and G. Ekstrom, Simultaneous inversion for mantle shear velocity and topography of transition zone discontinuities, *Geophys J Int*, *154* (2), 559-583, 2003.

Gueguen, Y., and A. Nicolas, Deformation of mantle rocks, *Annu. Rev. Earth Planet. Sci.*, *8*, 119, 1980.

Gutenberg, A., On the layer of relatively low wave velocity at a depth of about 80 kilometers, *Bull. Seismol. Soc. Amer.*, *38*, 121-148, 1948.

Hacker, B.R., G.A. Abers, and S.M. Peacock, Subduction factory 1: Theoretical mineralogy, densities, seismic wave speeds, and H_2O contents, *Journal of Geophysical Research*, *108* (B1), 2029, doi:10.1029/2001JB001127, 2003.

Hacker, B.R., and G.A. Abers, Subduction Factory 3: An Excel worksheet and macro for calculating the densities, seismic wave speeds, and H2O contents of minerals and rocks at pressure and temperature, *Geochem. Geophys. Geosys.*, *5*, doi:10.1029/2003GC000614, 2004.

Hales, A seismic discontinuity in the lithosphere, *Earth Planet. Sci. Lett.*, *7*, 44-46, 1969.

Hammond, W.C., and E.D. Humphreys, Upper mantle seismic wave attenuation: Effects of realistic partial melt distribution, *Journal of Geophysical Research*, *105* (B5), 10987-10999, 2000a.

Hammond, W.C., and E.D. Humphreys, Upper mantle seismic wave velocity: Effects of realistic partial melt geometries, *Journal of Geophysical Research*, *105* (B5), 10975-10986, 2000b.

Hauksson, E., Crustal structure and seismicity distribution adjacent to the Pacific and North America plate boundary in southern California, *Journal of Geophysical Research*, *105* (B6), 13875-13903, 2000.

Hessler, E.K., Upper mantle seismic structure of the Southern Rocky Mountains - Great Plains transition, M.S. thesis, University of Oregon, Eugene, 1997.

Holland, T.J.B., and R. Powell, An internally consistent thermodynamic data set for phases of petrological interest, *Journal of Metamorphic Petrology*, *16*, 309-343, 1998.

Houseman, G.A., and P. Molnar, Gravitational (Rayleigh-Taylor) instability of a layer with non-linear viscosity and convective thinning of continental lithosphere, *Geophys. J. Int.*, *128*, 125, 1997.

Humphreys, E., and K.G. Dueker, Physical state of the western U.S. upper mantle, *Journal of Geophysical Research*, *99* (B5), 9635-9650, 1994.

Jackson, I., Progress in the experimental study of seismic wave attenuation, *Annu. Rev. Earth Planet. Sci.*, *21* (1), 375-406, 1993.

Jacobsen, S.D., J.R. Smyth, and H.A. Spetzler, Sound velocities and elasticity of Fe-bearing hydrous ringwoodite, *In Preparation to be submitted to Physics of the Earth and Planetary Interiors*, 2003.

Jones, C.H., H. Kanamori, and S.W. Roecker, Missing roots and mantle drips: Regional Pn and teleseismic arrival times in the southern Sierra Nevada and vicinity, California, *J. Geophys. Res.*, *99*, 4567, 1994.

Jones, C.H., and R.A. Phinney, Prospecting for the petrology of the upper mantle: Teleseismic shear waves in the Sierra Nevada, California, *Geol. Soc. Amer. Abstr. Prog.*, *31* (7), A-481, 1999.

Jull, M., and P.B. Kelemen, On the conditions for lower crustal convective instability, *J. Geophys. Res.*, *106* (B4), 6423, 2001.

Karato, S., Importance of anelasticity in the interpretation of seismic tomography, *Geophysical Research Letters*, *20* (15), 1623-1626, 1993.

Karato, S., and H. Jung, Water, partial melting and the origin of the seismic low velocity and high attenuation zone in the upper mantle, *Earth and Planetary Science Letters*, *157* (3-4), 193-207, 1998.

Karato, S., and H.A. Spetzler, Defect microdynamics in minerals and solid state mechanisms of seismic wave attenuation and velocity dispersion in the mantle, *Reviews of Geophysics*, *28* (4), 399-421, 1990.

Kelly, K.R., R.W. Ward, S. Treitel, and R.M. Alford, Synthetic seismograms: A finite-difference approach, *Geophysics*, *41* (1), 2-27, 1976.

Kohler, M.D., and D. Eberhart-Phillips, Three-dimensional lithospheric structure below the New Zealand Southern Alps, *Journal of Geophysical Research-Solid Earth*, *107* (B10), 2002.

Kohler, M.D., and D. Eberhart-Phillips, Intermediate-depth earthquakes in a region of continental convergence: South Island, New Zealand, *Bulletin of the Seismological Society of America*, *93* (1), 85-93, 2003.

Komatitsch, D., J. Ritsema, and J. Tromp, The Spectral-Element Method, Beowulf Computing, and Global Seismology, *Science*, *298* (5599), 1737-1742, 2002.

Kumazawa, M., and O.L. Anderson, Elastic moduli, pressure derivatives, and temperature derivatives of single-crystal olivine and single-crystal forsterite, *J. Geophys. Res.*, *74*, 5973, 1969.

Langston, C.A., Effect of Planar Dipping Structure on Source and Receiver Responses for Constant Ray Parameter, *Bull. Seismol. Soc. Amer.*, *67* (1029-1050), 1977.

Lay, T., and T.C. Wallace, Multiple ScS Attenuation and Travel-Times beneath Western North-America, *Bulletin of the Seismological Society of America*, *78* (6), 2041-2061, 1988.

Lee, D.-K., and S.P. Grand, Upper mantle shear structure beneath the Colorado Rocky Mountains, *Journal of Geophysical Research*, *101* (B10), 22233-22244, 1996.

Lerner-Lam, A.L., A.F. Sheehan, S.P. Grand, E. Humphreys, K.G. Dueker, E. Hessler, H. Guo, D.-K. Lee, and M.K. Savage, Deep Structure Beneath the Southern Rocky Mountains from the Rocky Mountain Front Broadband Seismic Experiment, *Rocky Mountain Geology*, *33* (2), 199-216, 1998.

Li, A., D.W. Forsyth, and K.M. Fischer, Evidence for shallow isostatic compensation of the southern Rocky Mountains from Rayleigh wave tomography, *Geology*, *30* (8), 683-686, 2002.

Ligorria, J.P., and C.J. Ammon, Iterative Deconvolution and Receiver-Function Estimation, *Bull. Seismol. Soc. Amer.*, *89*, 1395-1400, 1999.

Ludwig, W.J., J.E. Nafe, and C.L. Drake, Seismic refraction, in *The Sea*, pp. 53-84, Wiley, New York, 1970.

Manley, C.R., A.F. Glazner, and G.L. Farmer, Timing of volcanism in the Sierra Nevada of California: Evidence for Pliocene delamination of the batholithic root?, *Geology*, *28* (9), 811, 2000.

Marson-Pidgeon, K., and M. Savage, Modeling shear-wave splitting at Wellington, New Zealand, *Geophys J Int*, *157*, 853-864, 2004.

Mavko, G.M., Velocity and attenuation in partially molten rocks, *Journal of Geophysical Research*, *85* (NB10), 5173-5189, 1980.

McKenzie, Some remarks on heat flow and gravity anomalies, *J of Geophys. Res.*, *72*, 6261-6273, 1967.

Meju, M.A., Error analysis in linear inversion, in *Geophysical data analysis: Understanding inverse problem theory and practice*, pp. 294, Society for Exploration Geophysicists, Tulsa, 1994.

Menke, W., Singular Value Decomposition and the Natural Generalized Inverse, in *Geophysical Data Analysis: Discrete Inverse Theory*, pp. 119-124, Academic Press, Orlando, 1984.

Minster, J.B., and D.L. Anderson, A model of dislocation-controlled rheology for the mantle, *Philosophical Transactions of the Royal Society of London Series a-Mathematical Physical and Engineering Sciences*, *299* (1449), 319-356, 1981.

Molnar, P., H.J. Anderson, E. Audoine, D. Eberhart-Phillips, K.R. Gledhill, E.R. Klosko, T.V. McEvilly, D. Okaya, M.K. Savage, T. Stern, and F.T. Wu, Continous deformation versus faulting through the continental lithosphere of New Zealand, *Science*, *286* (5439), 516-519, 1999.

Muller, R.D., W.R. Roest, J.Y. Royer, L.M. Gahagan, and J.G. Sclater, Digital isochrons of the world's ocean floor, *Journal of Geophysical Research*, *102* (B2), 3211-3214, 1997.

Mutschler, F.E., E.E. Larson, and R.M. Bruce, Laramide and younger magmatism in Colorado - new petrologic and tectonic variations on old themes, *Colorado School on Mines Quarterly*, *1*, 1-47, 1987.

Nataf, H.C., and Y. Ricard, An a priori tomographic model of the upper mantle based on geophysical modeling, *Physics of the Earth and Planetary Interiors*, *95*, 101-122, 1996.

Nowick, A.S., and B.S. Berry, *Anelastic Relaxation in Crystalline Solids*, 677 pp., Academic Press, New York, 1972.

O'Connell, R.J., and B. Budiansky, Viscoelastic properties of fluid-saturated cracked solids, *Journal of Geophysical Research*, *82* (36), 5719-5735, 1977.

Patton, H.J., and S.R. Taylor, Q structure of the Basin and Range from surface waves, *Journal of Geophysical Research*, *89* (B8), 6929-6940, 1984.

Percival, D.B., and A.T. Walden, *Spectral Analysis for Physical Applications: Multitaper and Conventional Univariate Techniques*, Cambridge University Press, Cambridge, 1993.

Polet, J., and H. Kanamori, Anisotropy Beneath California: Shear Wave Splitting Measurements Using a Dense Broadband Array, *Geophys. J. Int.*, *149* (2), 313, 2002.

Prodehl, C., and P.W. Lipman, Crustal structure of the Rocky Mountain region, in *Geophysical framework of the continental United States*, edited by W.D. Mooney, pp. 249-284, Geol. Soc. of Amer., Boulder, 1989.

Reid, F.J.L., J.H. Woodhouse, and H.J. van Heijst, Upper mantle attenuation and velocity structure from measurements of differential S phases, *Geophysical Journal International*, *145*, 615-630, 2001.

Revenaugh, J., and T.H. Jordan, Mantle layering from *ScS* reverberations 3. The upper mantle, *J. Geophys. Res.*, *96* (B12), 19781-19810, 1991.

Reyners, M., and E. Robertson, Intermediate depth earthquakes beneath Nelson, New Zealand, and the southwestern termination of the subducted Pacific plate, *Geophysical Research Letters*, *31*, doi:10.1029/2003GL019201, 2004.

Reyners, M., R. Robinson, and P. McGinty, Plate coupling in the northern South Island and southernmost North Island, New Zealand, as illuminated by earthquake focal mechanisms, *Journal of Geophysical Research-Solid Earth*, *102* (B7), 15197-15210, 1997.

Ringwood, A.E., *Composition and Petrology of the Earth's Mantle*, 618 pp., McGraw-Hill, New York, 1975.

Romanowicz, B., A global tomographic model of shear attenuation in the upper mantle, *Journal of Geophysical Research*, *100*, 12375-12394, 1995.

Romanowicz, B., Attenuation tomography of the Earth's mantle:A review of current status, *Pure and Applied Geophysics*, *153*, 257-272, 1998.

Roth, E.G., D.A. Wiens, L.M. Dorman, J. Hildebrand, and S.C. Webb, Seismic attenuation tomography of the Tonga-Fiji region using phase pair methods, *Journal of Geophysical Research*, *104* (B3), 4795-4809, 1999.

Roth, E.G., D.A. Wiens, and D.P. Zhao, An empirical relationship between seismic attenuation and velocity anomalies in the upper mantle, *Geophysical Research Letters*, *27* (5), 601-604, 2000.

Rubie, D.C., and C.R.I. Ross, Kinetics of the olivine-spinel transformation in subducting lithosphere, *Phys. Earth Plant. Inter.*, *86*, 223-241, 1994.

Saleeby, J., M. Ducea, and D. Clemens-Knott, Production and loss of high-density batholithic root, southern Sierra Nevada, California, *Tectonics*, *22* (6), 1064, doi:10.1029/2002TC001374, 2003.

Sato, H., and M.P. Ryan, Generalized Upper Mantle Thermal Structure, in *Magmatic Systems*, edited by M.P. Ryan, pp. 259-290, Academic Press, New York, 1994.

Sato, K., T. Katsura, and E. Ito, Phase relations of natural phlogopite with and without enstatite up to 8 GPa: implication for mantle metasomatism, *Earth and Planetary Science Letters*, *146*, 511-526, 1997.

Savage, M.K., O.S. Boyd, A.F. Sheehan, and C.H. Jones, Dipping and anisotropic structure in the upper mantle beneath New Zealand from receiver functions, *in progress*, 2004.

Sheehan, A.F., G.A. Abers, C.H. Jones, and A. Lerner-Lam, Crustal thickness variations across the Colorado Rocky Mountains from teleseismic receiver functions, *Journal of Geophysical Research*, *100* (B10), 20391-20404, 1995.

Sheehan, A.F., and S.C. Solomon, Differential Shear Wave Attenuation and Its Lateral Variation in the North Atlantic Region, *Journal of Geophysical Research*, *97* (B11), 15339-15350, 1992.

Slack, P.D., P.M. Davis, W.S. Baldridge, K.H. Olsen, A. Glahn, U. Achauer, and W. Spence, The upper mantle structure of the central Rio Grand rift region from teleseismic P and S wave travel time delays and attenuation, *Journal of Geophysical Research*, *101* (B7), 16003-16023, 1996.

Smyth, J.R., and D.J. Frost, The effect of water on the 410-km discontinuity: An experimental study, *Geophysical Research Letters*, *29* (10), doi:10.1029/2001GL014418, 2002.

Smyth, J.R., C.M. Holl, D.J. Frost, and S.D. Jacobsen, High pressure crystal chemistry of hydrous Ringwoodite and water in the Earth's interior, *Submitted to Physics of the Earth and Planetary Interiors*, 2003.

Snelson, C.M., T.J. Henstock, G.R. Keller, K.C. Miller, and A. Lavender, Crustal and uppermost mantle structure along the Deep Probe seismic line, *Rocky Mountain Geology*, *33* (2), 181-198, 1998.

Sobolev, S.B., H. Zeyen, G. Stoll, F. Werling, R. Altherr, and K. Fuchs, Upper mantle temperatures from teleseismic tomography of French Massif Central including effects of composition, mineral reactions, anharmonicity, anelasticity, and partial melt, *Earth and Planetary Science Letters*, *139*, 147-163, 1996.

Stacey, F.D., Thermal parameters of the Earth, in *Physics of the Earth*, pp. 457-460, Brookfield Press, Kenmore, Brisbane, 1992.

Stein, S., and C.A. Stein, Thermo-mechanical evolution of oceanic lithospere: implications for the subduction process and deep earthquakes, in *Subduction:*

Top to Bottom, edited by J.P. Platt, pp. 1-18, American Geophysical Union, Washington, D.C., 1996.

Stern, T., P. Molnar, D. Okaya, and D. Eberhart-Phillips, Teleseismic P wave delays and modes of shortening the mantle lithosphere beneath South Island, New Zealand, *Journal of Geophysical Research-Solid Earth*, *105* (B9), 21615-21631, 2000.

Stewart, D., Earth velocity structure from an earthquake recording array, Honours thesis thesis, Victoria University of Wellington, Wellington, 1998.

Stuart, G., D. Francis, D. Gubbins, and G. Smith, Tararua broadband array, North Island, New Zealand, *Bull. Seismol. Soc. Amer.*, *85* (1), 325-333, 1995.

Schutt, H., J. Kohler, O. Boyd, and H. Spetzler, Seismic attenuation in partially saturated dime-shaped cracks, *Pure and Applied Geophysics*, *157* (3), 435-448, 2000.

Tarantola, A., *Inverse Problem Theory: Methods for Data Fitting and Model Parameter Estimation*, 613 pp., Elsevier Science, New York, 1987.

Turcotte, D.L., and E.R. Oxburgh, Finite amplitude convective cells and continental drift, *J. Fluid Mech.*, *28*, 29-42, 1967.

van Keken, P.E., B. Kiefer, and S.M. Peacock, High-resolution models of subduction zones: Implications for mineral dehydration reactions and the transport of water into the deep mantle, *Geochem. Geophys. Geosys.*, *3* (10), doi:10.1029/2001GC000256, 2002.

Walck, M.C., The P-wave upper mantle structure beneath an active spreading center: The Gulf of California, *Geophysical Journal of the Royal Astronomical Society*, *76*, 697-723, 1984.

Walck, M.C., The upper mantle beneath the north-east Pacific rim: A comparison with the Gulf of California, *Geophysical Journal of the Royal Astronomical Society*, *81*, 243-276, 1985.

Wannamaker, P.E., J.B. Hulen, and M.T. Heizler, Early Miocene lamproite from the Colorado Plateau tectonic province, Southeastern Utah, USA, *Journal of Volcanology and Geothermal Research*, *96*, 175-190, 2000.

Warren, L.M., and P.M. Shearer, Investigating the frequency dependence of mantle Q by stacking P and PP spectra, *Journal of Geophysical Research-Solid Earth*, *105* (B11), 25391-25402, 2000.

Watt, J.P., G.F. Davies, and J. O'Connell, The elastic properties of composite minerals, *Rev. Geophys. Space Phys.*, *14*, 541, 1976.

Wernicke, B., R. Clayton, M. Ducea, C.H. Jones, S. Park, S. Ruppert, J. Saleeby, J.K. Snow, L. Squires, M. Fliedner, G. Jiracek, R. Keller, S. Klemperer, J. Luetgert, P. Malin, K. Miller, W. Mooney, H. Oliver, and R. Phinney, Origin of High Mountains in the Continents: The Southern Sierra Nevada, *Science*, *271* (5246), 190, 1996.

Wilshire, H.G., C.E. Meyer, J.K. Nakata, L.C. Calk, J.W. Shervais, J.E. Nielson, and E.C. Schwarzman, Mafic and ultramafic xenoliths from volcanic rocks of the western United States, *U. S. G. S. Professional Paper*, *1443*, 179, 1988.

Wilson, C., C. Jones, and A. Sheehan, Lithospheric Structure of a Continental Strike-Slip Boundary, Marlborough Fault Zone, South Island, New Zealand, *EOS Trans. AGU*, *82* (47), Abstract T11D-0882, 2001.

Wilson, C.K., C.H. Jones, P. Molnar, A.F. Sheehan, and O.S. Boyd, Evidence for continuous deformation in the lower crust and upper mantle beneath a continental strike-slip fault zone: Marlborough Fault System, South Island, New Zealand, *Geology*, *in press*, 2004.

Zandt, G., The Southern Sierra Nevada drip and the mantle wind direction beneath the Southwestern United States, *Int. Geol. Rev.*, *45*, 213, 2003.

APPENDIX 1. SOURCES OF ERROR

A1.1 ERRORS DUE TO NON RANDOM NOISE AND THE SEDIMENTARY BASIN CORRECTION

Interference produced by non random noise, specifically a set of reflections from the bottom of a sedimentary basin, can lead to significant apparent δt^*. Though the only source accounted for in this study, this type of error can also be caused by shear wave splitting, S to P conversions, and focusing/defocusing. The contribution to δt^* from this effect can produce larger values than those due to a highly attenuating upper mantle. Contributions to δt^* from intrinsic attenuation in the basin are negligible since the travel time through the sediments is small. For example, a seismic wave traveling through a 4 km thick basin with a shear velocity of 2 km/s will spend 2 seconds in the basin. If the basin has a Q of 50, t^* will be 0.04, an order of magnitude smaller that the correction due to basin reflections. In this section, different reflectivity series corresponding to a range in arrival times of the first reflector are convolved with the event waveforms in Figure A1.1, event #405 and event #412, and apparent δt^* is calculated for the reverberating time series relative to the original.

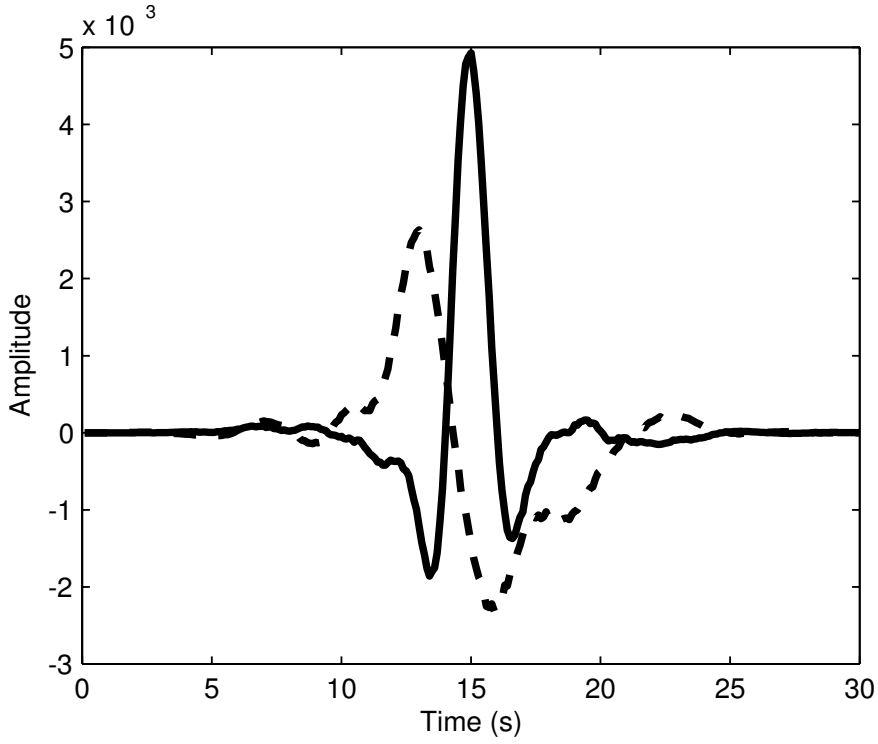

Figure A1.1. Two reference signals where the reference signal is the aligned stack of all S-waves for a given event. The dashed curve is Event #405 and the solid curve is Event #412.

Figure A1.2 shows the apparent δt^* for the two example event waveforms in Figure A1.1 in dependence on the time of the first reflected arrival. The curves represent a case with a normal incident reflection coefficient of -0.3, a typical value expected for the bottom of a sedimentary basin. For a 4 km thick basin with a shear velocity of 2 km/s, a possible scenario for the stations in the Denver Basin, the first reflected arrival will lag the direct arrival by 4 seconds. Depending on the event shape, apparent δt^* could be about -0.5 seconds.

The functional relationship between δt^* error and time lag between the direct arrival and the reflected waves depends on the temporal shape and extent of the event pulse, the relative size between the direct arrival and the reflection, and the frequency range over which the δt^* measurement is made. Apparent δt^* due to basin reflections

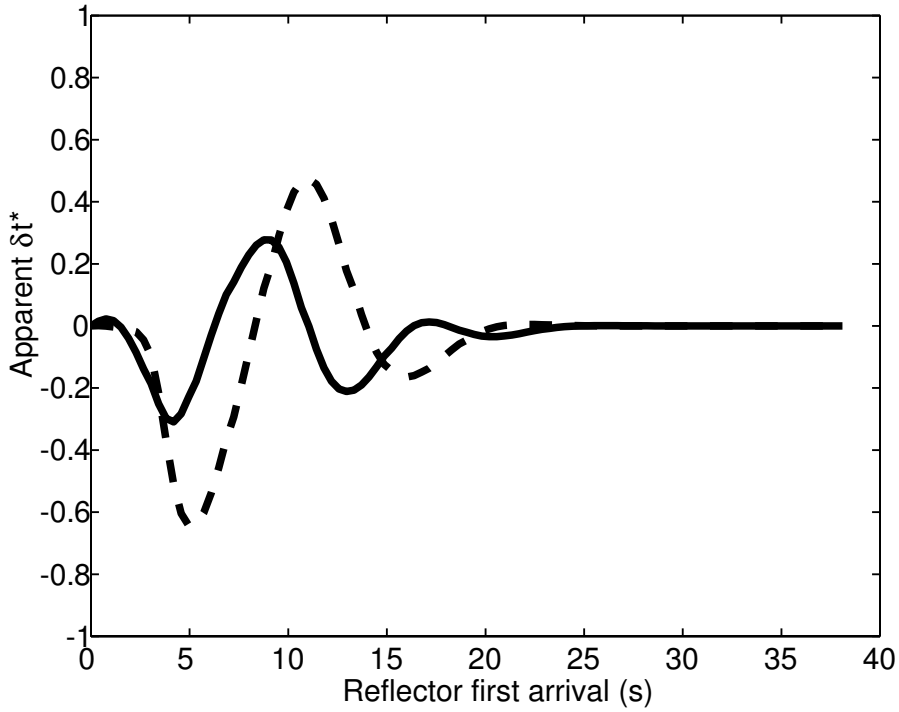

Figure A1.2. Apparent δt^* versus time of arrival for the first reflector due to a normal incident reflection coefficient of -0.3. The results are for the signals in Figure A1.1 (dashed curve – Event #405, solid curve – Event #412). For long offsets, the reflection is no longer in the window of interest and apparent δt^* goes to zero. At shorter offsets, apparent δt^* oscillates at different rates depending on the frequencies with which δt^* is measured and the shape of the source time series. The range in time of arrival for the first reflector from the bottom of sedimentary basins in this study is 0.5 to 5.2 seconds. Reflections from the bottom of the crust would come in around 25 seconds.

is calculated for all stations sitting on known sedimentary basins. A synthesized reflectivity sequence is convolved with each event pulse. The reflectivity sequence is generated using basin thicknesses reported by Sheehan et al. [1995] and Burchfiel [*Plate 1A*, 1992] and rock densities and P-wave velocities estimated for the crust and basins of Colorado by Snelson et al. [1998] and Prodehl and Lipman [1989]. To obtain shear wave velocities, we assume V_p/V_s of 1.75 in the crust and 2.0 in the basins [*Sheehan et al.*, 1995; *Catchings*, 1999; *Hauksson*, 2000; *Ludwig et al.*, 1970; *Christensen*, 1996]. The value for the basin V_p/V_s ratio was determined by

maximizing the δt^* variance reduction for different values of basin V_p/V_s ratio. The variance reduction of δt^* for the Q^{-1} tomography due solely to basin reflections is 11%. The mean δt^* correction is -0.11, the maximum, 0.05, and minimum, -0.86. Specific values for the corrections are listed in Table 3.

A1.2 ERRORS DUE TO RANDOM NOISE.

Our next goal is to determine the effect of random temporal noise on the measurement of δt^*. Two reference time series, event #405 and event #412 (Figure A1.1), which represent extremes in sensitivity to temporal noise are contaminated in the time domain with varying levels of normally distributed random noise. For each level of noise, a noise vector is generated and multiplied by a gaussian taper, added to the signal and the signal to noise ratio and δt^* are measured. The signal to noise ratio is measured as described in Section 2 except that the noise spectrum is calculated from the tapered noise vector. δt^* is measured as in Section 2 and measured relative to the clean signal. The process is repeated 1000 times for each noise level to derive the standard deviation of δt^* due to that level of normally distributed random noise.

Figure A1.3 shows the effect of noise on the example reference time series where the standard deviation of δt^* is plotted versus the noise to signal ratio. As the noise to signal ratio increases, the standard deviation of δt^* increases approaching values of 2.5 seconds. The relationship between the standard deviation of δt^* and noise to signal ratio is approximately linear for small to moderate values of the noise to signal ratio and for most of the δt^* data used in the Q^{-1} tomography study. We assume that the noise in our signals for this study can be described by a normally

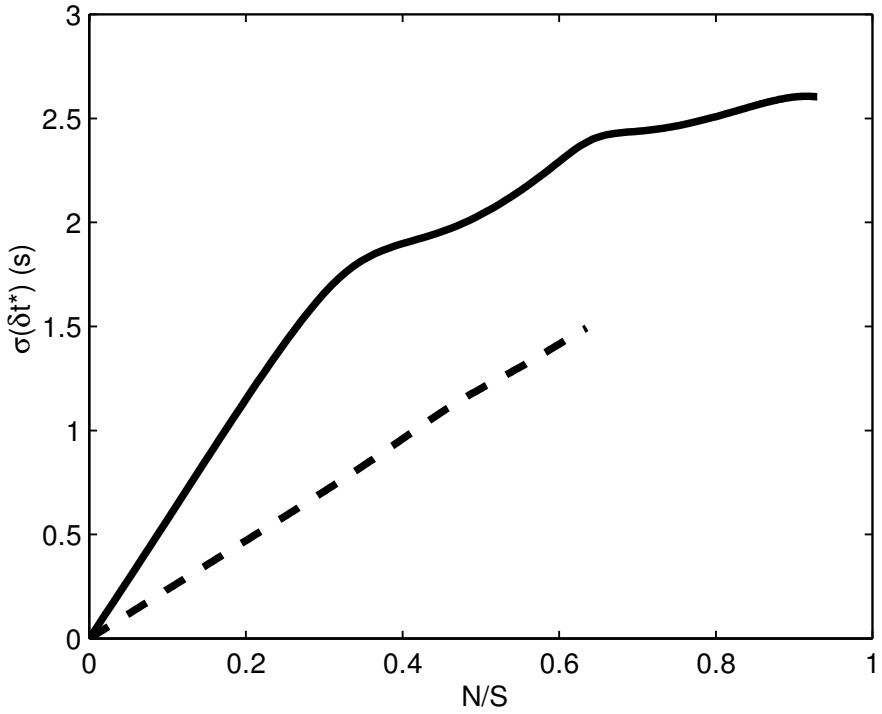

Figure A1.3. The sensitivity of the reference signals in Figure A1.1 to random noise (dashed curve – Event #405, solid curve – Event #412). These two signals produce extremes in sensitivity, the slope between the standard deviation of δt^* and the noise to signal ratio (Table 2).

distributed random process and use the slopes of standard deviation of δt^* versus the noise to signal ratio derived from Figure A1.3 (Table 2) for each event and the signal to noise ratios for each signal (Table 3) to derive the standard deviation of δt^* for each measurement. The inverse of these values are applied as weights in the inversion. This analysis leads to the conclusion that 75% of the variance of δt^* for this study, after accounting for basin reflections, is due to normally distributed random noise.

APPENDIX 2. MODEL RESOLUTION

Typically the resolution matrix will give you an estimate of the uniqueness of a solution based only on the ray path geometry, $d\bar{\tau}^{1}$. The resolution matrix, R, is defined

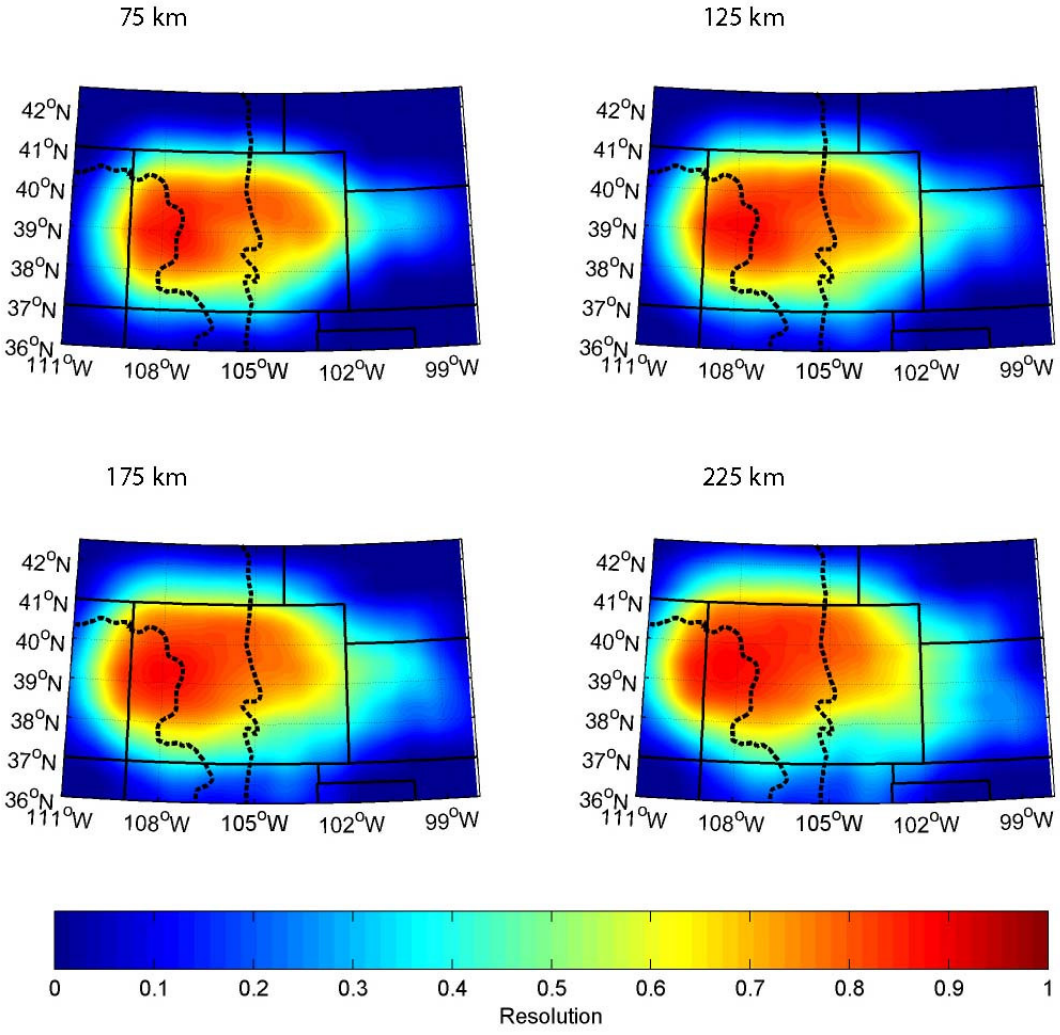

Figure A2.1. Resolution matrix showing model resolution at four depths. The resolution increases to near one throughout most of the upper mantle beneath Colorado.

$$R = M_p M_p^T \tag{A2.1}$$

where M_p is the matrix of eigenvectors defined in (11). Figure A2.1 shows that the resolution across most of the Colorado Rocky Mountains is near 1.0. The resolution matrix as defined here, however, does not account for uncertainty in the observations.

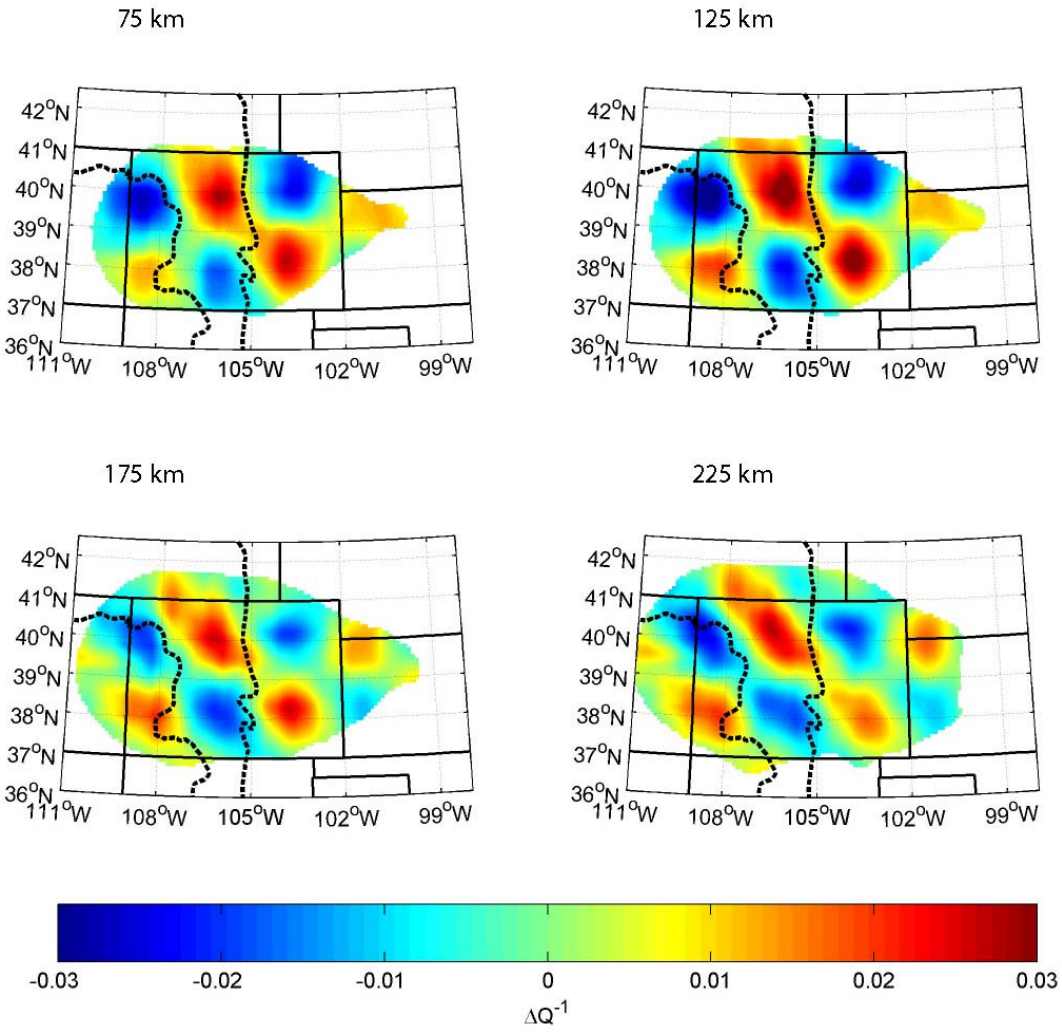

Figure A2.2. Checkerboard results for observations without error at four depths. Input model consists of 200 × 200 × 400 km blocks of alternating attenuation, +0.03 and -0.03. The checkerboard remains fairly well resolved where the resolution is high.

To assess the effect of uncertainty in δt^* on the resolution of the solution, we use checkerboard tests.

The checkerboard model is composed of 200 × 200 × 400 km blocks having an attenuation, ΔQ^{-1}, of either +0.03 or -0.03. Observations are produced according to equation 9, and the inversion is performed as outlined in Section 3. One can take the synthetic observations and re-invert for the model to estimate model resolution (Figure A2.2). An inspection of Figure A2.2 shows that the ray geometry provides good resolution. Areas within the model remain well resolved while areas along the edges of the model space become distorted. The true resolution, however, can only be considered when errors are introduced to the observations [*Tarantola*, 1987]. The problem is estimating the proper amount of error to add to the observations.

In Appendix 1.1, we found that based on our data's signal to noise ratios and the shape of the reference time series, normally distributed random noise accounts for 75% of the δt^* data variance. A random value scaled by a constant multiplied by the standard deviation of δt^* is added to the checkerboard data. The constant is determined by requiring that 75% of the checkerboard data variance is due to random error, the same condition that is present in the real data. The standard deviation of δt^* is also used as the inverse of the weight in the inversion. It is found by dividing the data's signal to noise ratio (Table 3) by the slope of the standard deviation of apparent δt^* versus the synthetic noise to signal ratio (Section 1.2; Table 2). Now having some idea of the error in the observations and how to weight the inversion, we can interpret a more representative checkerboard test to assess model resolution (Figure A2.3). The inverted checkerboard model is only slightly more distorted than the inversion

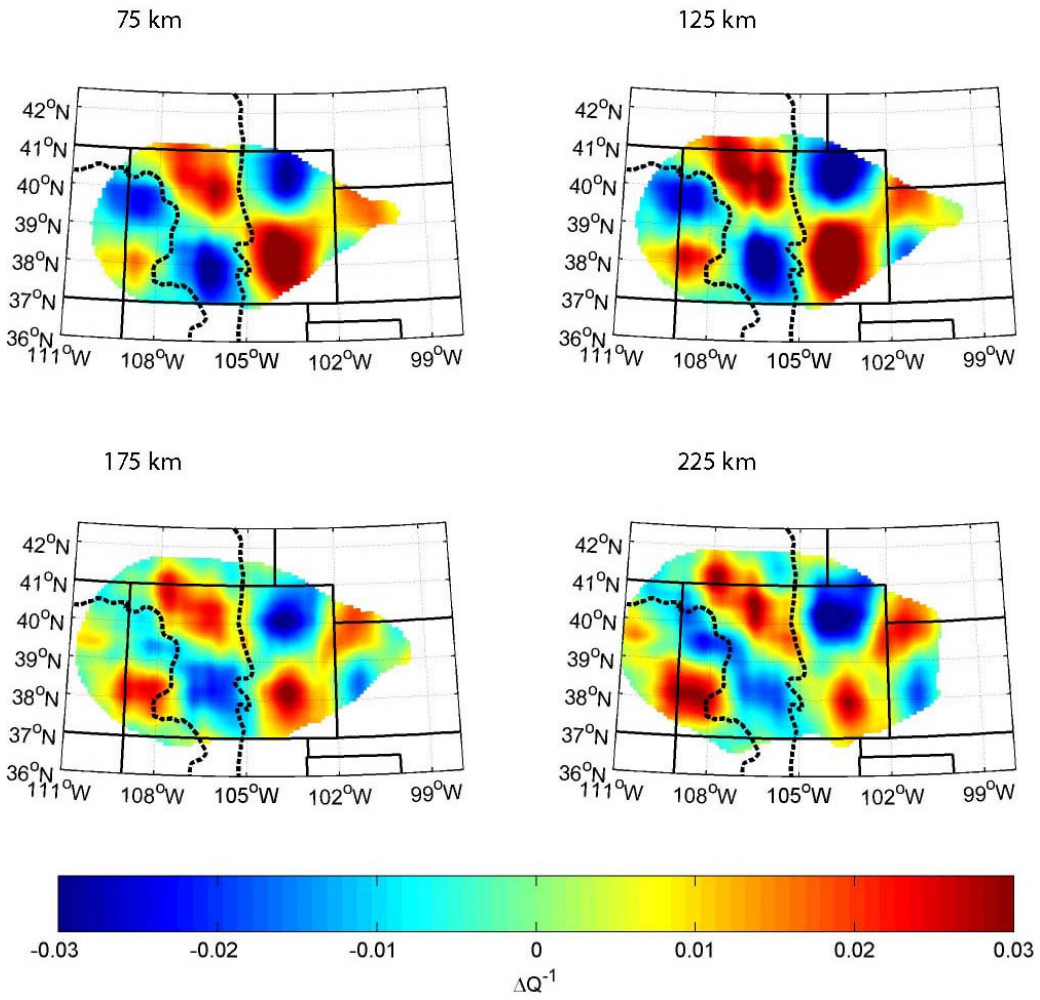

Figure A2.3. Checkerboard results for observations t^* with random error that is 75% of the data variance at four depths. The resulting variance reduction of the checkerboard t^* data is 10%. Resolution continues to be good though becomes increasingly distorted with depth.

without error. The amplitude of variations between checkers is amplified which helps to counteract the effect of damped intrinsic δt^* values from the tapering processes. The checkerboard results suggest that a properly weighted inversion, even with the amount of random error expected for our data set, can still produce reasonable results.

APPENDIX 3. SUPPORTING ONLINE MATERIAL FOR: FOUNDERING LITHOSPHERE IMAGED BENEATH THE SOUTHERN SIERRA NEVADA, CALIFORNIA, USA

A3.1 METHOD

The network of 24 broadband seismometers comprising the seismological component of the Sierran Paradox Experiment was deployed from late May to mid October 1997 (Fig. 1, Table S1). Stations were approximately 20 km apart spanning an area of nearly 3 x 10^4 km^2. Approximately 40 teleseismic events of appropriate distance range and magnitude for this study yielded 800 seismic traces to measure (Table S2). We have measured direct P, S_{fast}, and S_{slow}-wave travel time delays, t_p, t_{sf}, and t_{ss}, and S_{fast}-wave path integrated attenuation, Δt^*, to invert for variations in P-wave velocity, v_p, the ratio of P-wave to S-wave velocity, v_p/v_s, %S anisotropy, and S_{fast}-wave attenuation, Q^{-1}_s.

S-wave delay times are measured using the fast (N80°E) and slow (N10°W) components of motion as determined from SKS shear-wave splitting measurements [*Polet and Kanamori*, 2002; *Jones and Phinney*, 1999] and facilitates an appreciation for the depth dependence of anisotropy. Relative travel times are measured by cross-correlating waveforms that have been bandpass filtered from 1 to 100 seconds; across the array the shapes of teleseismic arrivals are found to vary only slightly and cross-correlation should give reliable measurements of differential arrival times.

The horizontal channels are rotated into the fast and slow directions prior to measuring spectral ratios. A straight line is fit to the spectral ratio between 10 and 30

Table S1. Station Information. Station statics result after correcting for elevation.

Name	Longitude	Latitude	Elevation (km)	P wavespeed station static (s)	S_{fast}	S_{slow}	S_{fast} Δt^* station static (s)	S_{slow}
ARC2	-118.3323	36.0106	2.60	0.162	0.01	0.05	0.3	-0.4
BGR	-119.0166	36.6283	0.95	-0.100	-0.18	-0.23	-0.5	0.0
BPC	-118.4306	37.1282	2.37	0.131	0.44	0.91	0.6	0.4
BRR	-119.0394	36.9127	1.29	0.119	0.14	-0.29	0.0	0.7
BVC	-117.8628	36.7265	0.48	0.281	-0.19	0.40	0.5	0.0
CCC	-118.7868	36.5778	1.56	0.042	0.29	0.60	0.6	0.3
CHP	-118.0919	35.8938	2.43	0.168	0.48	0.37	0.4	-0.2
CPR	-118.5758	36.7967	1.60	-0.233	-0.20	-0.21	0.4	0.1
DP00	-117.6410	36.2670	1.73	0.332	0.14	0.38	0.2	0.4
FLL	-118.9723	37.2798	2.22	0.097	0.60	0.31	0.4	0.3
HVY	-119.3015	36.7200	0.22	-0.325	-0.36	-1.20	0.5	0.3
JUN	-118.4110	36.5810	2.52	-0.050	0.08	0.19	0.7	-0.1
LMC	-119.0291	36.3580	0.23	-0.056	-0.25	-0.12	0.0	0.3
MKW3	-118.6060	36.4540	2.36	0.005	1.51	1.03	0.0	-0.7
OVY	-118.3280	36.7777	2.73	0.005	0.06	-0.04	0.7	-0.1
PDC	-118.9779	36.0333	0.20	-0.087	-0.62	-0.72	0.0	0.0
SFK	-118.8146	36.3656	0.84	0.074	-0.08	-0.23	0.3	0.9
SFT	-118.0627	36.2303	1.83	0.203	0.26	0.18	0.1	0.7
SLC	-117.7175	36.5245	1.94	-0.019	0.05	0.61	-0.4	-1.2
SMD	-118.6302	36.9709	1.81	0.034	-0.37	-0.09	-0.2	0.2
SRF	-118.1060	36.9360	2.18	-0.015	-0.30	0.07	0.3	-0.5
TWR2	-118.4066	36.3513	1.97	-0.011	0.36	-0.03	0.9	0.3
WHP	-118.2216	36.5885	2.42	0.026	0.30	0.32	0.5	0.0
WMD	-118.5749	36.1979	2.67	0.094	0.34	0.14	0.2	-0.4

seconds to derive Δt^* (Chapter 2) [*Boyd and Sheehan*, in Press]. Rotating into the fast and slow directions keeps the second wavelet due to splitting from interfering with the primary wavelet's spectra, thereby reducing Δt^* error (Chapter 2). No other correction for Δt^* is made, as is evident by the low variance reduction attained by the differential attenuation tomographic model (~25%). This value is low but much greater than a previous study in which 10% variance reduction was shown to be adequate to resolve subsurface features. Boyd and Sheehan [in Press] (Chapter 2) show that interference from basin reverberations, anisotropy, and other forms of scattering can lead to significant errors in Δt^*. They also point out that if

uncorrelated, these uncertainties will cancel and a meaningful differential attenuation tomographic model can be obtained. The effect of focusing and defocusing on Δt^* is expected to be small based on the location, extent and magnitude of the velocity anomalies (Chapter 2).

Inversion of the P and S-wave differential travel times and S-wave Δt^* to produce the tomographic models of differential slowness and attenuation is performed according to the integral equations

$$\partial t_x = \int \partial \frac{1}{v_x} dl$$
$$\partial t_x^* = \int \partial \frac{1}{v_x Q_x} dl \qquad \text{(S1)}$$

where the subscript x represents either the P (for velocity), S_{slow}, or S_{fast} waves. The distances spent along the ray path are given by dl. In our method, a primary block size of 50 km is chosen because it has sufficient ray density to produce a good average. We perform an inversion using weighted singular value decomposition where the weights are the inverse of the standard errors for each measurement derived from the signal to noise ratio of the waveforms. The blocks are translated 5 km until inversions are obtained for all possible translations generating a total of 10 x 10 x 10 or 1000 inversions. They are sequentially combined and subsequently convolved with a 25 km cube to produce a smooth tomographic model [*Boyd and Sheehan*, in Press]. We iterate the inversions four times using the residuals relative to the previous iteration as input data. The residuals are defined as the original data minus the predicted data

Table S2. Event information. The last two columns represent the number of stations used for the P and S-wave measurements.

Date	Longitude	Latitude	Depth (km)	Backazimuth (degrees)	Distance (degrees)	P-wave slowness (s/km)	S-wave slowness (s/km)	#P	#S
7/20/97 00:30:21 UTC	-167.5	52.6	14	311.2	37.6	0.076	0.136	22	22
7/20/97 10:14:22 UTC	-66.3	-23.0	256	131.8	77.1	0.050	0.096	21	20
9/02/97 12:13:25 UTC	-75.7	3.9	222	119.5	50.9	0.067	0.123	17	17
9/04/97 04:23:36 UTC	178.3	-26.5	618	233.2	86.7	0.042	0.083	21	21
7/21/97 23:19:39 UTC	-71.9	-30.3	33	140.5	79.8	0.049	0.094	22	22
9/10/97 12:57:10 UTC	-174.4	-21.3	33	232.1	78.3	0.050	0.096	22	22
7/25/97 06:47:03 UTC	-71.8	-30.2	33	140.3	79.8	0.049	0.095	22	22
6/10/97 21:53:55 UTC	-108.1	-35.8	10	171.3	72.9	0.053	0.102	12	11
7/27/97 05:21:29 UTC	-71.8	-30.4	33	140.5	79.9	0.049	0.094	21	21
7/28/97 06:46:55 UTC	142.7	22.3	33	293.2	83.6	0.046	0.090	22	22
6/17/97 21:03:40 UTC	-179.4	51.3	33	309.3	44.9	0.072	0.130	15	12
9/20/97 16:11:32 UTC	-177.6	-28.7	33	229.1	85.7	0.045	0.088	21	22
6/25/97 03:54:12 UTC	-173.2	-15.9	33	235.0	73.6	0.053	0.101	19	15
6/26/97 06:12:09 UTC	-82.5	4.8	10	125.2	45.7	0.071	0.129	19	15
6/26/97 19:21:08 UTC	-114.3	-49.7	10	177.4	86.3	0.044	0.087	19	14
8/08/97 22:27:23 UTC	-179.2	-15.5	33	239.6	77.3	0.050	0.097	21	21
6/27/97 04:39:52 UTC	-26.7	38.3	10	56.9	69.5	0.056	0.106	19	15
8/13/97 04:45:04 UTC	125.8	25.0	55	305.2	93.8	0.041	0.078	20	20
9/30/97 06:27:28 UTC	141.9	32.0	33	301.5	78.5	0.050	0.096	21	21
6/30/97 15:47:39 UTC	-155.1	19.4	8	251.9	36.3	0.077	0.137	19	15
6/30/97 18:56:27 UTC	-80.8	-4.1	33	130.8	53.6	0.066	0.122	19	15
8/15/97 07:37:49 UTC	-105.7	-4.4	10	161.1	42.6	0.073	0.132	20	20
8/17/97 20:11:11 UTC	167.4	-13.7	33	249.6	85.9	0.044	0.088	20	20
8/18/97 12:24:26 UTC	-72.0	-29.9	33	140.3	79.4	0.049	0.095	19	19
10/04/97 15:29:46 UTC	-46.7	15.9	10	87.4	66.1	0.058	0.109	19	0
10/04/97 15:34:29 UTC	-46.8	16.0	10	87.4	65.9	0.058	0.109	19	0
7/05/97 22:46:41 UTC	164.7	-11.5	33	253.0	86.5	0.044	0.087	19	15
7/06/97 09:54:02 UTC	-71.8	-30.1	33	140.2	79.6	0.049	0.095	20	16
7/06/97 20:13:37 UTC	-88.0	16.1	33	119.0	33.8	0.078	0.139	20	16
7/06/97 23:15:20 UTC	-71.9	-30.2	33	140.4	79.7	0.049	0.095	18	17
7/08/97 02:24:07 UTC	142.7	23.8	33	294.3	82.8	0.047	0.091	21	18
7/08/97 12:11:14 UTC	-178.6	51.4	33	309.4	44.4	0.072	0.131	21	18
7/09/97 19:24:11 UTC	-63.6	10.5	10	103.4	55.7	0.064	0.120	21	18
7/10/97 14:55:48 UTC	-70.7	-22.9	33	135.0	74.5	0.052	0.100	21	19
7/14/97 16:09:35 UTC	146.4	43.3	33	309.1	69.3	0.056	0.106	21	18
8/28/97 11:10:07 UTC	-33.9	57.1	10	40.0	57.2	0.064	0.118	20	20
7/15/97 11:15:24 UTC	122.4	24.8	101	307.2	96.1	0.041	0.077	21	0
10/14/97 09:53:18 UTC	-176.8	-22.0	167	233.2	80.4	0.048	0.093	6	6
8/29/97 06:53:59 UTC	-175.7	-15.2	33	237.4	74.8	0.052	0.100	19	19
7/19/97 12:22:57 UTC	-71.4	-29.0	26	139.4	79.0	0.049	0.095	21	21
7/19/97 14:24:23 UTC	-98.2	15.8	33	133.7	27.4	0.088	0.141	21	21

minus the station statics. After four iterations there is little improvement in variance

reduction.

We derived the S_{slow}-wave tomographic model from residuals relative to both a one dimensional velocity model for tectonic North America [*Grand and Helmberger*, 1984] and from the final S_{fast} model (Fig. 2d). In both cases, the same general patterns of anisotropy emerge, and the variance reductions are similar. The resulting anisotropic model predicts splitting that is very similar to independent SKS splitting measurements (Fig 1, Fig. S1). Tomographically predicted splitting reduces the variance of the SKS measurements by more than 50%. A linear regression to the data presented in figure S1 results in a slope of 0.95 ± 0.1, y-intercept of 0.42 ± 0.07, and linear correlation coefficient of 0.7. The intercept is non-zero because our study has solved for relative differences in velocity and we have assumed the smallest anisotropy in our tomographic model is zero.

Event and station statics (Table S1) also contribute to differential travel times and Δt^*. The event static is accounted for by first demeaning the measurements for a given event and then including a solution for the event static in the inversion. We find that the event statics resulting from the solution in the inversion are negligible, much less than 1% of the total variance for all models.

For the case of seismic velocity, station statics are obtained initially by correcting for elevation, before inversion, assuming a constant P and S-wave velocity and then, after inversion, examining the difference between the mean observed station delay relative to the mean predicted station delay. After the elevation corrections have been applied and four iterations of the inversions have been performed, removing the mean delay at each station removes an additional 20% of the original variance in

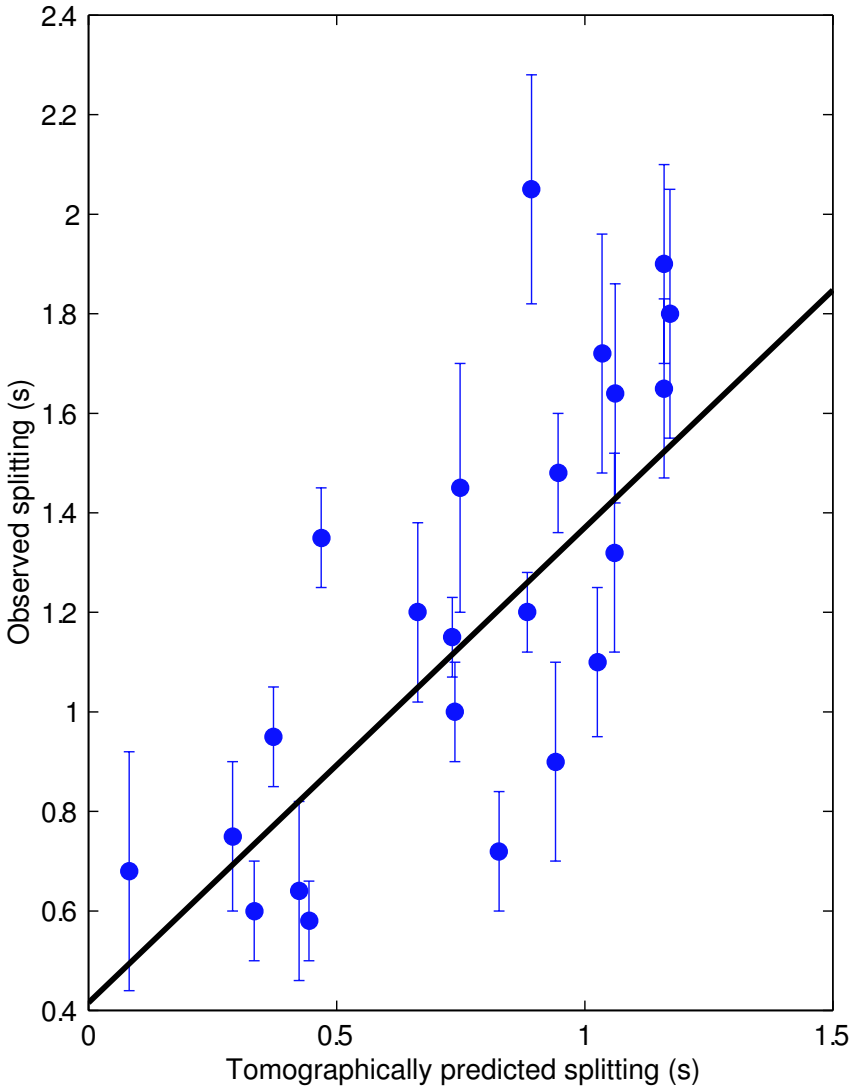

Figure S1. Tomographically predicted shear-wave splitting versus observed SKS splitting. The error bars are standard errors for the SKS splitting measurements. The black line results from a linear regression of the data and has a slope of 0.95 ± 0.1, y-intercept of 0.42 ± 0.07, and linear correlation coefficient of 0.7.

arrival times. These static corrections are consistent with variations in crustal velocity, slow in the Sierra and faster to the east and west [*Fliedner et al.*, 2000]. Stations statics for Δt^* account for less than 10% of the measured variance.

The total variance reductions from our tomographic inversions are 60% (∂v_p^{-1}), 64% (∂v_{sf}^{-1}), 61%, (∂v_{ss}^{-1}), 30%, (∂Q_{sf}^{-1}), and 21% (∂Q_{ss}^{-1}). Much of the variance that

has not been accounted for is likely due to higher spatial frequency variations in velocity and attenuation as well as variability occurring outside of the model domain. The substantially lower variance reductions for differential attenuation are due to the additional sources of uncertainty in Δt^*. Uncertainty in the measurements was determined by adding noise to the source time series and observing its effect on the measurement. The signal to noise ratio of the real times series was then correlated to the signal to noise ratio of the synthetic time series to determine the uncertainty. Variance due to this uncertainty in the measurements approach 4% (∂v_p^{-1}), 18% (∂v_{sf}^{-1}), 15% (∂v_{ss}^{-1}), 57% (∂Q_{sf}^{-1}), and 59% (∂Q_{ss}^{-1}), indicating that we have not overfit our observations but have recovered most of the variation from lateral variations in structure.

Calculation of anharmonic wave speeds requires absolute attenuation. Since we are interested in differences in wave speed, the exact offset of attenuation is not critical and so we safely add the minimum attenuation in our tomographic model to the attenuation values that are used to derive the anharmonic wave speeds. The correction for anelasticity involves the removal of the effects of dispersion from the seismic velocities. The correction is

$$V_0 = V\left[1 - \frac{1}{2}\cos\left(\frac{\pi\alpha}{2}\right)Q^{-1}\right]^{-1} \tag{S2}$$

where α reflects the frequency dependence of attenuation, assumed to be 0.25, and Q^{-1} is the seismic attenuation [*Minster and Anderson*, 1981]. P-wave attenuation is

assumed to be 4/9 S-wave attenuation, e.g. all energy is lost in shear. Since $Q \propto w^{0.25}$ and most of the energy in the P-wave is closer to 1 second whereas it is closer to 20 seconds for the S wave, P-wave attenuation is additionally reduced by a factor of 2.1 ($(20/1)^{0.25}$).

The areal extent of various compositions depicted in figure 3B was found using a number of seismic factors. The garnet peridotite was simply found by locating all fast anharmonic P-wave speeds and low anharmonic P-wave to S-wave speed ratios. Garnet pyroxenite was almost as simple, slow anharmonic P-wave speeds and high anharmonic P-wave to S-wave speed ratios, but also includes the constraint of low attenuation. Spinel peridotite proved to be the most difficult to locate where in addition to subsetting on intermediate anharmonic P-wave speeds and P-wave to S-wave speed ratios, we used the constraint of low anisotropy.

A3.2 MODEL RESOLUTION AND FIDELITY

We conducted spike tests to verify the anomalies observed in our tomographic models. For the spike test, a 50 km cube was centered at 36.4°N, 118.5°W, and 100 km depth and given anomalous seismic parameters of -0.01 ($d(1/v_p)$), -0.02 ($d(1/v_{sf})$), 0.02 ($d(1/v_{ss})$), and -0.04 ($d(1/Q_{sf})$). The input anomalies result in derived anomalies of 1.80 ($v_{p,o}/v_{sf,o}$) relative to a background of 1.73 and 0.10 for fractional anisotropy (Fig. S3). The recovered amplitudes of these anomalies are -0.006 ($d(1/v_p)$), -0.014 ($d(1/v_{sf})$), 0.004 ($d(1/v_{ss})$), -0.04 ($d(1/Q_{sf})$) 1.78 ($v_{p,o}/v_{sf,o}$) and 0.05 (fractional anisotropy). The variance reductions for the primary models are 85% ($d(1/v_p)$), 92% ($d(1/v_{sf})$), 74% ($d(1/v_{ss})$), and 91% ($d(1/Q_{sf})$). The variance reductions, having values

less than 100%, are due to imperfect ray coverage and the inability of the inversion to recover the strong seismic gradients near the spike edge. The discrepancy between the large variance reductions of these synthetic models relative to the real models is due to measurement uncertainty and noise.

Figure S2 contains the same vertical slice as Figure 2 of the main text and goes through the center of the synthetic anomaly. The seismic anomalies are well recovered with the exception of the shear velocity oriented in the slow direction (Fig. S3). This is due to relatively poor ray coverage for the slow oriented shear wave at this latitude. As a consequence, the magnitude of the derived parameter of seismic anisotropy at this latitude is not well resolved.

The spike tests have similar features for each parameter. The spike should appear as a square but has been elongated in the vertical direction. There is also a small amount of smearing along the NW/SE and NE/SW ray path directions. These artifacts do not reproduce the geometry of the features seen in the tomographic slices presented in Figure 2 which cover the entire depth range and trend more E-W. In addition, the dipping high velocity feature does not have stations projected along its axis to the surface, a verification that it is not an effect of smearing of an anomaly along a ray path.

The reason there is varying ray coverage for each S-wave observable is because of the weighting. Each data point and corresponding ray are weighted according to the standard error of the measurement which is a function of the signal to noise ratio. S-waves are polarized differently for each event, so when rotated into S_{fast} and S_{slow} coordinates, one component will often have a small amplitude. It happens that the

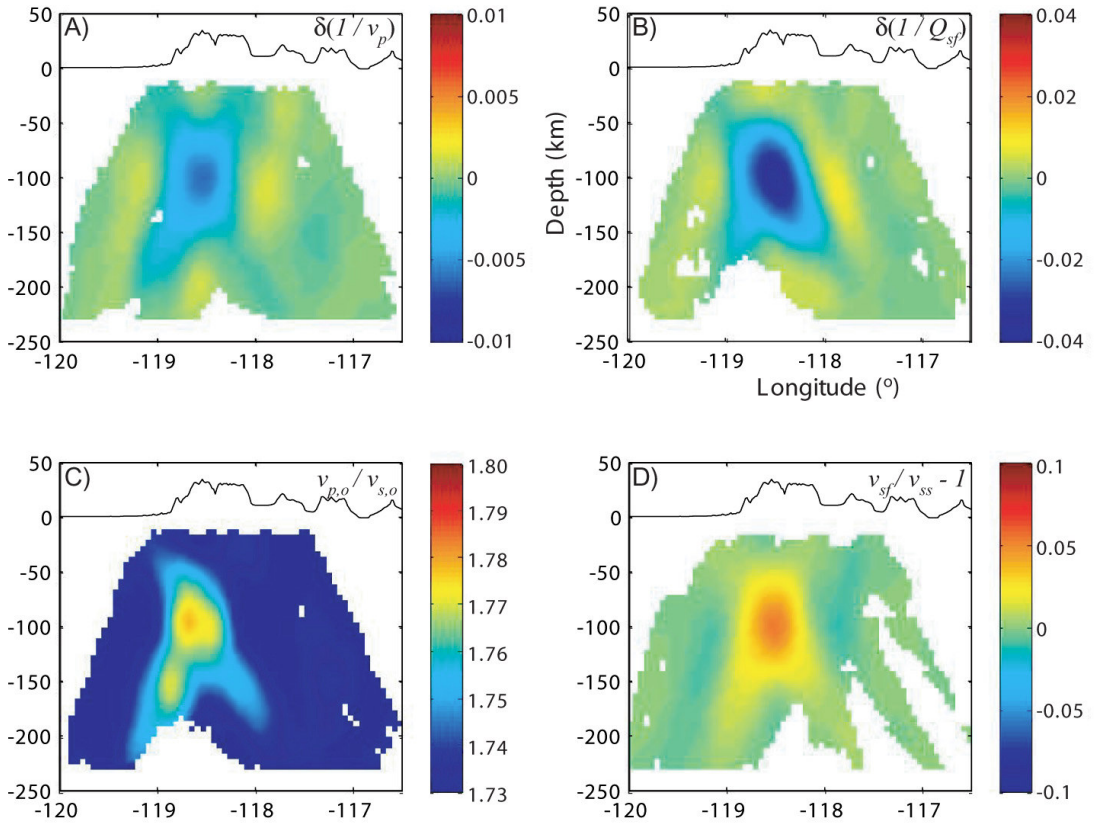

Figure S2. Vertical slices of spike tests at same latitude as figure 2 of main article. 50 km square 'spike' is placed at depth 75 to 125 km, centered about 36.4°N and 118.5°W. A small amount of smearing is present along the ray path directions which are generally oriented NW to SE with a fewer number from the SW and NE. This is in contrast to the EW oriented seismic anomaly presented in figure 2.

component of the S-wave in the slow direction usually has a greater amount of noise and hence less weight for paths that traverse this region.

A3.3 Effects on wavespeed and calculation of mineral physics constants

Decreases in velocity can be caused by increases in temperature [*Karato*, 1993], the presence of partial melt [*Hammond and Humphreys*, 2000b], the presence of partially saturated nominally anhydrous minerals [*Karato and Jung*, 1998], or

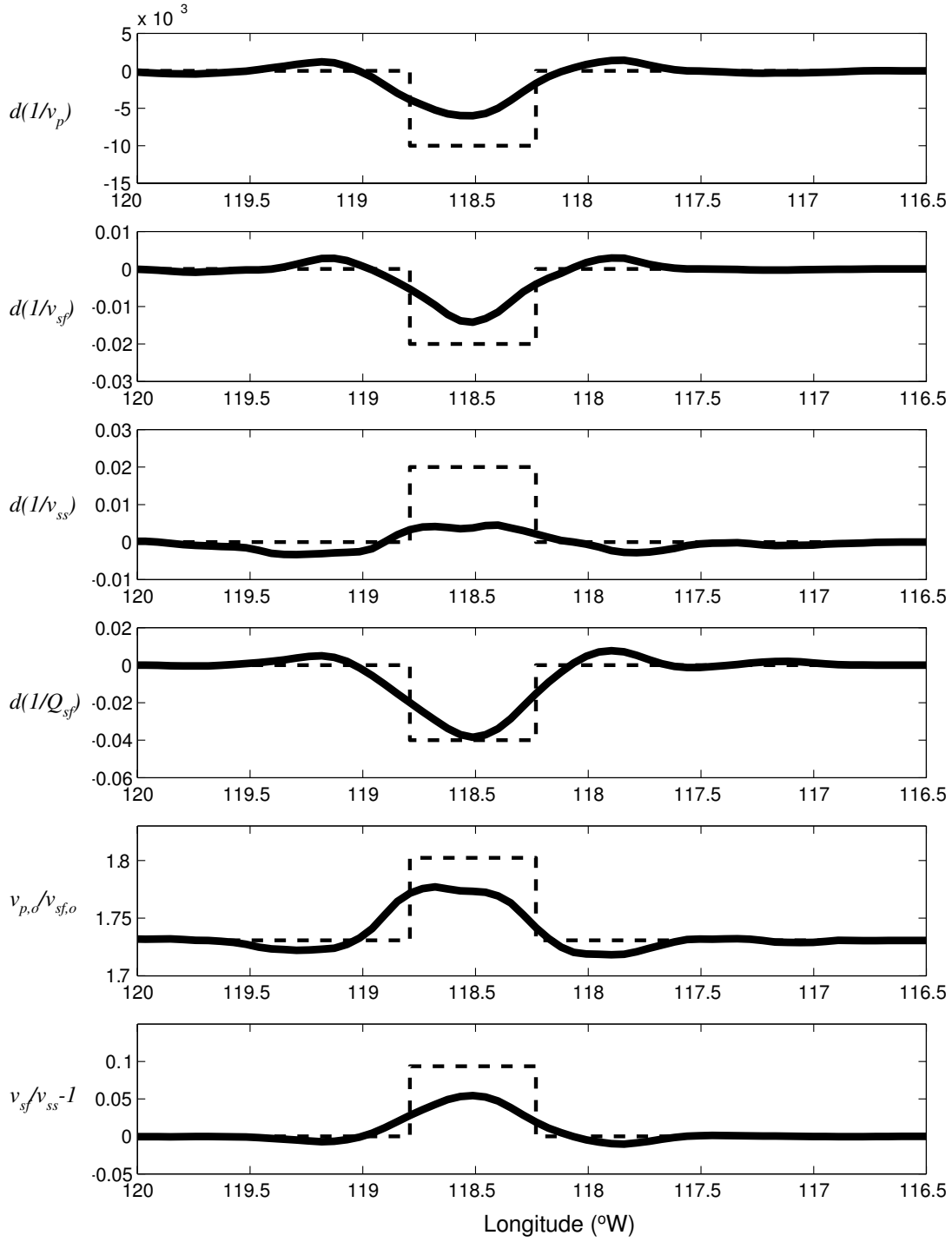

Figure S3. Comparison of spike test results (solid lines) with original spike (dashed lines). From top to bottom is shown $d(1/v_p)$, $d(1/v_{sf})$, $d(1/v_{ss})$, $d(1/Q_{sf})$, $v_{p,o}/v_{sf,o}$ and v_{sf}/v_{ss} -1.

petrological and geochemical effects such as differing amounts of garnet relative to

olivine or magnesium relative to iron [*Christensen*, 1996]. Of course, these possibilities also affect v_P/v_S, attenuation, and anisotropy (Table 1). Partial melt in itself may not affect attenuation [*Hammond and Humphreys*, 2000a] but will significantly decrease the P and S wavespeeds and lead to greater v_P/v_S ratios. Attenuation will probably increase if melt is present but only because of the increased temperatures needed to produce melt. It is possible that low attenuation could accompany partial melt if there are mineral phases present that melt at lower temperatures [*Boyd and Sheehan*, in Press]. The effect of saturating nominally anhydrous minerals with water would probably increase attenuation [*Karato and Jung*, 1998], resulting in higher v_P/v_S ratios. Compositional effects will have a small effect on attenuation but a much greater effect on v_P/v_S ratios. For example, garnet is generally faster than olivine and has a greater v_P/v_S ratio. Increasing the Mg# [Mg/(Mg+Fe)] of most minerals increases the seismic velocities but decreases the v_P/v_S ratio [*Hacker et al.*, 2003]. Composition also significantly effects seismic anisotropy. Olivine is a highly anisotropic mineral [*Kumazawa and Anderson*, 1969] while garnet is not [*Babuska et al.*, 1978]. Pyroxenes have significant anisotropy [*Aleksandrov et al.*, 1963] but are not expected to develop preferred mineral orientation and hence are not expected to contribute to anisotropy in the rock aggregate [*Gueguen and Nicolas*, 1980]. To interpret our results, we must account for this information in light of constraints provided by petrology of the xenoliths.

The mineral end-member modal compositions for the three average rock types appearing in figure 3A are as follows. They have the same Mg# as reported in the main text but relative amounts of pyroxene and garnet were adjusted to match the

tomographically determined seismic velocities. The garnet pyroxenite consists of 15.5% almandine, 4.2% grossular, 10.3% pyrope, 50.7% diopside, and 19.3% hedenbergite. The garnet peridotite consists of 0.7% almandine, 0.7% grossular, 3.6% pyrope, 65.2% forsterite, 9.8% fayalite, 4.6% diopside, 13.3% enstatite, 1.7% ferrosilite, and 0.4% hedenbergite. Finally, the spinel peridotite, but substituting garnet for spinel since the calculations were made at 3GPa, consists of 1.5% almandine, 2.5% pyrope, 67.7 % forsterite, 12.3% fayalite, 13.8% enstatite, and 2.2% ferrosilite.

As stated in the article, the calculation of mineral physics constants is found using the methods of Bina and Hellfrich [1992] and Holland and Powell [1998] with the mineral constants compiled by Hacker et al. [2003]. The method is also summarized by Hacker et al. [2003] though the equations for the temperature dependence of thermal expansion and the isothermal bulk modulus at elevated temperature and pressure were misprinted. These equations are correctly printed in a later article by Hacker and Abers [2004] in which they also include an Excel macro to perform this calculation. Our method differs slightly and is explained in the subsequent paragraphs.

The anharmonic P-wave and S-wave velocities are given by

$$v_p = \sqrt{\frac{K_S + \frac{4}{3}\mu}{\rho}} \qquad \text{(S3)}$$

$$v_s = \sqrt{\frac{\mu}{\rho}}$$

where K_S is the adiabatic bulk modulus, μ is the shear modulus and ρ is the density. Changes to the density and moduli due to changes in temperature, dT, are related to the thermal expansivity, α, through

$$K_T(T) = K_{T0}e^{-\delta_T \int_{298}^{T} \alpha dT}$$
$$\mu(T) = \mu_0 e^{-\theta \int_{298}^{T} \alpha dT} \quad \text{(S4)}$$
$$\rho(T) = \rho_0 e^{-\int_{298}^{T} \alpha dT}$$

where δ_T is the isothermal second Gruneisen parameter, θ is the logarithmic change in shear modulus with respect to pressure, and K_T is the isothermal bulk modulus. The isothermal bulk modulus is related to the adiabatic bulk modulus by

$$K_S = K_T(1 + T\alpha\gamma_{th}). \quad \text{(S5)}$$

Here, γ_{th} is the first Gruneisen parameter. Before this equation can be implemented, the thermal expansivity and isothermal bulk modulus must be corrected for the change in pressure and temperature. The integral over αdT can be solved easily given that α is approximately related to temperature by a simple polynomial

$$\alpha(T) = \alpha^o\left(1 - \frac{10}{\sqrt{T}}\right) \quad \text{(S6)}$$

where α^o is the high temperature limit of α.. Its solution is

$$\int_{298}^{T} \alpha(T)dT = \alpha^o(T-298) - 20\alpha^o\left(\sqrt{T} - \sqrt{298}\right). \tag{S7}$$

After the temperature has been accounted for, changes to the expansivity, density and moduli due to changes in pressure must be found. The thermal expansivity as a function of pressure is

$$\alpha(T,P) = \alpha(T)(1+2f)^{\frac{-3\delta_T}{2}} \tag{S8}$$

where f is the finite strain. The density at pressure is

$$\rho(f) = \rho(T)(1+2f)^{3/2}. \tag{S9}$$

The isothermal bulk modulus and shear modulus at pressure and temperature to fourth order in strain is

$$K_T(f) = K_T(T)(1+2f)^{5/2}\left\{\begin{array}{l} 1 - f\left(5 - 3K_T^{'}\right) + \\ \frac{f^2}{2}\left[9K_T(T)K_T^{''} + \left(3K_T^{'} - 7\right)\left(3K_T^{'} - 5\right)\right] \end{array}\right\}$$

$$\mu(f) = \mu(T)(1+2f)^{5/2}\left\{\begin{array}{l} 1 - f\left(5 - 3\mu' K_T(T)/\mu(T)\right) + \\ \frac{f^2}{2}\left[9\mu'' K_T^2(T)/\mu(T) + 9\mu' K_T(T)/\mu(T)\left(K_T^{'} - 4\right) + 35\right] \end{array}\right\}$$

(S10)

The primes in the above expression denote pressure derivatives. Bina and Helffrich suggest μ'' and K_T'' are of order $1/\mu$ and $1/K_T$ and can be directly substituted into the above expressions, though Hacker and Abers prefer an alternate approximation which is to ignore the terms on the right preceded by f^2.

The strain is found by solving the equation

$$P = 3K_T(T)f(1+2f)^{5/2}\left\{1-2\xi f+\frac{f^2}{6}\left[9K_T(T)K_T''+4\xi\left(4-3K_T'\right)+5\left(3K_T'-5\right)\right]\right\} \quad \text{(S11)}$$

for f. Whereas Hacker and Abers solve this equation iteratively and ignore the term on the right containing $f^2/6$, we turn this equation into a polynomial and use the Matlab roots function to find a solution for f. We then choose the root that is real and closest to the first order solution

$$f = \sqrt{\frac{\left(P/K_T(T)\right)^2}{9}}. \quad \text{(S12)}$$

This method can be obtained as a matlab function at ftp://mantle.colorado.edu/pub/oliverb/MinVel.m. with mineral database at, ftp://mantle.colorado.edu/pub/oliverb/MinPar.csv.

APPENDIX 4. *t** UNCERTAINTY FROM THE INTERFERENCE OF AN ADDITIONAL WAVELET

A4.1 ABSTRACT

Interfering wavelets are generated by reflections, conversions, multipathing, and anisotropy. This interference produces spectral distortion which can cause significant uncertainty in measurements of attenuation obtained with the use of *t**. I show how *t** is affected by the interference of a single wavelet and present *t** data which illustrates the decrease in uncertainty by accounting for seismic anisotropy.

A4.2 INTRODUCTION

Measurement of the attenuation of seismic waves combined with seismic velocities is a powerful tool to successfully interpret the thermal and compositional variability of the material through which the seismic waves have passed [*Boyd and Sheehan*, 2002]. Characterizing seismic attenuation in the earth is required to properly determine source magnitudes, assess earthquake hazards, and appreciate the conditions under which global dynamics takes place [*Romanowicz*, 1998].

Seismic attenuation can be measured by several techniques. In the time domain, a transfer function can be computed to attenuate a reference trace, thereby producing the observed trace [*Bhattacharyya*, 1998]. In the frequency domain, attenuation can be measured from the decay of spectral amplitudes of an observed signal relative to a

reference signal [*Sheehan and Solomon*, 1992]. These methods produce integrated measures of attenuation, Q^{-1}, referred to as t^*,

$$t^* = \int_{Path} \frac{dt}{Q}, \tag{1}$$

and so must be normalized by the time spent along the path to derive the path average attenuation. Tomographic methods can be employed to derive attenuation along the path [*Lee and Grand*, 1996; *Roth et al.*, 1999]. In what follows, I aim to inform the reader as to one of the inherent uncertainties in measuring t^*, uncertainty arising from the interference of additional wavelets. As an example, I will use teleseismic data acquired in 1997 during the Sierran Paradox Experiment to show that accounting for seismic anisotropy reduces the uncertainty of the t^* measurement.

Interference of multiple copies of a common wavelet occurs as a matter of fact within the field of seismology [*Aki and Richards*, 2002]. As a seismologist, when trying to decipher a set of waveforms, I find the task akin to working my way out of a house of dirty and distorted mirrors. But interference isn't necessarily a problem. It only becomes a problem when looking at relative differences between a set of waveforms and the waveforms do not have the same set and position of interfering wavelets. Some forms of interference include overlapping seismic phases, e.g. S and ScS at the proper source/receiver distance, S to P conversions, topographic scattering, or reflections off of the bottom of a sedimentary basin. A more significant interference phenomenon is that generated by seismic anisotropy. Potentially, two

wavelets of equal magnitude interfere within a fraction of the dominant period of the original waveform.

A4.3 METHOD

When one is measuring t^*, interference of additional wavelets can bias the t^* measurement. Ultimately, one would like to be able to identify the interfering waveforms and remove them. Measurement of t^* follows from an evaluation of the spectral amplitude of a station time series, $A_S(w)$, relative to the spectral amplitude of a reference time series, $A_R(w)$. These spectra in their simplest form are given by

$$A_S(w) = S(w)I(w)G_S e^{-wt_S^*/2} \tag{2}$$

and

$$A_R(w) = S(w)G_R e^{-wt_R^*/2} . \tag{3}$$

Typically, the reference would have the same source spectrum, $S(w)$, as the station. The stations instrument response, $I(w)$, is deconvolved from the station time series. G is the geometrical spreading which we assume to be frequency independent. We find relative t^* by finding the slope of the relationship between the natural log of the ratio of spectral amplitudes to angular frequency, w,

$$\ln\left(\frac{A_S(w)G_R}{A_R(w)G_S}\right)=\frac{-wt^*_{S-R}}{2}\ . \tag{4}$$

Taking the derivative of both sides with respect to frequency and solving for $t_{S\text{-}R}$* gives

$$t^*_{S-R}=-2\frac{d\ln\left(\frac{A_S(w)G_R}{A_R(w)G_S}\right)}{dw}\qquad . \tag{5}$$

The spectral amplitude of the station, $A_S(w)$, may contain the effect of interfering wavelets and assume a functional form much more complicated than that given by (2). If we suppose that these interfering wavelets have the same shape as the wavelet of interest but are lagged in time with a different amplitude, what is the new spectral amplitude of the station trace? The complex amplitude spectrum of a station trace is given by the Fourier Integral Theorem:

$$F_S(w)=\int f(t)e^{-iwt}dt\ . \tag{6}$$

Let us assume for the moment that $f(t)$ is in fact $f_1(t)+f_2(t)$. We will find that

$$F_S(w)=F_1(w)+F_2(w)\ . \tag{7}$$

If $f_2(t)$ happens to be $Bf_1(t+\tau)$ where B is a scalar and τ is the delay of f_2 relative to f_1, then the shifting theorem of the Fourier transform will lead us to

$$F_S(w) = F_1(w) + BF_1(w)e^{iw\tau} = F_1(w)(1 + Be^{iw\tau}) . \tag{8}$$

The square root of the power spectrum of $F_s(w)$, e.g. the type of spectral amplitudes appearing in (2) and (3) is

$$A_S(w) = A_1(w)\sqrt{1 + B^2 + 2B\cos(w\tau)} . \tag{9}$$

We see that the spectrum at a station is composed of the spectrum of interest multiplied by a term resulting from the interfering wavelet where the interfering wavelet has the same shape but amplitude B and delay τ relative to the primary wavelet. The resulting equation for t* becomes

$$t^* = -2\left[\frac{d\ln\left(\frac{A_1(w)}{A_R(w)}\right)}{dw} + \frac{d\ln\left(\frac{G_R}{G_S}\right)}{dw} + \frac{d\ln\left(\sqrt{1+B^2+2B\cos(w\tau)}\right)}{dw}\right]$$

$$= -2\frac{d\ln\left(\frac{A_1(w)}{A_R(w)}\right)}{dw} + \frac{2B\tau\sin(w\tau)}{1+B^2+2B\cos(w\tau)} \quad . \tag{10}$$

The equation for t^* contains the measurement of interest plus a term resulting from the interference of an additional wavelet not present in the reference. Figure 1 illustrates the form of the second term in (10) averaged over the frequency range 0.03 to 0.1 Hz for an interfering wavelet having a relative amplitude, B, of -0.6,.-0.3, 0.3, and 0.6 relative to the original for a range of offset , τ, from 0 to 30 seconds.

The second term in (10) does not account for the fact that measurements are made on a finite time series that is typically tapered. To properly access figure 1, one could taper the graph of apparent t* versus offset such that when the offset is half of the window length, apparent t* approaches zero. Another factor to keep in mind is that these curves are averaged over the frequency range 0.03 to 0.1 Hz and that a greater frequency range over which the measurement is averaged will produce less apparent t*. However, since attenuation and consequently t^* is frequency dependent and higher frequencies are more susceptible to scattering, averaging over a greater frequency range may not produce more meaningful results.

As I said before, we would ultimately like to be able to identify and remove or otherwise account for interfering wavelets. Principle component analysis may be a viable means of identifying and possibly removing interfering wavelets [*Bostock and Rondenay*, 1999]. An alternative method would be to predict the interfering wavelets based on synthetic seismograms produced from a local high resolution velocity model [*Komatitsch et al.*, 2002].

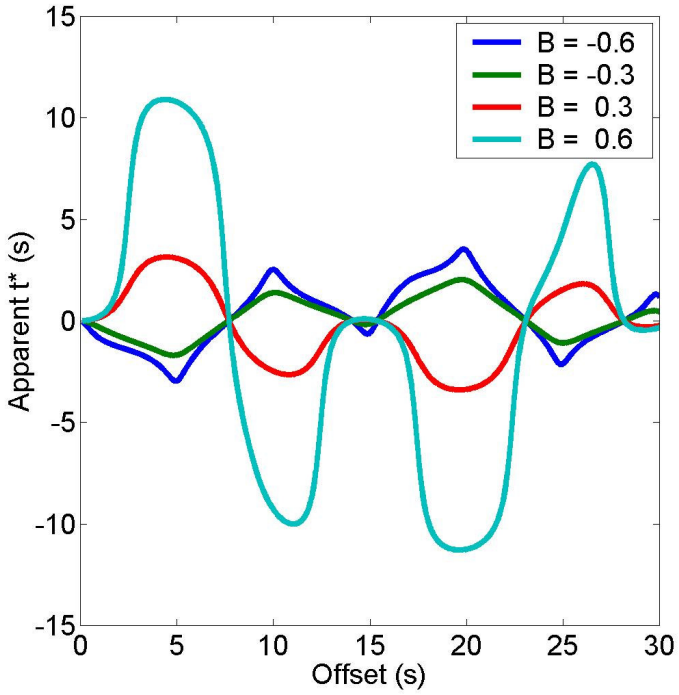

Figure 1. Apparent t* versus offset, τ, for various values of B, -0.6 (blue), -0.3 (green), 0.3 (red), and 0.6 (cyan), averaged over the frequency range 0.03 to 0.1 Hz.

A4.4 EXAMPLE

To see that interference is a problem for real seismic data, consider the measurement of t^* for teleseismic waves arriving to stations in the Sierra Nevada, a region having strong seismic anisotropy (Figure 2). A first order approach to account for seismic anisotropy would be simply to rotate the seismograms into the mean fast and slow directions (assuming a single layer of splitting). Ideally, anisotropy would be measured on the phase for which t^* is being measured and each stations anisotropy would be accounted for individually. t^* for tomographic problems is typically measured on the S phase while anisotropy is measured on the SKS phase. These

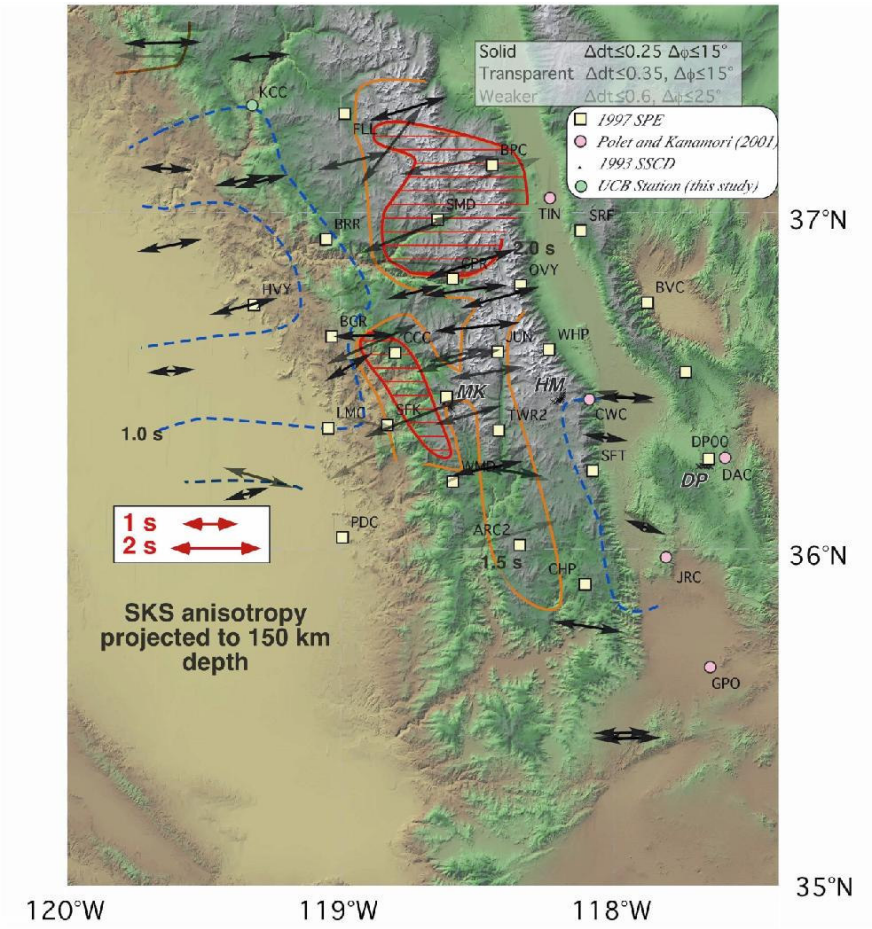

Figure 2. After Jones and Phinney [1999]. SKS splitting measurements in the southern Sierra Nevada. Splits are predominantly parallel to North American plate motion in this region. The fast direction of seismic anisotropy averages N80E.

phases have slightly different ray paths and so anisotropy determined for SKS may not apply to S.

I have made measurements of t^* for 192 traces from 16 events using up to 24 stations. The events have a wide distribution in back azimuths from 100° to 310°. Typical t^* measurements are made on the transverse components. I identify the S-wave and rotate the horizontal seismograms into either the radial and transverse directions or the mean fast and slow direction (N80E/S10E). Since rotating the seismograms into the radial and transverse directions should sample a range of

interfering wavelets due to anisotropy, the standard deviation of t^* for measurements made in the transverse and radial directions should be greater than t^* measurements made in the mean fast and slow directions. And indeed it is. The standard deviation of t^* for measurements made in the transverse and radial directions is 1.04 s and 1.04 s respectively. The standard deviation of t^* for measurements made in the mean fast and slow direction is 0.97 s and 0.90 s respectively.

A4.5 CONCLUSIONS

But are these differences statistically significant? It could be argued that the statistical quantity called the standard deviation of the mean, the standard deviation divided by the square root of the number of measurements, normally applied to reflect the uncertainty in the mean, is one such measure. It would be the uncertainty if all of the variability in measured t^* were due to random error. In my case it is considered an upper limit since some and conceivably most of the standard deviation represents true variability. For 192 t^* measurements, the standard deviation of the mean for rotating into the transverse, radial, mean fast and slow directions is 0.07 s. Therefore, the difference in standard deviations reported above is statistically significant. Accounting for seismic anisotropy reduces t^* uncertainty.

This is not proof that the uncertainty due to interference follows the form given in (10). Presumably, there are many interfering wavelets of many sizes and offsets and wavelets that have distorted spectral content relative to the primary wavelet. My aim is only to show that interference is a problem that must be taken into account.

Many methods can be used to account for interference and the best method will likely be specific to the problem. I do believe that the measurement of attenuation in the earth is required and that earth scientists should not be daunted by the possible uncertainties of t^* measurement.